ABSTRACT

Title of Document:	MINIMUM ENERGY DESIGN OF SEAWATER HEAT EXCHANGERS
	Patrick Luckow, Master of Science, 2009
Directed By:	Professor, Avram Bar-Cohen, Mechanical Engineering
	Associate Professor, Peter Rodgers, Mechanical Engineering

Industrial cooling with seawater, particularly natural gas liquefaction in arid environments, places large strains on existing heat exchanger designs. High temperature, high salinity water damages metals and leads to devices with a short useful life. Cost effective, corrosion resistant heat exchangers are required to fully utilize available saline water resources. Thermally conductive polymer composites, using carbon fiber fillers to enhance conductivity, are a promising material.

This Thesis provides a characterization, analysis, and optimization of heat exchangers built of anisotropic thermally conductive polymers. The energy content of such polymers is compared to several other materials, and the required content of carbon-fiber fillers is studied for optimum conductivity enhancement. A methodology for the optimization of low thermal conductivity fins, and subsequently heat exchangers, is presented. Finally,

the thermal performance of a prototype thermally enhanced polymer heat exchanger is experimentally verified, and compared to numerical and analytical results.

MINIMUM ENERGY DESIGN OF SEAWATER HEAT EXCHANGERS

By

Patrick Wass Luckow

Thesis submitted to the Faculty of the Graduate School of the
University of Maryland, College Park, in partial fulfillment
of the requirements for the degree of
Master of Science
2009

Advisory Committee:
Professor Avram Bar-Cohen, Co-chair
Professor Peter Rodgers, Co-chair
Professor Reinhard Radermacher
Professor Bao Yang

Acknowledgements

I am very appreciative of the insights I have received from Dr. Avram Bar-Cohen throughout my research. He has continually pushed me to study what I am most interested in, and as I result I have pursued the thermal design of heat transfer devices on the basis of energy efficiency and sustainability. I am also very grateful for the time I have spent working with Dr. Peter Rodgers, whose guidance in analyzing experimental results of prototype heat exchangers has been very helpful in effectively presenting my conclusions.

This work continues along the theme of design of sustainability previously studied by Dr. Madhu Iyengar and Dr. Raj Bahadur, whose use of the concepts of least material optimization and lifecycle energy costs of heatsinks provided a strong foundation for this analysis.

I would also like to thank my MS committee members Dr. Reinhard Radermacher and Dr. Bao Yang. I have learned much from both in my class work which has been applied throughout this study, and their thoughts and comments in improving this work are much appreciated.

I am also very grateful of support from my colleague Juan Cevallos. Much of the work presented here would not have been possible without his support of the injection molding concerns, as well as his fabrication of the prototype heat exchanger.

This research was supported as a part of The Energy Education and Research Collaboration (EERC) between the University of Maryland and The Petroleum Institute. The Abu Dhabi National Oil Company (ADNOC) and its international partners deserve thanks for their generous financial support.

Table of Contents

List of Figures

List of Tables

Nomenclature

A_b	Base area [m^2]
A_f	Fin area [m^2]
A_t	Total area [m^2]
c_p	Specific heat capacity [J/kg K]
C	Heat capacity rate [W/K]
COP	Coefficient of performance [W/W]
COP_T	Total coefficient of performance [MJ/MJ]
D_h	Hydraulic diameter [m]
E_M	Manufacturing energy per unit mass [MJ/kg]
F	Friction coefficient [-]
h	Heat transfer coefficient [W/m^2 K]
H	Channel height [m]
K	Thermal conductivity [W/m K]
k_1	Polymer resin thermal conductivity [W/m K]
k_2	Filler thermal conductivity [W/m K]
k_E	Einstein coefficient [-]
K_L	Loss coefficient [-]
L	Length of channel [m]
m	Heat exchanger mass [kg]
N	Number of fins [-]
NTU	Number of transfer units [-]
Nu	Nusselt number [-]
P	Pumping power [W]
Pr	Prandtl number [-]
q	Heat transfer rate [W]
Re	Reynolds number [-]
S	Fin spacing [m]
t_f	Thickness [m]
t_b	Dividing wall thickness [m]
T	Temperature [^oC]
U	Overall heat transfer coefficient [W/m^2 K]
UA	Heat transfer capacity for a given matrix [W/m^2 K]
u_m	Mean Fluid Velocity [m/s]
$\dot{\forall}$	Volumetric Flowrate [m^3/s]
W	Base Width [m]
W_M	Manufacturing Energy [MJ]

Greek Letters

Δp	Pressure Drop [Pa]
ε	Effectiveness [-]
η_f	Fin efficiency [-]
η_o	Overall surface efficiency [-]
μ	Viscosity of fluid [N s/m^2]
ϕ_2	Filler volume fraction [-]

ϕ_m	Maximum packing fraction [-]
ρ	Density of fluid [kg/m^3]

Subscripts

1	Hot fluid side
2	Cold fluid side
c	Cold
h	Hot
I	Inlet
O	Outlet

Chapter 1: Introduction

In a wide variety of industrial processes, heat exchangers are a fundamental component. Many of these involve the heating and cooling of highly corrosive fluids. A seawater cooled heat exchanger for the liquefaction of natural gas is studied here. The high-temperature, high-salinity water used in such applications frequently leads to heat exchanger failure due to corrosion, as a well as scale build-up. Increased use of corrosion resistant materials could reduce plant downtime and increase revenue.

A global energy demand increase of 65% over 2004 levels is forecasted for 2030 [1]. Rather than simply generating more power to meet this demand, end-use energy efficiency improvements, dematerialization, and selection of lower energy and recycled materials can be used to reduce the rate of growth in energy consumption. For a typical heat exchanger, efficiency gains have typically been achieved primarily through improved manufacturing processes and thermofluid designs that reduce pumping power. The availability of stronger and more thermally-conductive, yet energy efficient, polymers [2] could provide new opportunities in heat exchanger design. High thermal conductivity polymer heat exchangers could offer significant benefits over those currently used in seawater applications for the power industry, as well as coastal petroleum refineries and gas liquefaction plants. Such heat exchangers may provide greater corrosion resistance, lower raw material cost, lower manufacturing cost, reduced disposal costs, and increased geometric flexibility. For heat exchangers in corrosive environments, significant energy gains can be made by increasing the service life through material substitution.

Additionally, the inherently low energy of fabrication and formation for polymer materials may lead to considerable energy savings over the lifetime of the heat exchanger. For heat exchangers in corrosive environments, where service lives are typically low - on the order of a year or less – the bulk of the energy consumed by the heat exchanger is in manufacturing, rather than pumping power. By designing a heat exchanger to generate the most heat transfer for a given amount of mass, the mass – and thus manufacturing energy – is minimized.

Polymers may also offer flexibility in geometric design due to manufacturing techniques unavailable with typical corrosion resistant metals, such as injection molding.

1.1 Application of Polymer Heat Exchangers to Natural Gas Liquefaction

The Abu Dhabi Gas company (ADGAS), a subsidiary of the Abu Dhabi National Oil Company (ADNOC), processes and distributes natural gas in the United Arab Emirates. Seawater is a crucial coolant in this process, and yet - due to its location on the coast of the Persian Gulf - this seawater can have a mean surface temperature as high as 32ºC and salinity up to 45 g/kg [3]. To date, these conditions have required heat exchangers built from expensive, corrosion resistant alloys.

This thesis explores the thermofluid characteristics of heat exchangers built of high thermal conductivity polymers, for conditions typically seen by ADGAS. Pure methane, the primary constituent of natural gas, is assumed for the gas, while seawater properties are used for the liquid. Typical heat exchanger parameters are given in Table 1 for a regenerator overhead condenser [4]. Other heat exchangers have liquid velocities ranging from 1.3-2.7 m/s and gas velocities from 0.40 to 11.20 m/s.

	Gas	**Liquid**
Velocity (m/s)	11.2	1.7
Inlet Temp (°C)	103	35
Inlet Pressure (bar)	1.98	4.51
Pressure Drop (bar)	0.14	0.7
Heat Exchanged (MW)	30.8	
Volume (m^3)	6.5	
Volumetric Heat Transfer (MW/m^3)	4.7	

Table 1: Commercial NG Liquefaction Heat Exchanger Properties [4]

Such a heat exchanger transfers a large amount of heat, and is essential to the operations of the natural gas liquefaction train. However, the high fluid temperatures

encountered in the UAE LNG application can aggravate the corrosion and scaling problems, as discussed in section 1.3.

1.2 Seawater & Natural Gas Properties

Natural gas is a colorless, odorless gas that burns cleaner than most other fossil fuels. The US Government plans to reduce greenhouse gas emissions may encourage the use of natural gas for electricity generation. Beyond pipelines from Canada, and potentially Alaska, liquefaction of the natural gas facilitates transport over large distances. To meet demand, U.S. imports of liquefied natural gas are expected to grow rapidly, from 631 billion ft^3 in 2005 to 2.1 trillion ft^3 in 2015 [5]. As a typical natural gas "mix" contains 70-90% methane and may vary from well to well, pure methane is used as the working gas in this study [6].

Property	Methane (90ºC)	Seawater (25 ºC)
ρ (kg/m^3)	0.539	1022
μ (Ns/m^2)	1.31E-05	1.08E-03
c_p (J/kgK)	2411	3993
k (W/mK)	0.0335	0.596
Pr (-)	0.73	7.23

Note: Sea water salinity taken at 35 g/kg.

Table 2: Fluid Properties**.**

The properties of seawater are quite close to those of freshwater, despite high salinity levels, with a typical density increase of 2-3% , due to the salt content of the water. The methane properties in Table 2 show the pronounced differences of gas properties from those of liquids; in particular, the thermal conductivity and density are dramatically less than that of seawater. These differences will dominate the thermal performance seen in industrial applications discussed here.

Several factors, such as alkalinity, total dissolved CO_2, and calcium and silica concentrations can affect the thermodynamic properties of seawater, and represent the source of existing uncertainty. Variations in the composition of seawater can have a

maximum impact on density of 24 g/m^3 in the open ocean, and as high as 130 g/m^3 in the Baltic Sea Estuary [7] .

1.3 Corrosion and Scale Build Up in Heat Exchangers

ADGAS heat exchangers have been found to have very short service lives, from a few months to a year, depending on flow rates, temperatures, and water conditions [8]. The two limiting factors on heat exchanger service life are scale formation and corrosion. The main source of scale forming within heat exchangers has been found to be calcium carbonate, as well as some calcium sulphate. Scale forms due to the elevated temperatures observed within some heat exchangers, leading to oversaturation of these dissolved minerals in the injected sea water [9]. Figure 1 presents an example of scale formation on a heat exchanger tube bundle that was found during inspection.

Figure 1: Scale formation at the inlet of a tube bundle [10]

Scale formation within the heat exchangers leads to decreased fluid flowrate and increased thermal resistance. Scale formation at the surfaces of the heat exchangers can also give rise to under-deposit corrosion on the cooling water side of the heat exchanger tubes, another, potentially catastrophic failure mode.

ADGAS identified several primary corrosion types; pitting, erosion, crevice and hydriding. A brief description of these corrosion types is given below.

Pitting is a form of extremely localized corrosion that leads to the creation of small holes in the metal, caused by a concentrated lack of oxygen. Figure 2 shows a heat

exchanger tube, covered with scales on the inside. Underneath the scales, localized pitting and corrosion can be observed.

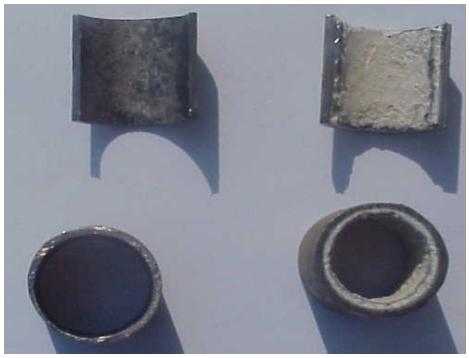

Figure 2: Seawater scaling on titanium tubes

Pitting corrosion is dangerous because when the holes pierce through the wall, fluid mixing can occur, which can be disastrous in processing applications. The speed of pitting corrosion and the resulting hole size tends to increase with time, after an initial incubation period [11]. When a metal corrodes, typically a corroded film remains on the surface, preventing further corrosion. At increased fluid velocities, this film is swept away and corrosion continues uninhibited. The critical velocity varies according to the fluid chemistry and also presence and nature of solids. For seawater, titanium tubes have been proven to handle velocities as high as 30 m/s, although 8 m/s is a more commonly use value for pure titanium [12]. These values are for seawater with no entrained particles, such as sand or biological matter. Typical seawater velocities seen in natural gas liquefaction trains rarely exceed 4 m/s.

1.4 Advantages of Polymers

Thermally enhanced polymers provide the potential benefit of resisting both scaling and corrosion, while still providing comparable performance to materials currently in use. Polypropylene's strong resistance to seawater corrosion led to its extensive use in the Ocean Thermal Energy Conversion (OTEC) heat exchangers [13]. Zaheed and Jachuck [14] reviewed the availability and application range of several commercial polymer heat exchangers. Unfilled polypropylene polymer, with a thermal conductivity of just

0.25W/mK, is a rather poor heat exchanger material. Alternatively, thermally-enhanced polymer composites, filled with pitch-based, carbon micro fibers that raise the thermal conductivity by one-to-two orders of magnitude, are believed to make seawater polymer heat exchangers a viable approach. It must be noted, however, that the thermal conductivity and structural properties of such polymers are dependent on the fiber orientation and geometry, leading to anisotropy in the heat exchanger walls. Thermally-enhanced polymer heat exchangers may provide, in addition to greater corrosion resistance, lower raw material cost, lower manufacturing cost, reduced disposal costs, and increased geometric flexibility.

Polymers also offer significant weight savings potentials as compared to metals. Several unfilled polymers have densities under 1 gm/cm^3, much less than copper, titanium, or even aluminum. Thermally enhanced polymers may have a higher density, approaching 2 gm/cm^3 for the highly concentrated filled polymers, due to the higher density of the fillers used to enhanced the conductivity. Still, this value is lower than the metals typically used in heat exchanger applications. These weight savings mean less energy is used in both manufacturing and transportation of these heat exchangers.

1.5 Water Use in U.S. Power Plants

While high temperature, high salinity seawater is a crucial coolant in natural gas liquefaction in the Persian Gulf, saline water cooling has applications worldwide. Water is used as the primary coolant for steam condensers, as well as other process equipment, in electric power generating plants. According to the U.S. Geological Survey (USGS) [15], which makes a thorough dataset of water use available every 5 years, the total average water use in the United States was 408 billion gallons per day (Bgal/d) in 2000, with 85% of that being freshwater. Of the 408 Bgal/d, 195 Bgal/d is used in thermoelectric power applications. Fresh water constitutes 70% of that consumption rate and the remaining 30% is saline water, primarily in coastal power plants.

Notably, as seen in Figure 3, the water used in power generation has remained relatively constant since 1985, despite a significant increase in generating capacity. This is due to a significant increase in the water "efficiency" of power generation, from 63

gal/kWh in 1950 to 21 gal/kWh in 2000 [16]. This is a result, in large part, of a transition from once through cooling to closed loop cooling. Thermal electrical power generating plants have been the largest net user of water since 1965, when they surpassed irrigation.

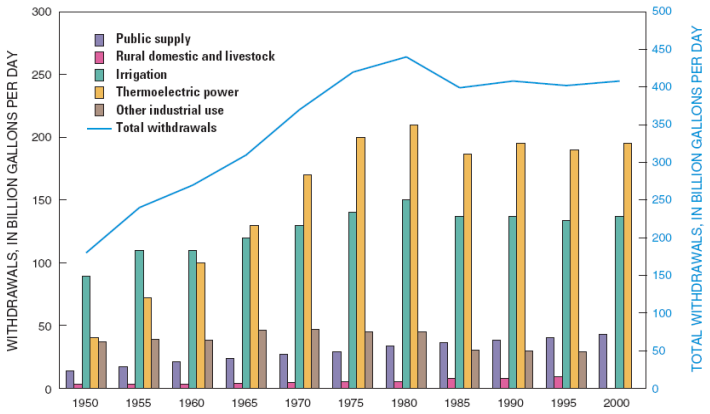

Figure 3: Trends in total water withdrawals by category [15]

Power plants use 136 Bgal/d of freshwater, just slightly less than irrigation at 137 Bgal/d. Other consumers, such as public supply and industrial, pale in comparison at only 43 Bgal/d and 20 Bgal/d respectively. Power plants account for 39% of total freshwater withdrawals, 52% of fresh surface water withdrawals, and 96% of saline water withdrawals, according to USGS data.

In increasingly prevalent closed-loop cooling systems, water is withdrawn from a source, circulated through process heat exchangers, cooled, and used again in a continuous loop. These systems make use of evaporation in cooling towers and thus have a higher consumptive use than once-through systems. Some water is lost to evaporation in this process, which results in an increasing concentration of dissolved and suspended solids in the remaining water. These particulates, at a high concentration, can lead to scaling, fouling, and/or corrosion. As a result, some amount of freshwater is continually reintroduced; this process is known as blowdown. Through the use of new heat exchanger materials resistant to these detrimental processes, plants would be able to operation at significantly higher levels of contaminants, significantly reducing fresh water consumption of such power plants.

Saline water consumption in the United States is associated primarily with the cooling needs of coastal power plants, and used in once through cooling (OTC). Higher grade materials must be used to prevent corrosion, often glass-reinforced polyester piping and metals such as titanium and stainless steel in the heat exchangers. Lower water temperatures in the ocean can increase the output of a power plant on the order of 1% [17], as opposed to siting a plant on a river or lake. Oceans also have the benefit of more gradual temperature variations. Despite this, there is a large push for new plants to adopt alternative cooling techniques, due to the vast amounts of water withdrawn by OTC, as well as environmental concerns from the entrainment of aquatic organisms as well as the introduction of large levels of warm water to lakes and rivers. Alternative techniques include closed loop cooling, with freshwater as makeup water, evaporative cooling towers, or air cooling, but all include significant added costs due to a lack of thermal efficiency as opposed to OTC with seawater.

1.6 Objectives

Thermally conductive polymer composites are a promising advanced heat exchanger material. In order to gain industry acceptance, significant work must be done to demonstrate the viability of such composites. The objectives of this thesis are to begin the steps towards such acceptance, through the following assessments:

1. Demonstrate potential energy savings through the use of polymer composites, as compared to existing corrosion resistant metals.
2. Quantify the required thermal conductivity for a viable gas liquid heat exchange.
3. Establish reliable optimization routines that allow for significant mass and energy savings in the design of corrosion resistant heat exchangers.
4. Experimentally verify performance of commercially available polymer composites through the testing of a prototype heat exchanger. This should also serve to establish appropriate methodologies for analytically and numerically predicting the real-world performance of polymer composites.
5. Understand the effects of anisotropic thermal conductivities present in polymer composites, both how such anisotropy develops and how it affects thermal performance.

1.7 Overview of Thesis

This thesis will provide an overview of the characterization, design, and optimization of thermally enhanced polymer composite heat exchangers. Divided in 8 chapters, it beings by introducing typical applications of the heat exchangers studied here, and explore the motivation behind this work. Chapter 2 will discuss the unique properties of polymers, beginning with existing polymer heat exchangers, and then focusing on the challenges involved with the addition of fillers. Chapter 3 will study the general design and optimization of low thermal conductivity polymer fins. Chapter 4 will present the heat exchanger analysis methods used, as well as several metrics and techniques for minimum energy design of heat exchangers, including the total coefficient of performance and least material relations. Numerical analysis methods will also be presented. Chapter 5 will then study the parametric behavior of a representative finned-plate heat exchanger module, and compare this geometry to two alternative heat exchanger designs. Chapter 6 will expand upon the work of Chapter 3, applying the concepts of design for minimum mass to a complete heat exchanger for LNG applications in Persian Gulf waters. Chapter 7 will then cover the experimental verification of the thermal performance of a polymer composite heat exchanger, including comparisons to an unfilled polymer heat exchanger, as well as the temperature distribution within the fins of an injection molded heat exchanger with anisotropy. A summary of contributions and proposed future work is discussed in Chapter 8.

Chapter 2: Polymer Properties and Attributes

2.1 Review of Polymer Heat Exchangers

In many industrial applications, including seawater heat exchangers, as well as food and chemical processing, and oil and gas refining, corrosion resistant materials must be used. Regrettably, these materials - including palladium-stabilized titanium, copper-nickel alloys, and stainless-steels - possess relatively low thermal conductivities, typically in the range of 5 to 40 W/mK, far lower than that of conventional heat exchanger materials, such as aluminum (170W/mK) and copper (300W/mK), but in the range of corrosion –resistant materials such as stainless steel (17 W/mK) and titanium (20 W/mK). In many marine systems using seawater as the ultimate coolant, its highly corrosive nature leads to the use of two-stage heat exchange, with tempered water in an intermediate closed-loop cycle [11]. Removal of this intermediate heat exchanger loop and direct reliance on seawater could greatly reduce the complexity of heat exchange and offer a significant savings in expended and invested energy. Additionally, the energy invested in manufacturing titanium is over 3 times that of aluminum and over 13 times that of copper [18-20]. Consequently, the use of titanium to facilitate direct cooling with seawater incurs a significant energy penalty; motivating the exploration of other corrosion-resistant materials, such as polymers, for seawater heat exchangers.

Zaheed and Jachuck reviewed the availability and range of use of several commercial polymer heat exchangers [14]. The use of thin polymer films is studied to address the thermal conductivity deficiencies of most polymers. Several types of polymers offer potential for heat exchanger applications; strength, viable operating temperature, chemical inertness, and water absorbency are all factors considered when selecting a polymer. Typical polymers used include PVDF (polyvinylidene fluoride, for highly corrosive applications), Teflon/PTFE (polytetrafluoroethylene, known for its chemical inertness), PE (polyethylene, due to its very low cost), as well as polypropylene. Polypropylene's strong resistance to seawater corrosion led to its use in the Ocean Thermal Energy Conversion (OTEC) heat exchangers [13]. The common characteristic of all of these polymers is a thermal conductivity one or two orders of magnitude below conventional corrosion-resistant metals.

Alternatively, thermally-enhanced polymer composites, filled with pitch-based, carbon micro fibers that raise the thermal conductivity by one-to-two orders of magnitude, are believed to make seawater polymer heat exchangers a viable approach. It must be noted, however, that the thermal conductivity and structural properties of such polymers are dependent on the fiber orientation and geometry, leading to anisotropy in the heat exchanger walls [21].

Several manufacturers developed commercial heat exchangers based on a range of polymers. Configurations typical of metal heat exchangers are used, but a larger heat transfer area is often necessary. Polymer plate, shell and tube, and coil heat exchangers are all readily available, as well as corrugated film heat exchangers, which add ridges in the polymer to increase rigidity, but maintain a very thin wall, to minimize the thermal resistance due to the low conductivity.

One benefit of polymers is flexibility in manufacturing; A Swedish Company, AB SEGERFRÖJD [22], sells a polypropylene heat exchanger of extruded polymer sheets, welded together to minimize thermal resistance and ensure an airtight seal. These heat exchangers are also easily recycled, because they are built entirely of a single material, using no glue or sealants. Nylon has proven to be a successful material for shell and tube heat exchangers, especially for solar water heating applications. Liu & Davidson showed nylon was an advantageous material in this case due to its high strength, allowing for a higher ratio of diameter to wall thickness [23]. The nylon polymer also facilitates the rapid adoption of technologies such as solar hot water, due to its significantly lower cost than more conventional copper tubing. A Texas based company; Power Cold has commercialized this technology by developing a fluid cooler using a high strength nylon material developed by DuPont for heat exchanger tubing. The polymer doesn't corrode like metals do in this application, and the increased smoothness reduces the potential for scale to bind to the surface [24]. Fluorotherm uses PTFE and PVDF to manufacture immersion heat exchangers for use in high temperature, highly corrosive applications [25]. These polymers are used in chemical processing and applications where high purity is required, such as semiconductor

wafer processing. Fluorotherm is able to bend and shape these coils and to manufacture them with flexibility, avoiding kinks in the tubing.

Zaheed and Jachuk [14] discuss several additional applications of polymer heat exchangers. Seawater desalination is a clear application, due to the highly corrosive properties of the water. Similarly, they are used in the food industry due to chemical inertness and resistance to corrosion and fouling. Polymers are also being investigated to reduce both cost and weight of absorption chillers [26]. Others have taken advantage of the sometimes detrimental water absorption properties of polymers to develop a heat and moisture exchanger between two streams of air. Such materials could replace more costly desiccant wheels in building applications [27], and facilitate energy recovery from exhaust air streams.

In order to facilitate the use of polymers in space-constrained, high heat flux environments, higher thermal conductivities will be required. Several companies have begun developing and commercializing thermally enhanced polymer composites, using pitch-based carbon fibers or graphite flakes [28, 29]. Bar-Cohen and Bahadur have investigated the viability of PPS composite electronic heat sinks, with thermal conductivities up to 20 W/mK, and shown comparable performance to aluminum heat sinks in air cooling applications, and significantly greater performance on a mass basis [30]. Such heat sinks have yet to gain much traction in electronics cooling, likely due to the high-cost of initial samples of the polymers manufactured in small batches, as well lack of perceived benefits over typical heat exchange metals. In the future, while corrosion is not a major risk in electronics, the increased manufacturing flexibility may allow polymer heat exchangers to be designed with geometries more suited to the relevant application than metals. An injection molded heatsink would also likely have a lower cost in high volume production than an aluminum heatsink, of comparable thermal performance. This could become a major benefit for polymer heat sinks in an industry with significantly decreasing margins.

The application of thermally enhanced polymers to gas liquid heat exchangers, specifically seawater heat exchangers for natural gas liquefaction, will be studied here. The corrosion resistance of the polymer is highly advantageous in this case, as existing shell-and-tube heat exchangers frequently fail due to corrosion and scaling within a year [8]. With comparable thermal performance to existing materials, such thermally conductive polymer heat exchangers could provide significant savings simply by requiring fewer replacements, and less plant downtime. The lower density of these polymers would also likely reduce manufacturing and transportation costs. Further work is needed to enhance the thermal conductivity of such polymer composites even more, if such heat exchangers are expected to be used in liquid-liquid applications.

2.2 Effects of Fillers on Composite Properties

A standard polymer has a very low thermal conductivity, on the order of 0.25 W/mK. To enhance this value, fillers are added, typically carbon fiber. Typical values for the thermal conductivity of pitch-based carbon fiber are 500 W/mK. The composite thermal conductivity is highly dependent on both the volume fraction of the fibers and their orientation.

2.2.1 Anisotropy

Because the composite conductivity is dominated by the highly conductive carbon fibers, it is highly anisotropic. The literature reveals that pin-fin composites of pitch-based discontinuous fibers can reach axial conductivities of up to 100 W/mK, with radial conductivities as low as 0.4 W/mK [21]. In reality, Bahadur measured axial conductivities up to 16 W/mK for a commercially available PPS composite, with orthogonal conductivities as low as 2.7 W/mK. Results for a plate fin will be discussed in Chapter 3.

For injected molded parts, the conductivity is highly dependent on the molding configuration. Carbon fibers will tend to align themselves with the direction of the flow field.

2.2.2 Nielsen Model

The original model for the effective thermal conductivity of a composite polymer was proposed by Nielsen [31]. The validity of this model has been confirmed by several studies [32, 33] and is given as:

$$\frac{k}{k_1} = \frac{1 + AB\phi_2}{1 - B\varphi\phi_2} \tag{1}$$

$$A = k_E - 1 \tag{2}$$

$$B = \frac{k_2 / k_1 - 1}{k_2 / k_1 + A} \tag{3}$$

$$\varphi = 1 + \left(\frac{1 - \phi_m}{\phi_m^{\,2}} \right) \phi_2 \tag{4}$$

where 'k', 'k_1', and 'k_2' are the composite, polymer resin, and filler thermal conductivity, respectively. 'k_E' is the Einstein coefficient, a function of aspect ratio and orientation of the fibers. Nielsen gives typical A values (Table 3) for various fillers, limited on the high end by the quantity 2L/D. An A value as low of 0.5 is seen for the heat flow across fibers. ϕ_2 is the filler volume fraction, and ϕ_m is the maximum packing fraction (Table 4).

Filler type	Direction of heat flow	Aspect ratio	A
Cubes	Any	1	2
Spheres	Any	1	1.5
Random fibers	Any	2	1.58
Random fibers	Any	4	2.08
Random fibers	Any	6	2.80
Random fibers	Any	10	4.93
Random fibers	Any	15	8.38
Uniaxially oriented fibers	Parallel to fibers	---	2L/D
Uniaxially oriented fibers	Perpendicular to fibers	---	0.5

Table 3: A values for the Nielsen Model as a function of filler type and aspect ratio [31]

Filler shape	Type of packing	ϕ_m
Spheres	Hexagonal close	0.7405
Spheres	Face centered cubic	0.7405
Spheres	Body centered cubic	0.6
Spheres	Simple cubic	0.524
Spheres	Random close	0.637
Spheres	Random loose	0.601
Rods or fibers	Uniaxial hexagonal close	0.907
Rods or fibers	Uniaxial simple cubic	0.785
Rods or fibers	Uniaxial random	0.82
Rods or fibers	Three dimensional random	0.52

Table 4: Maximum packing fraction values for use in the Nielsen Model [31]

Equation (1) results in a quadratic equation for ϕ_2, and thus the filler volume fraction, needed to achieve a specified thermal conductivity can be determined. Discussion in section 2.4 will address the relationship between filler volume and the amount of invested energy in the composite.

$$\frac{\frac{k}{k_1}B(1-\phi_m)}{\phi_m^{\,2}}\phi_2^{\,2} + (AB+\frac{k}{k_1})\phi_2 + (1-\frac{k}{k_1}) = 0 \qquad (5)$$

Fiber volume fractions for commercially available thermally conductive polymers have been experimentally determined to reach 70% for some samples [34]. This value would imply a maximum packing fraction of 82%, correlating to a random uniaxial packing arrangement. The value of 'A' in the Nielsen relation was chosen to equal 19 so as to fit a measured axial thermal conductivity of 20 W/mK at a reported fiber volume fraction of 70% [35].

To better understand the behavior of the Nielsen model, a parametric study was performed. Figure 4 shows how the composite conductivity increases rapidly with filler volume fraction. Since the filler conductivity is several orders of magnitude larger than the polymer matrix, this is the dominating parameter. Despite this, the Nielsen model still predicts a composite conductivity less than 5% of the filler conductivity at a volume fraction of 75%. Figure 5 shows a very linear relation between the composite conductivity and the polymer conductivity. This is important because the studied range of conductivities, from 0.1 W/mK to 0.5 W/mK is a common range for polymers. It is apparent that the choice of polymer matrix can have a large effect on the composite conductivity. Doubling the polymer conductivity from 0.2 to 0.4 effectively doubles the composite conductivity for the conditions shown, from 4 to 8 W/mK.

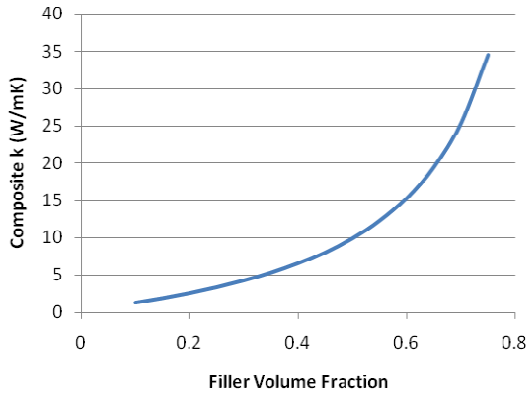

Figure 4: Composite conductivity as a function of filler volume fraction. k_1=0.22 W/mK, k_2 = 700 W/mK, Φ_m=0.82; A=40; Uniaxially oriented fibers

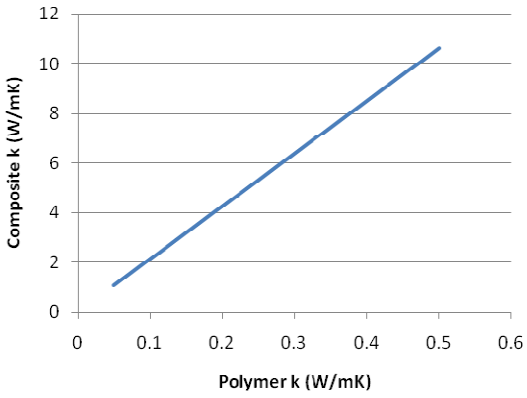

Figure 5: Composite conductivity as a function of polymer matrix conductivity. k_2 = 700 W/mK, Φ_2=0.325, Φ_m=0.82; A=40; Uniaxially oriented fibers

The following two figures display the importance of the arrangement of the filler particles within the polymer matrix. Different geometrical arrangements have a large effect on the maximum packing fraction. As shown in Table 4, a three dimensional random arrangement has a maximum packing fraction of only 0.52, while uniaxial simple cubic arrangement brings this up to 0.785. Figure 6 shows that – for a constant volume fraction of pitch based carbon fibers – the composite conductivity decreases rapidly with maximum packing fraction, beginning to level off at about 0.7. Conversely, Figure 7 shows that the composite thermal conductivity increases as the volume percent increases relative to the maximum packing fraction. These two figures together imply that an increasing fiber-to-fiber spacing rapidly reduces the composite conductivity, due to the low polymer matrix conductivity inhibiting heat conduction from fiber to fiber.

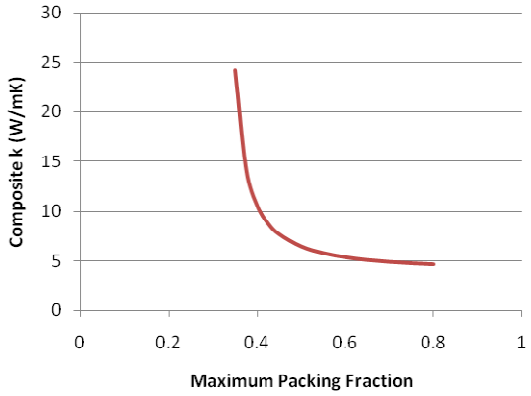

Figure 6: Composite conductivity as a function of maximum packing fraction. k_1=0.22 W/mK, k_2 = 700 W/mK, Φ_2=0.325; A=40; Uniaxially oriented fibers

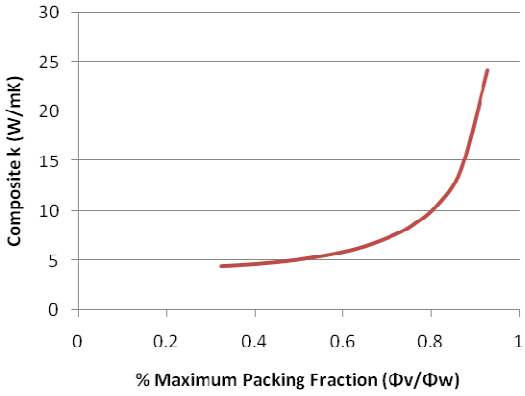

Figure 7: Composite conductivity as a function of percent of maximum packing fraction. k_1=0.22 W/mK, k_2 = 700 W/mK, Φ_2=0.325; A=40; Uniaxially oriented fibers

The Nielsen model provides a strong, experimentally verified method for predicting the effective thermal conductivity of polymer composites, and will be used throughout this study.

2.3 Behavior of Composites in Seawater

Mohd Ishak and Berry [36] studied the hydrothermal aging of carbon fiber composites of Nylon6,6. The tensile properties of the composite studied were detrimentally affected by water absorption, but still – in this degraded state – the material was found to be significantly stronger than the base nylon polymer. They showed that the tensile modulus for a nylon composite with a 27% volume fraction of carbon fibers decreased from an unaged value of 28.9 GPa to a value of 12.7 GPa. This can be compared to values of 110 GPa for a typical titanium alloy [37] or 68.9 GPa for aluminum [38]. With a no carbon fibers, the polymer composite is far more compliant, 3.4 GPa initially, down to 0.63 after aging. They also experimentally demonstrated that, as expected, equilibrium moisture content decreases with increasing fiber volume fraction.

2.4 Energy Content of Carbon Fiber Polymer Composites

Two thermally conductive polymers were chosen to be representative of commercially available products [PolyOne 28]. Determination of the energy values for thermally conductive polymers is more complex than for the conventional and corrosion-resistant metals discussed above. Suzuki and Takahashi [39] give an energy content of 24 MJ/kg for the polypropylene polymer used in this study and a much larger value of 286 MJ/kg for carbon fiber. These values include both the raw material production and the processing and assembly of the polymer and the fibers. It is to be noted that this 2004 energy content value for the fibers represents a significant decrease from the 1999 reported energy content of 478 MJ/kg [39]. Moreover, the energy content of pitch based, discontinuous fibers and graphite flakes, typically used in thermally enhanced polymers, may decrease further, as production volumes increases and as lower cost, lower energy content stocks, e.g. by-products of coal-gas production, are used as the raw material [19].

To determine the energy content and thermal properties of a polymer composite, the mass fraction of the filler, ϕ_W, - as well as other geometric details - must be known. The energy content is then:

$$E_M = 286\phi_W + 24(1-\phi_W) \tag{6}$$

$$\phi_W = \frac{1.75\phi_2}{1.75\phi_2 + 0.85(1-\phi_2)} \tag{7}$$

Where ϕ_2 is the filler volume fraction, as appearing in the Nielsen equation, discussed in Section 2.2.2. As shown in Figure 8, the energy content of a polymer composite, in MJ/kg, can rapidly increase from 85 MJ/kg for a thermal conductivity of 1 W/mK to approximately 215MJ/kg for a conductivity of 8 W/mK, at which point the plot begins to plateau, as the energy content approaches that of the carbon fiber itself.

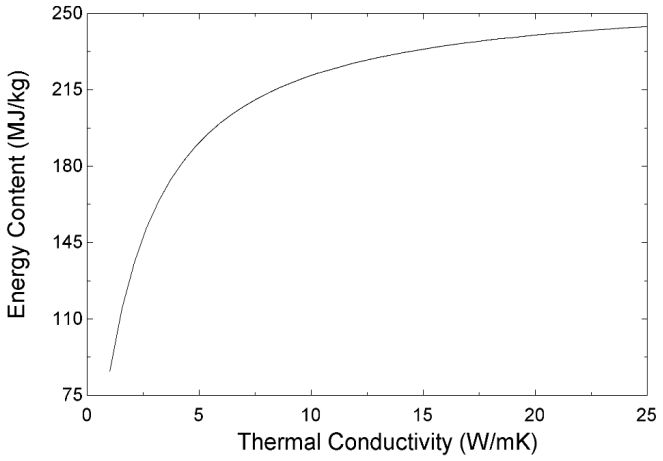

Figure 8: Polymer Composite Energy Content. k1=0.25 W/mK, k2 = 500 W/mK, Φ2=0.325, Φm=0.82; A=19; Uniaxially oriented fibers. $E_{m,fibers}$=286 MJ/kg, $E_{m,polymer}$=24 MJ/kg

The fact that the energy content varies with thermal conductivity provides an interesting opportunity for thermal optimization. When the thermal resistances of process fluids dominate, a low thermal conductivity will be sufficient to provide acceptable thermal performance. The material thermal conductivity can be chosen specifically for the application, minimizing the use of expensive (in both energy and dollars) carbon fibers.

Chapter 3: Study of Low Thermal Conductivity Plate Fins

3.1 Classical Models

The geometry for a single fin of the heat exchanger to be studied is given in Figure 9:

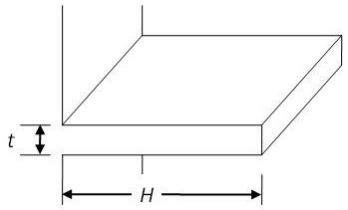

Figure 9: Single longitudinal fin
of rectangular profile

The heat transfer rate for a single fin is given by the simple relation

$$Q = \eta h A_{fin} \theta_b \tag{8}$$

where θ_b is the excess temperature at the base. To incorporate the heat transfer from the base area associated with each fin, the equation can be modified:

$$Q = (\eta A_{fin} + A_{base}) h \theta_b \tag{9}$$

The fin efficiency of such a rectangular plate fin with height H and an assumed adiabatic tip is given by

$$\eta = \tanh(mH) / mH \tag{10}$$

where m is the fin parameter

$$m = (2h / k_{fin} t)^{1/2} \tag{11}$$

where k_{fin} is the fin thermal conductivity, t the fin thickness, and h the average heat transfer coefficient. Harper and Brown [40] showed that to correct for an adiabatic tip assumption, the fin height could be corrected by $H_c=H+t/2$. Schneider [41] showed that this approximation is nearly identical to the rigorous solution at values of $ht/k < 0.0625$, and within 7.6% for $ht/k < 0.25$.

The fin heat transfer rate for a fin with a convecting tip [42] can be given as

$$q = M \frac{\sinh(mL) + (h / mk)\cosh(mL)}{\cosh(mL) + (h / mk)\sinh(mL)} \tag{12}$$

$$M = \sqrt{hPkA_C}\,\theta_b \tag{13}$$

with P being the perimeter of the fin, A_c being the cross-sectional area of the fin (length times thickness) and θ_b being the excess temperature.

The overall efficiency, without need for the Harper Brown assumption, can be found by dividing (12) by maximum heat transfer of the fin, given in equation (14). This assumes the entire fin area is at the temperature of the base, and thus adding fin area is equivalent to adding area directly to the base.

$$q_{\max} = hA_f\theta_b \tag{14}$$

Conventional fin analysis follows the Gardner assumptions and neglects any temperature variations through the thickness of the fin [43] The validity of this is assessed through the magnitude of the Biot number, given in equation (15). It was shown by Bahadur [35] that the classical 1D equations were valid for Biot numbers of 0.4, but at higher values the classical equations significantly overpredict the heat flow rate. In this case more complex equations are required for 2D conduction. Bahadur also investigated the effects of

orthotropic fins, a relevant consideration in thermally enhanced polymers, where the orientation of the carbon filler can make the in-plane and out of plane conductivity differ by more than an order of magnitude. Bahadur was able to use the least-material relations typically used for 1D heat flow in combination with equations for orthotropic pin fin heat flow and predict heat transfer for an orthotropic pin within 7%, up to a Biot number of 35 [35].

$$Bi = \frac{ht}{2k} \tag{15}$$

The thermally enhanced polymer fins of greatest interest in this study have a thickness of 1-2mm, with a conductivity of roughly 5W/mK. In typical gas side heat transfer coefficients of 30-60W/m^{2}K, this results in Biot numbers of 0.003 to 0.012, well below the limiting value for the one-dimensional approximation of 0.4 determined by Bahadur.

3.2 Least Material Design

Commercial heat exchangers are frequently classified by weight, volume, and cost. In a world concerned about future energy supplies, as well as the global environmental effects of energy production and use, optimally-designed, efficient heat exchangers will play an ever growing role in energy conversion systems. The required formation and fabrication (i.e. manufacturing) energy is rapidly becoming a key consideration in this selection process. It is highly desirable to design heat exchangers that minimize all of these quantities while providing the required performance. The design of optimum, least-material fins for high thermal conductivity materials, such as aluminum and copper, was pioneered by Kern and Kraus [44] and applied to the development of least-material heat sinks by Iyengar and Bar-Cohen [45] for natural convection and Bar-Cohen et al. [30] for forced convection cooling of electronic components.

For forced convection cooling it is important to consider entropy generation, as first discussed by Bejan [46]. Heat transfer from a high temperature heat source, such as a hot gas, to a low temperature sink, such as water or other coolant, represents a potential for useful work to be done. The maximum amount of work is given by a Carnot efficiency,

as discuss in Ogiso [47]. As this heat is transmitted in total to the lower temperature fluid, it will always be accompanied by the generation of entropy. Entropy generation also results from fluid pumping power to overcome frictional dissipation. The total entropy generation rate can then be written as the sum of these two components, as discussed in Iyengar & Bar-Cohen [48]. This Entropy Generation Minimization (EGM) methodology has been used by several research groups [48-52] to optimize plate-fin heatsinks.

The EGM method accounts for thermal availability loss due to the temperature difference as well as the pumping power, but does not account for entropy generation in the creation the fins themselves. This energy makes up a large fraction of the total lifetime energy consumption of a heat exchanger, especially for heat exchangers with a short service life or built of high fabrication energy, corrosion-resistant materials [53]. The total coefficient of performance (COP_T) expands the COP metric to include the energy invested in manufacturing and transporting a heat exchanger as well as the pumping power. Optimization to minimize the total energy consumed can lead to lighter-weight devices with lower material and manufacturing cost. The least-material optimization, explored here, focuses on achieving the maximum heat transfer per unit mass. In design for sustainability, mass is most directly associated with manufacturing and transportation costs, as well as invested energy. Optimization of extended heat transfer surfaces, as done here, will directly correlate to several environmental, as well as economic, benefits.

Traditional least material optimization techniques are done for a single fin. Bar-Cohen and Jelinek [54] showed that the results of such an optimization could be applied to an array of individually optimum fins. This approximation is appropriate for dense fin arrays of high-thermal conductivity materials, where most of the heat transfer is due to the fins. In low thermal conductivity materials, a significant portion of the heat transfer may come through the interfin spacings. Bar-Cohen and Jelinek [54] developed an array-optimum relation by the addition of a term incorporating this effect. In very low thermal conductivity fins, 2D conduction in the base and in the fin may play a role. The following section will attempt to show how the least material relations may be used to optimize such fins.

3.2.1 Least Material Analysis

Based on an analytical derivation, Kern and Kraus [44] showed that the mH product for all least-material plate fins is a constant value, 1.4192. Since the fin efficiency is only a function of this product, as in Eq.14, the efficiency of the least material fin also attains a fixed value of 0.627. Inserting a value of 1.4192/H for m in Eq. (10), yields the equation for the least-material fin thickness.

$$t = \frac{2h}{k}(0.497\,H^2) \tag{16}$$

A theoretical relation for the fin dimensions providing the optimum efficiency of a least-material array was developed by Bar-Cohen and Jelenik [54] and is given in equation (17).

$$mH_{opt} = 1.4192 + 1.125\frac{hH}{k} \tag{17}$$

This equation attempts to account for the effect of heat transfer in the interfin area on the least material thickness by modifying the optimum mH product. This can be used with Eq. (13) to derive the equation for the fin thickness for an array of least material fins:

$$t_{opt} = \frac{2h}{k}\left(\frac{1.4192 + 1.125\,\frac{hH}{k}}{H}\right)^{-2} \tag{18}$$

Eq. (18) reveals that the impact of heat transfer through the interfin spacings is to produce thinner optimal fins than determined with Eq. (16). This corrected optimal fin thickness is within 0.5% of the optimal thickness of a single fin, given in Eq (16), for high thermal conductivities of 300 and 150 W/mK, for a fin height of 10mm and heat transfer coefficients from 10 to 65 W/m^{2}K. However, as the conductivity decreases, heat transfer through the base becomes more important and the added term in Eq. (18) has a larger impact. For copper-nickel alloy and titanium fins, with conductivities of 40 and 20 W/mK, the difference is 1.5% and 3%, for fins of the same dimensions and subjected to

these heat transfer coefficients. For the thermally enhanced polymers with conductivities of 10 and 5 W/mK, this correction is even more important, a difference of 6% and 12% is seen, respectively. And for the unfilled polymer, with a very low thermal conductivity of 0.25 W/mK, the difference is on the order of 400%. These differences are illustrated in Figure 10, with the solid lines representing the array-based least material thickness, and the dotted lines the isolated fin least-material thickness. The thickness can be seen to increase with increasing heat transfer coefficient, as does the separation between the two relations. Lower conductivities also lead to thicker fins.

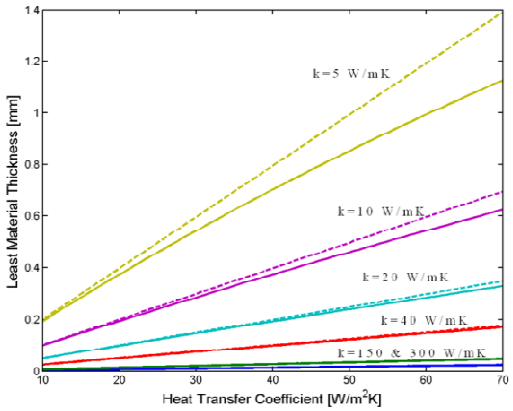

Figure 10: Least material fin thickness as a function of heat transfer coefficient and thermal conductivity, H_{fin}=10mm

3.2.2 Results of Least Material Analysis

3.2.2.1 Single Fin

The validity of the least-material fin aspect ratio, Eq. (16), was initially verified by analysis of a single longitudinal plate fin (Figure 11-Figure 12) with constant profile area and heat transfer coefficients in the range anticipated for the LNG polymer heat exchanger**.** With a constant profile area, the mass of the fin is fixed and the least material fin is thus the fin that achieves the maximum heat transfer rate. For a high conductivity material, the least material relations will lead to slender, tall fins, whereas for a low conductivity polymer thicker fins will be preferred. The value of the optimum ht/k ranges from 1.85^{-5} for k=300 W/mK to 0.236 for k=0.25 W/mK in the h=30 W/m^{2}K case. In the

high h and low k case, a value of ht/k 0.467 for k=5 W/mK is seen. Such a high heat transfer coefficient is not likely to be relevant for the cooling of a gas, such as methane.

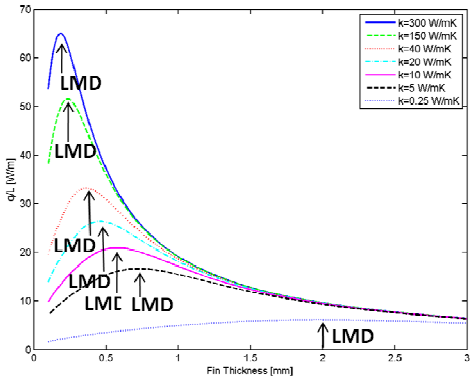

Figure 11:Single fin heat transfer rate A_p=8 mm^2, h=30 W/m^{2}K, θ_b=40K

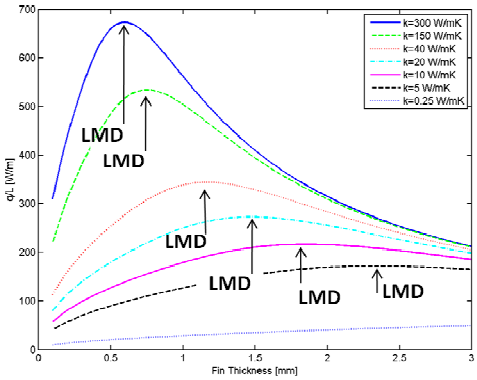

Figure 12:Single fin heat transfer rate, A_p=8 mm^2, h=1000 W/m^{2}K, θ_b=40K

The optimum thicknesses calculated by the least-material relation, Eq. (16) are noted in Figure 11 and Figure 12 as LMD, and show a strong correlation with the results through a range of thermal conductivities, from 300 W/mK down to 0.25 W/mK. The discrepancy between the thickness at which the peak heat transfer occurs in Figure 11 and Figure 12 and the analytical least-material thickness is less than 0.1% for both h=1000 W/mK and h=30 W/mK, shown in Table 5 and 6. The peak of each curve denotes the fin dimensions that yield the most efficient use of the given fin mass. The 0.25 W/mK thermal conductivity, representative of the unfilled polymer, is not shown in the h= 1000 W/mK case, as the predicted optimum thickness becomes much larger, 6.335 mm.

h=30 W/m^{2}K

k (W/mK)	*Peak Heat Transfer Thickness (mm)*	*LM Thickness (mm)*	*% Error*
300	0.185	0.185	0.0415
150	0.233	0.233	0.0381
40	0.363	0.363	0.0024
20	0.457	0.457	0.0055
10	0.576	0.576	0.0005
5	0.725	0.725	0.0049
0.25	1.968	1.968	0.0033

Table 5: Error in LM Relation**:** A_p=8 mm^2, h=30 W/m^{2}K, θ_b=40K

h=1000 W/m^{2}K

K (W/mK)	*Peak Heat Transfer Thickness* **(mm)**	*LM Thickness* **(mm)**	*% Error*
300	0.596	0.596	0.0094
150	0.751	0.751	0.0020
40	1.167	1.167	0.0004
20	1.470	1.470	.00096
10	1.852	1.852	0.0033
5	2.334	2.334	0.0078
0.25	6.335	6.335	0.0085

Table 6: Error in LM Relation: A_p=8 mm^2, h=1000 W/m^{2}K, θ_b=40K

3.2.2.2 Application Towards Fin Arrays

While single fin analysis provides insight into the thermal behavior of extended surfaces an entire array of fins is typically needed to enhance the heat transfer rate from the wetted surface of a heat exchanger. The modeling, analysis, and optimization of such fin arrays is greatly simplified if the one-dimensional, isotropic fin equations can be used to calculate the heat transfer rate of the individual fins. Bahadur has shown that for Biot numbers less than 0.4, the classical fin equations, for pin fins, and by implication for plate fins whose behavior is governed by a nearly identical governing equation, can be used with negligible error [35]. Figure 13 shows that, for the assumed working conditions of a methane-seawater heat exchanger and thermal conductivities from 300W/mK representing copper to 0.25 W/mK representing an unfilled polymer, the Biot number for fins placed on the methane side of the heat exchanger with fin counts greater than 2 fins/cm results in Biot numbers less than 0.4 and is thus sufficiently small to warrant use of the 1-dimensional, heat conduction assumptions.. At lower fin counts, and particularly at the low thermal conductivity of unfilled polymers, two-dimensional conduction effects may play an important role. It is to be noted that for these same unfilled polymer fins, for a fin pitch below 0.3 cm, the flow is turbulent, and the resulting higher heat transfer coefficient leads to a large Biot number**.**

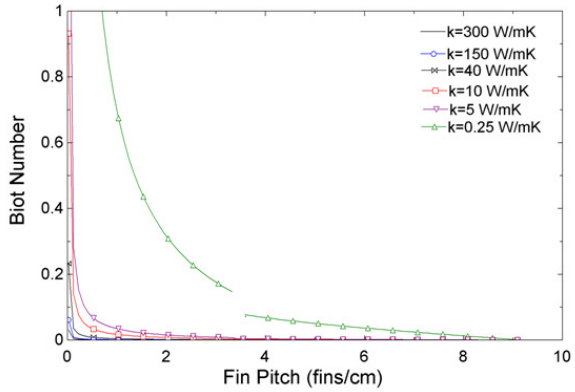

Figure 13: Biot numbers in a gas/liquid heat exchanger, for various thermal conductivities. L=W=1m, H_{fin}=10mm, Gas Pumping Power: 5W. t_b=1mm, θ_b =55K, variable fin thickness

If heat transfer from a relevant wetted area in a heat exchanger is to be enhanced through the addition of fins, it is expected that a significant fraction of the heat transfer will occur thru these fins. Figure 14 displays the fraction of the heat transferred from the wall to the flowing methane through the fins. It can be seen that for all but the lowest thermal conductivity, more than 80% of the heat transfer does occur through the fins for fin counts from 3 fin/cm to 8fin/cm. For higher fin counts, when fin thickness decreases due to the constant pumping power constraint, the relative importance of the fin heat transfer begins to fall. For the unfilled polymer, with a thermal conductivity of 0.25 W/mK, only 50-60% of the heat transfer is through the fins for much of the fin count range.

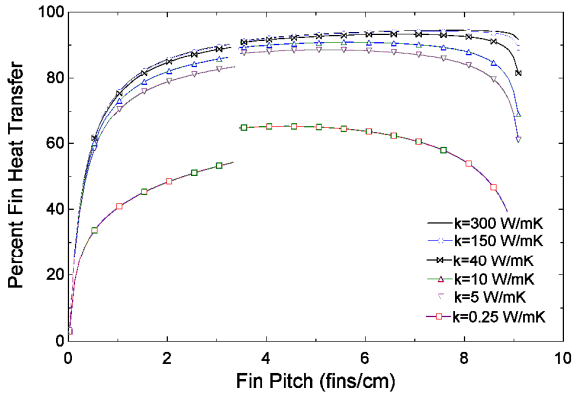

Figure 14: Fraction of heat transfer through fins, for various thermal conductivities. L=W=1m, H_{fin}=10mm, Gas Pumping Power: 5W. t_b=1mm, θ_b =55K

To find the fin thickness which maximizes the benefit of the mass used in the fin array, the variation of the heat transfer rate (per unit length) with fin thickness is determined and displayed in Figure 15, for a constant profile area and parametric values appropriate to the methane side of the seawater heat exchanger. In the previous case, the fin count and fin thickness was allowed to vary while holding pumping power constant. To verify the least-material thickness, a constant fin count of 500 fins (and thus a constant total profile area) is assumed. The least material efficiency of 0.627 is seen to accurately predict the optimum fin thickness nearly exactly for k=300 and 150 W/mK, within 1.4% for k=40 W/mK and 20 W/mK, 2.6% for k=10 W/mK, and 3.2% for k=5 W/mK. For a thermal conductivity of 0.25W/mK, when the heat transfer rate is nearly independent of fin thickness, the error jumps to 23.2%.

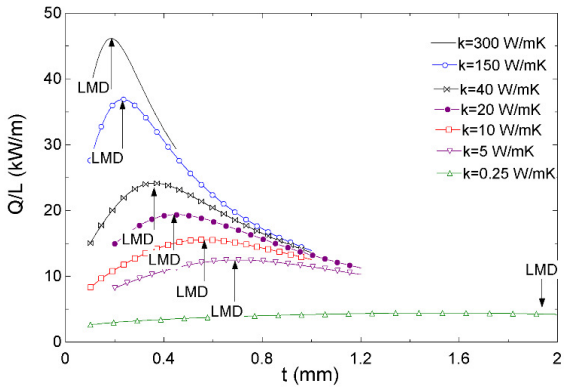

Figure 15: Heat transfer per unit length in a gas-cooled array, for various thermal conductivities. W=1m,A_p=8 mm^2, h=30 W/m^{2}K, θ_b =55K, N_{fins}=500, t_b=1mm

The methodology presented here shows that for a rectangular plate fin array with constant profile area fins, the single fin least material condition is a good approximation down to thermal conductivities as low as 5 W/mK. At the extreme end, with less than 15% of heat transfer through the fins, the optimum fin can be accurately found by using the heat transfer through the fins alone. This restricts the usefulness of the least-material condition to evaluation of existing heat exchanger designs, as opposed to a design tool for new heat exchangers. Error at low fin spacings and thermal conductivities can be reduced through a combination of an array-based least material relation, discussed further in Section 5.7.

Chapter 4: Heat Exchanger Thermal Analysis Methods

In this section, the calculation strategies for heat transfer and pressure drop are outlined. In addition, performance metrics for fin efficiency and least-material utilization are presented. A total Coefficient of Performance (COP_T) is defined to relate the total heat transfer achieved over the service life of the heat exchanger to both the lifetime pumping power and formation/manufacturing energy.

4.1 Heat Transfer Rate

4.1.1 Effectiveness-NTU Method

Following the ε-NTU methodology [42], the heat transfer rate for a counterflow heat exchanger is given by equation (19).

$$q = \varepsilon C_{\min}(T_{i,m} - T_{i,w}) \tag{19}$$

Using the difference between the respective inlet temperatures of the two fluids and C_{min}, the minimum of the methane and seawater heat capacities, the effectiveness, ε, and number of transfer units (NTU) are determined according to the following relations:

$$\varepsilon = \frac{1-\exp[-NTU(1-C_r)]}{1-C_r\exp[-NTU(1-C_r)]} \quad (C_r < 1) \tag{20}$$

$$NTU = \frac{UA}{C_{min}} \tag{21}$$

$$UA = \frac{1}{R_t} \tag{22}$$

4.1.2 Thermal Resistance

R_t is the total thermal resistance, the inverse of the thermal conductance. The effective thermal conductance, UA (W/K), is calculated through the convection and conduction thermal resistance chains, as:

$$UA = \frac{1}{\frac{1}{n_o A_{t,m} h_m} + \frac{t_b}{k A_b} + \frac{1}{n_o A_{t,w} h_w}} \tag{23}$$

where h_m is the heat transfer coefficient on the methane side and h_w on the water side. $A_{t,m}$ and $A_{t,w}$ are the wetted areas on the gas and liquid side, respectively. The overall array efficiency η_o, calculated as a function of the individual fin efficiencies and the fraction of the base area occupied by fins, is discussed later.

Applying Eq. (23), it is found that in the case of the low thermal conductivity unfilled polymer (k=0.25W/mK), roughly two thirds of the thermal resistance occurs on the gas side, and the bulk of the remaining third is from the wall. For a 10 W/mK polymer composite, roughly 90% of the thermal resistance is due to the gas side. Since the convective resistance on the seawater side is nearly an order of magnitude below the gas side resistance, least-mass optimization of this seawater heat exchanger begins by nearly eliminating the fins on the water side, leaving widely-spaced fins to primarily meet the structural constraints of this finned-plate compact heat exchanger. Since the overall thermal resistance is dominated by the convective resistance on the gas side, it is these fins that need to be optimized for the highest heat transfer rate per unit mass. For purposes of the present study, the base plate thickness is assumed to be dictated by molding considerations and is taken to be constant and equal to 1mm.

4.1.3 Heat Transfer Coefficients

The value of the heat transfer coefficient appropriate for each configuration can generally be determined from available Nusselt number correlations. The finned plate heat exchanger examined in this study is comprised of parallel plate channels of various aspect ratios and length-to-diameter ratios. In the cases considered here, for a 1m long finned-array, flow is always fully developed within the first 20cm. Consequently, for hydraulic diameter-based Reynolds Numbers up to 2300, the fully-developed laminar flow correlations are used in this study, though they provide a somewhat conservative heat transfer rate. The correlation developed by Shah & Bhatti [55] for laminar fully developed flow in a rectangular duct of variable aspect ratio, α, with an isothermal boundary condition, is used in this study. This correlation reproduces tabulated results to an accuracy of 0.1%.

$$Nu_T = 7.541(1 - 2.610\alpha + 4.970\alpha^2 - 5.119\alpha^3 + 2.702\alpha^4 - 0.548\alpha^5) \qquad (24)$$

$$0 \le \alpha \le 1$$

Performance is studied over a large pumping power range. At large pumping powers, and thus Reynolds numbers, the flow can become turbulent. The Gnielinski [56] modification of the Petukhov correlation, providing an expanded Reynolds number range, is used to determine the turbulent heat transfer coefficients for the parallel plate channels under study when the Reynolds number exceeds 2300. An accuracy of ±10% can be expected.

$$Nu = \frac{(f/8)(\mathrm{Re}-1000)\,\mathrm{Pr}}{1.0 + 12.7\sqrt{f/8}(\mathrm{Pr}^{2/3}-1.0)} \qquad (25)$$

$$0.5 < \mathrm{Pr} < 2000 \qquad 2300 < \mathrm{Re} < 5\times10^6$$

Kays [57] showed that for values of the dimensionless axial distance x*, equation (26), greater than 0.05 the heat transfer coefficients are asymptotic to the fully-developed limit.

Typical values for the thermal entry length in this study are 0.09m on the methane side, and 0.18m on the seawater side, due to larger Prandtl and Reynolds numbers, well short of the 1m length examined.

$$x^* = \frac{x / D_h}{\mathrm{Re}\,\mathrm{Pr}} \tag{26}$$

Similarly, the hydraulic entrance length can be found when the dimensionless axial distance x^+, equation (27), is equal to 0.056. For the flow conditions here, the hydraulic entrance length is roughly 0.04m and 0.13m for the methane and seawater, respectively. Production scale heat exchangers can be expected to be even longer than the ones studied here, and further minimize the effects of developing flow.

$$x^+ = \frac{x / D_h}{\mathrm{Re}} \tag{27}$$

4.2 Pumping Power

The friction factor correlation for laminar fully developed flow in a rectangular duct is used [55]. Similar to the corresponding Nusselt number correlation, a high degree of accuracy can be expected, given as 0.05% by the authors.

$$f = \frac{24}{\mathrm{Re}}(1 - 1.3553\alpha + 1.9467\alpha^2 - 1.7012\alpha^3 + 0.9564\alpha^4 - 0.2537\alpha^5) \tag{28}$$

$$0 \le \alpha \le 1$$

For turbulent flow, the fully-developed friction factor, *f,* for smooth pipes is calculated using a correlation by Petukhov [58], with an accuracy of 10% in the given Reynolds number range.

$$f = (0.790 \ln \mathrm{Re}_D - 1.64)^{-2} \tag{29}$$

$$3000 \leq \mathrm{Re}_D < 5 \times 10^6$$

The pumping power required to overcome resistance to flow in a channel can be expressed as the product of the pressure drop and the volumetric flow rate:

$$P = \Delta p \cdot \dot{\forall} = \Delta p NSH u_m \tag{30}$$

where the pressure drop, Δp, is the sum of the friction and dynamic (entrance and exit) losses:

$$\Delta p = \left(f \frac{L}{D_h} + K_{L,entry} + K_{L,exit} \right) \left(\frac{1}{2} \rho u_m^2 \right) \tag{31}$$

Notably, this relation excludes a factor for developing flow. For the heat exchangers studied here, where the length is many times larger than the passage diameter, this is a reasonable simplification, though it may lead to the pressure drop and pumping power being slightly underestimated.

4.3 Performance Metrics

To best compare various heat exchanger materials, it is crucial to establish thermal performance metrics that take into consideration heat transfer rates, the volume and mass of the heat exchanger, and the energy required to both manufacture and operate the heat exchanger [5].

4.3.1 Volumetric Efficiency

One relevant metric is the volumetric efficiency, which reflects how much heat transfer a heat exchanger can accomplish in a given volume, typically given in kW/m^3.

$$\eta_V = q / V \tag{32}$$

While a smaller volume is generally preferable, and this is one reason plate heat exchangers are used as opposed to shell-and-tube heat exchangers [5], for energy considerations it is more important to consider the mass.

4.3.2 Mass Efficiency

In terms of energy, product mass is generally more important than volume, as densities can vary greatly over the range of heat exchanger materials. Therefore it is beneficial to define a mass efficiency, in terms of the amount of a heat transfer a heat exchanger can accomplish for a given mass:

$$\eta_m = q / m \tag{33}$$

4.3.3 Coefficient of Performance

While volumetric and mass efficiencies are directly correlated to the resulting heat transfer, it is helpful to define a coefficient of thermal performance (COP) for the heat exchanger. The COP relates the heat transfer rate to the pumping power invested and is presented here in units of kW/W.

$$COP = \frac{q}{P} \tag{34}$$

In this study typical values for the COP range from 0.25 to 1 kW/W.

4.3.4 Total Coefficient of Performance

The Coefficient of Performance is an important metric when pumping power is dominant. For seawater heat exchangers, exotic materials are often used but their service life is limited. The energy content of the material then becomes a larger component in the overall energy investment and, if the issue of sustainability is to be addressed [30, 59], it is important to define a Total Coefficient of Performance metric.

The previously-defined COP can be extended to address the energy invested in the heat exchanger mass by defining a $COP_{T,}$, relating the total heat transfer over the service life of the heat exchanger to both the lifetime pumping power and manufacturing energy:

$$COP_T = \frac{qt}{Pt + W_M} \tag{35}$$

Where manufacturing energy is defined as:

$$W_M = E_M \times m \tag{36}$$

The thermal properties, as well as embedded energy of formation and fabrication, vary widely from material to material (see Table 7). In corrosive environments, a common choice is titanium, and in some cases a copper-nickel alloy. Polymer composites may be more resistant to corrosion, and thus have a longer service life, yielding dramatic energy and cost savings for comparable thermal performance. An unfilled polymer will also be studied for reference, though the low thermal conductivities of base polymers do not facilitate their use in many high performance applications. Likewise, more typical heat exchange materials such as aluminum and copper are studied, despite their inherent susceptibility to corrosion.

Material	**Thermal Conductivity (W/mK)**	**Energy Content (MJ/kg)**	**Density (g/cm^3)**
Copper	300	72	8.9
Aluminum	150	306	2.7
Copper-Nickel	40	72	8.9
Titanium	20	1000	4.5
High-k Polymer Composite	10	222	1.61
Low-k Polymer Composite	5	191	1.54
Unfilled Polymer	0.25	24	0.85

Table 7: Thermal conductivity and energy content of relevant materials

Formation/Fabrication Energy – Metals: For metal seawater heat exchangers used in natural gas liquefaction, service life is rarely longer than a year, and as short as three to six months [ADGAS 60]. For such short service lives, the energy invested in manufacturing a heat exchanger can dwarf the lifetime energy expended in pumping [53]. Because of

this, it is important to design heat exchangers not only for efficient operation, but also for efficient production.

Values for the manufacturing energy for the materials studied here are derived from life cycle assessments, and include the energy required to mine, process, and form the material. Data provided by the Copper Development Association [61] gives the energy content of copper as 72 MJ/kg. In the absence of more specific data, this same energy value is used for copper-nickel alloy; though it is likely that the actual energy content of this alloy is slightly greater than 72 MJ/kg [SPINE Data Report 62]. Data provided by the LCA Committee of the Japanese aluminum industry [20] suggests that 306 MJ/kg are required to manufacture aluminum. For titanium, the production process is very energy intensive and requires an energy investment of 1000 MJ/kg [18].

Formation/Fabrication Energy – Polymers: Two thermally conductive polymers were chosen to be representative of commercially available products [PolyOne 28]. Determination of the energy values for thermally conductive polymers is more complex than for the conventional and corrosion-resistant metals discussed above. To enhance the inherently low thermal conductivity of the available polymers, fillers are added, typically pitch-based carbon fiber with a thermal conductivity of up to 800 W/mK, [63]. Suzuki and Takahashi [39] give an energy content of 24 MJ/kg for the polypropylene polymer used in this study and a much larger value of 286 MJ/kg for carbon fiber. These values include both the raw material production and the processing and assembly of the polymer and the fibers. This is discussed in further detail in section 2.4.

The values for energy content of each material can be multiplied by the density to developed a "Volumetric Heat of Formation" metric, demonstrating how much energy it takes to manufacture a fin of given volume, in GJ/m^3. This quantity is shown in Figure 16. The high energy content of titanium combines with a relatively large density to give it a value of 4.5 GJ/m^3, nearly 7 times that of copper-nickel and nearly 12 times that of the polymers. Copper, despite its low energy content, has highest value after titanium due to its large density. The high and low k polymers have volumetric heat of formation values

roughly half that of copper. A thermally enhanced polymer heat exchanger gains the benefits of both low levels of fabrication energy and low mass.

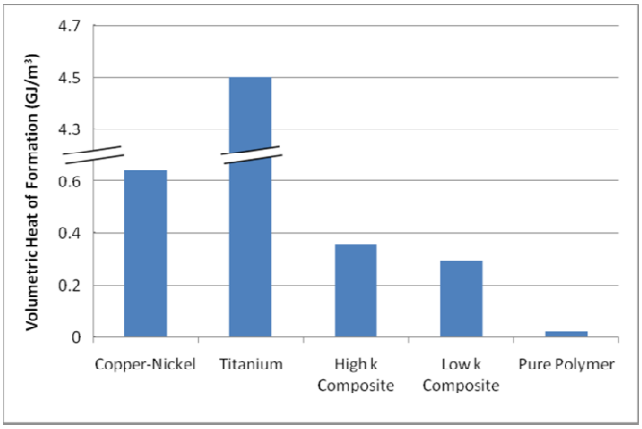

Figure 16: Volumetric Heat of Formation for several corrosion resistant materials

4.4 Numerical Modeling Methodology

Finite element modeling was performed to both study the anisotropic behavior a thermally enhanced polymer heat exchanger, and compare numerical predictions with experimental results. The numerical model developed was also used to study heat exchanger thermal performance, as well as parasitic heat losses from experimental components such as thermocouples.

4.4.1 Development of Numerical Heat Exchanger Module

A finned plate heat exchanger module, with dimensions identical to the prototype used in the experimental study, was generated using ANSYS Version 11 to numerically study the thermal anisotropy expected within the polymeric material. A three dimensional steady state analysis was performed.

Geometry

In order to construct the required geometry, volumes were generated for the base, a single fin, the corresponding epoxy layer above it, and the base on top of that. A new workplane was then generated using three keypoints on the inlet service, from which to generate cylinders representing the thermocouples. Cylinders were generated based on position, radius, and depth. The completed model is shown in Figure 17.

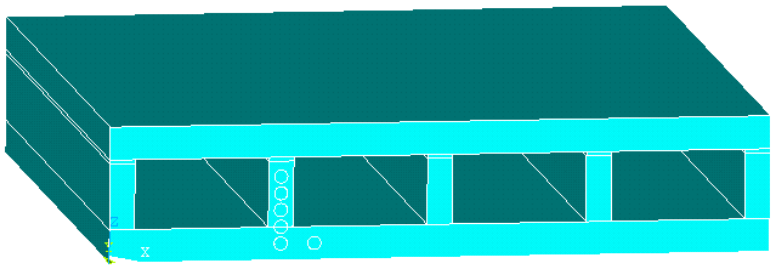

Figure 17: Heat Exchanger Numerical Module

Materials

To address the different conductivities of materials involved in the heat exchanger, from the stainless steel thermocouples to the low-conductivity epoxy layer, five materials were then defined, with x, y, and z conductivities specified for each (anisotropy was only addressed for two of these, the fins, and the base). These materials represented the epoxy, stainless steel thermocouple, polymer coated thermocouple, as well as independent conductivities for the base and fin polymer. Thermal conductivity as function of material and coordinate direction are summarized in Table 8.

	k_x (W/mK)	**k_y (W/mK)**	**k (W/mK)**
Polymer Base	4.7	4.7	1.5
Polymer Fin	2.3	2.3	6.2
SS Thermocouple	14	14	14
Polymer Thermocouple	0.5	0.5	0.5
Epoxy	0.1	0.1	0.1

Table 8: Thermal conductivities used in numerical model

Meshing

Volumes representing each material were meshed, using SOLID70 elements. This is a three dimensional tetrahedral thermal solid, comprised of 4 nodes with a single degree of freedom at each node. Orthotropic material properties can be used to define this element. Free surfaces of this element not subject to a boundary condition are assumed to be adiabatic. The introduction of small cylinders representing thermocouples required a fine mesh.. Smart sizing facilitated dynamic element sizing on a scale of 1 to 10, 1 being the finest mesh and 10 being the most course. In this case, a value of 4 was used for the base plate and fins, and 3 for the thermocouples and epoxy. Starting with a previously defined element size of 1mm, it locally overrides this value depending on proximity and curvature. A smartsize value of 4 scales the default mesh size by a factor of 0.4, while a smartsize value of 3 is slightly finer at 0.3. An expansion factor of 1 is used for both, meaning expansion of internal elements is not allowed. The final meshed geometry is shown in Figure 18. Approximately 1.5 million elements are generated by this process.

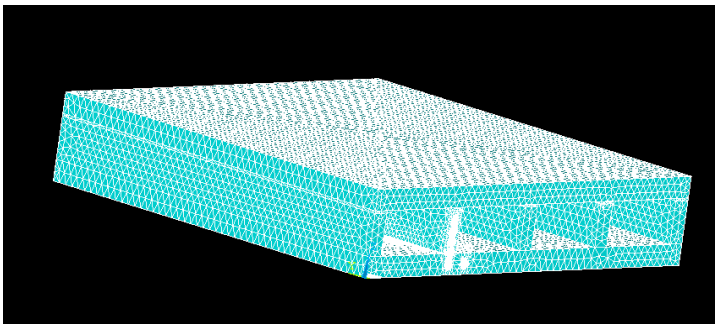

(a) Isometric view

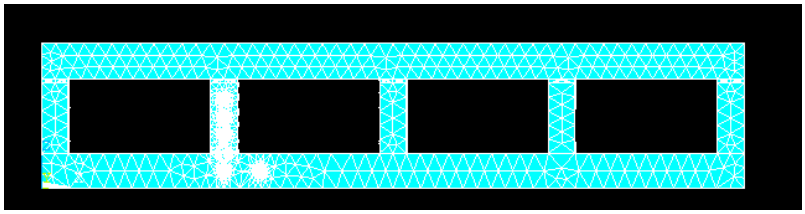

(b) Front view

Figure 18: ANSYS meshing of heat exchanger numerical module

Grid independence was assessed, and incrementing the smart sizing parameters from 4 to 3 to achieve a finer mesh resulted in no appreciable change in the heat transfer rate (under 0.6%), despite increasing the element count to 2 million.

Boundary Conditions

A convective boundary condition was applied to the interior of each channel by specifying a heat transfer coefficient and bulk temperature measured experimentally. In order to accommodate the drop in the bulk temperature across the length of the heat exchanger channels, a gradient was specified along the length of the channel. Based on inlet and outlet temperature measurements, this gradient was computed for each channel. The water temperature is assumed to be isothermal, and thus a constant temperature boundary condition is applied at the base surfaces representing the water temperature.

Solution

A static solution is generated, and the temperature distribution is plotted. Nodes at the bottom and top base plates are selected, and the "FSUM" command is used to find the heat transfer rate by summing nodal contributions.

It is important to note that the temperature values measured experimentally are not at the outside edges of the fins; the thermocouples are embedded 1cm deep into the polymer. To display the temperature at these locations, surfaces are generated at the relevant interior planes. These surfaces are then compared to experimental results. In Appendix 2, the ANSYS modeling code is given for reference.

All simulations were performed on a 3.0 Ghz Pentium IV computer, having 3.5 gigabytes of memory, and took 45-60 minutes per trial. A batch file was written in order to make the process easily repeatable.

4.4.2 Numerical Analysis of Anisotropic Plate Fins

The orientation, packing conditions, and mass fraction of the fibers are significant factors in establishing the thermal conductivity of a polymer composite and are captured in the Nielsen Model, discussed in section 2.2.2 . Due to the nature of these composites, thermal conductivity along the fibers is far greater than in the perpendicular direction and the fiber parameters can vary significantly within the volume of a molded part. It must thus be anticipated that any heat exchanger fabricated of such polymer composites will display thermal anisotropy and spatial variation of the thermal conductivity

The potential impacts of this anisotropy are shown in Figure 19 for a single plate fin, 1mm thick and 5mm tall, on a 3mm wide and 2mm thick base. A constant heat flux is applied at the base, with the fin having an isotropic thermal conductivity of 5 W/mK, and a heat transfer coefficient of 30W/mK is applied to the fin, representing the gas-side behavior of the methane-seawater heat exchanger. Figure 19.a shows the behavior of an isotropic fin; despite the low conductivity, the temperature distribution across the width of the fin is very even and the fin temperature varies from 388K at the base to 376K at the tip. Figure 19.b shows the same conditions, but with a conductivity through the thickness of the fin of 1 W/mK, and a conductivity in the axial direction of 5 W/mK. The temperature distribution now exhibits a more two-dimensional character within both the fin and the base. A temperature variation through the thickness of 1.2K is encountered and, while the temperature at the fin tip is nearly identical to the isotropic case, the more significant base temperature decreases by nearly 1K to 387K.

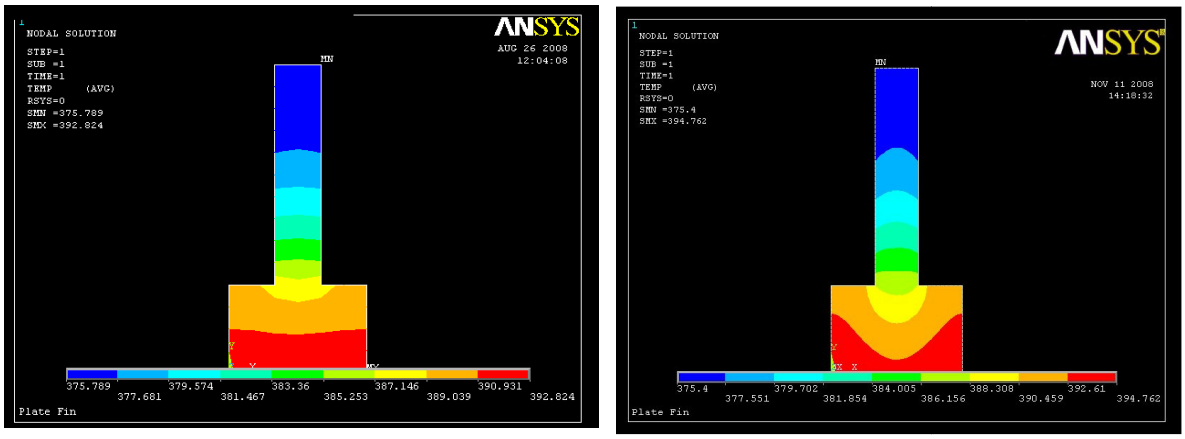

(a) Isotropic Fin, $k_x = k_y = 5$ W/mK (b) Anisotropic Fin, $k_x = 1$ W/mK, $k_y = 5$ W/mK

Figure 19: Temperature distribution in a rectangular plate fin, W=3mm, H=5mm, t_b=2mm,t_f=1mm,h=30 W/m^{2}K, Base heat flux 1000 W/m^2

Low thermal conductivity materials may also have less uniform heat spreading in the base. If there is already a non-uniform temperature distribution at the base of the fin, effects will be amplified throughout the extended heat transfer surface.

In order to further explore these effects, Moldflow simulations of the polymer flow patterns within the prototype fins were studied. Simultaneous research into the molding characteristics of polymers conducted by Cevallos [64] was studied to understand the thermal effects of the molding process. Molding simulations were used of a prototype polymer fin, 5mm in height with a 2.5mm base plate. The software predictions for the statistical probability that fibers will be oriented along a particular axis are shown in Figures 20.a and 20.b. The first figure shows that at the base of the fin, the fibers are highly oriented in the x – or through thickness - direction, with approximately 75% aligned in this direction. However, this orientation weakens in the y-direction with a probability of just 25% near the fin tip and a very low probability of lateral fiber orientation near the side walls of the fin. Conversely, 20.b shows high levels of orientation along the side walls in the y-direction, along the height of the fin. Assuming heat is conducted best along the orientation of the fibers, this is the thermally-preferable case. Figure 20.b shows very low levels of y-orientation at both the base and tip of the fin.

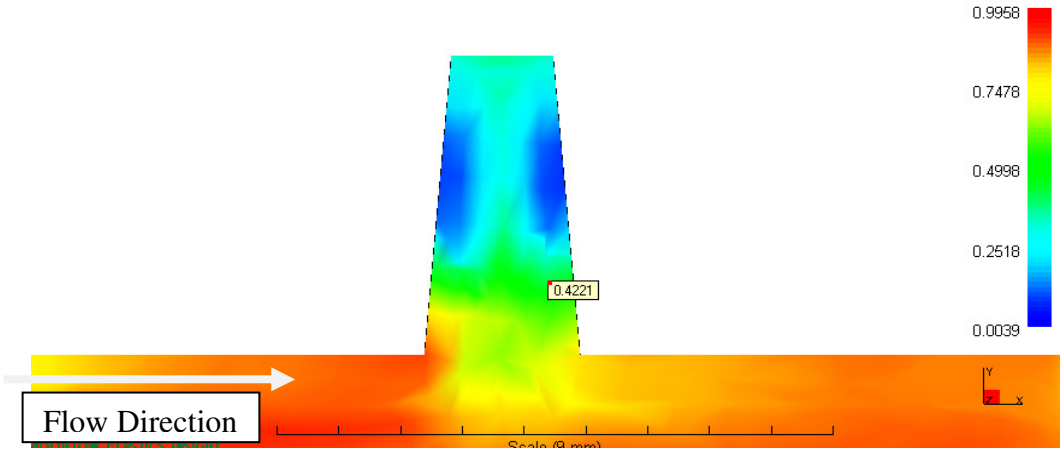

(a) Fiber orientation across the fin thickness (x axis)

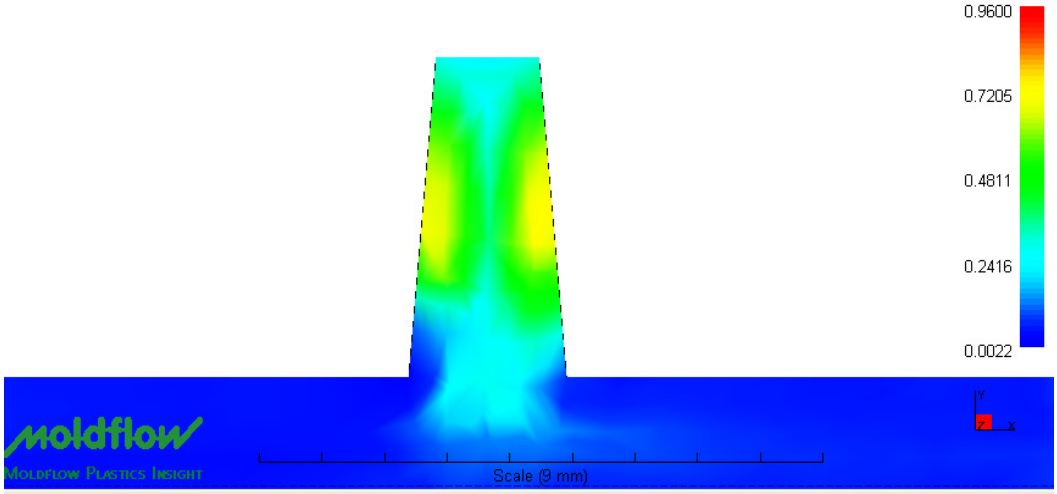

(b) Fiber orientation along the fin height (y axis) t_f=2.5mm, t_b=10mm, H=5mm

Figure 20: Predicted fiber orientation t_f=2.5mm, t_b=10mm, H=5mm [64]

The Nielsen Model, equations (1)-(4), can be used to determine a value for the anisotropic thermal conductivity in the x and y directions, through the Moldflow-generated fiber orientation values. The value of A changes with the fiber orientation. Parameters consistent with the manufacturer's listed thermal conductivity of 10 W/mK [28] and other properties were used, including a filler conductivity of 700 W/mK, polymer conductivity of 0.25 W/mk, fiber volume fraction of 0.33 and maximum packing fraction of 0.52. The resulting maximum composite k, with perfectly aligned fibers, would be 9.5 W/mK with these parameters, and 0.5 W/mK if perfectly "misaligned".

Through this process, an anisotropic conductivity map (Figure 22) was generated for a 5 by 3 grid of distinct thermal conductivity "zones" in the fin, neglecting any z-direction variation in alignment and conductivity. ANSYS simulations were then run to study the thermal performance of this fin, an attempt to determine method to approximate the overall thermally conductivity of the fin in a simpler fashion.

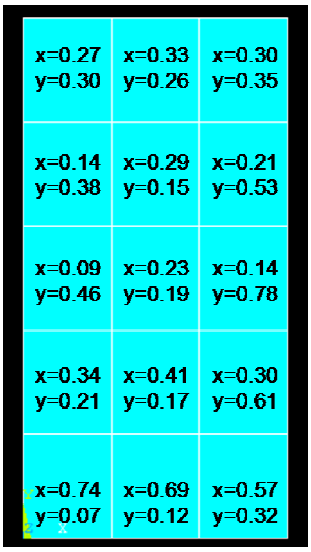

Figure 21: Predicted fiber orientation values along the x & y directions of a fin t_f=2.5mm, H=5mm

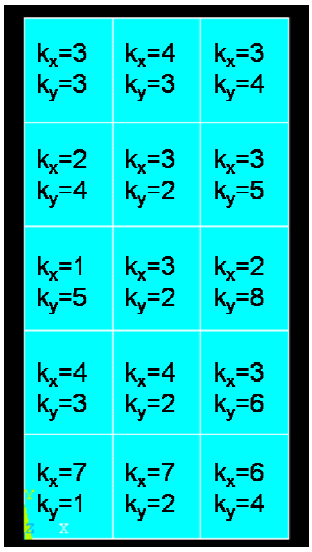

Figure 22:Predicted thermal conductivity values along the x & y directions of a fin t_f=2.5mm, H=5mm

The thermal conductivity values are then used to study the thermal performance of the fin. A constant temperature boundary condition of 353K is applied at the base, and a convective boundary condition is present on the sides and tip of the fin. Results can be seen in Section 7.1.6.

Chapter 5: Parametric Trends in HX for LNG Liquefaction

It is important to understand the relevant heat exchanger design space, and what levels of thermal performance can be expected. The costs of this performance, in pumping power, must be compared, as well as several additional metrics, including the Coefficient of Performance and Total Coefficient of Performance.

5.1 Design Space

The model used for this analysis consists of a homogeneous, doubly finned, 1m by 1m plate enclosed by adiabatic surfaces, representing a single "building block" of a compact heat exchanger (Figure 23). The inlet temperatures of the hot methane gas and cold seawater were taken as 90ºC and 35ºC, respectively. Various plate materials were considered and the geometric parameters, including fin thickness, fin spacing, and the fin height, where varied in the range of 0.1 - 5mm, 2 - 1000mm, and 1 - 20mm respectively. Results are also presented for four sets of fluid velocities.

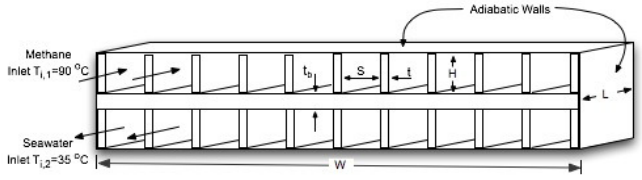

Figure 23: Doubly Finned Parallel Counterflow Heat Exchanger.

5.2 Heat Transfer Rate

The heat transfer rate achieved by a single, $1m^2$, doubly-finned plate, with fin height and thickness of 10mm and 1mm, respectively, is shown in Figure 24 as a function of fin spacing. This exchanger was subjected to a methane velocity of 10 m/s at 90ºC and a cooling seawater velocity of 0.5 m/s at 35ºC. Two inflection points may be observed, for the transition between laminar and turbulent flow regimes for each fluid. The seawater has larger Reynolds numbers, ranging from 1600 to 5200, and results in the smaller

inflection point at a fin spacing of approximately 0.003m. At a fin spacing of 0.005m, the methane transition results in a more dramatic inflection point. Reynolds numbers for the gas range from 1200 to 3900. It may be seen that for these conditions the heat transfer rate varies from approximately 1.5 kW for the unfilled polymer material to approximately 3.7kW for aluminum. However, despite their relatively low thermal conductivities, the polymer composites and titanium are seen to provide substantially higher heat transfer rates than the pure polymer. In particular the low conductivity enhanced thermoplastic appears to achieve more than 80% of the heat transfer of the aluminum module and the high thermal conductivity polymer can reach 90% of this baseline. More importantly, the performance of the two categories of thermally-enhanced polymers brackets the heat transfer rate attained by the titanium alloy, a common material for heat exchangers working in corrosive environments.

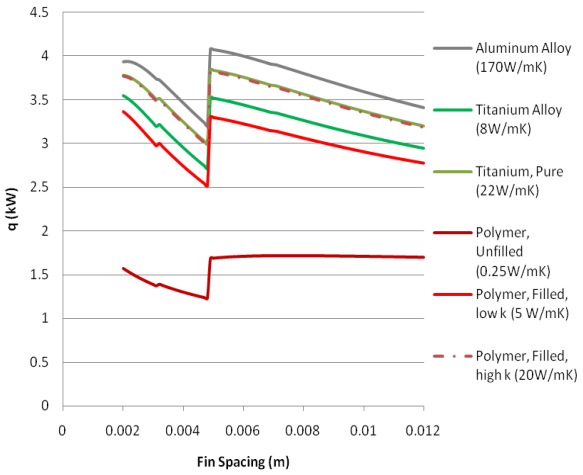

Figure 24: Doubly finned counterflow heat exchanger heat transfer performance as a function of fin spacing and heat exchanger material (t_f =1mm, t_b = 1 mm, H = 10 mm, W = L = 1 m, u_1 = 10 m/s, u_2 = 0.5 m/s).

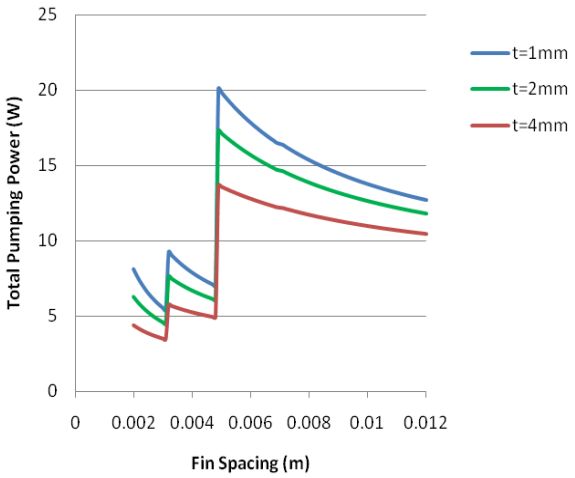

Figure 25: Pumping power for doubly finned counterflow heat exchanger as a function of fin spacing and fin thickness (t_b = 1 mm, H = 10 mm, W = L = 1 m, u_1 = 10 m/s, u_2 = 0.5 m/s).

The relatively modest differences in heat transfer rates among all but the poorest thermal conductivity material (i.e. unfilled polymer) can be traced to the effect of the low gas-side heat transfer coefficient on the overall heat exchanger conductance, as in Equation (23). With methane heat transfer coefficients in the range of 20-40W/m^{2}K, versus typical water

heat transfer coefficients of 1000-2000 W/m^{2}K and plate conductances greater than 5000 W/K for a 1m^2 area of thickness 1-2mm even for thermal conductivities of just 5W/mK, the resistance to heat transfer from the hot methane to the finned plate is the controlling resistance in the heat exchanger. Consequently, the thermal performance of the heat exchanger module is relatively insensitive to the plate thermal conductance and low thermal conductivity materials can be used successfully in the studied application.

5.3 Pumping Power

The pumping power consumed by the finned plate heat exchanger as a function of fin spacing, including both the liquid and the gas sides, is shown in Figure 25 and seen to display three segments of decreasing slope, interrupted by step change increases, for each fin thickness. These step changes are reflective of laminar-to-turbulent flow transitions in the respective channels. Flow in the water channels becomes turbulent at a Reynolds Number of 2300**,** reached with a fin spacing of approximately 0.004m, while the gas flow becomes turbulent at a fin spacing of 0.005m. The pumping power is also seen to decrease with fin thickness, since for the assumed heat exchanger fin spacing and inlet velocity, thicker fins lead to fewer channels and lower total flow rates.

5.4 Coefficient of Performance

The Coefficient of Performance, calculated with equation (34), is plotted in Figure 26 through Figure 29 for varying fluid velocities, as a function of fin spacing and for the various heat exchanger materials considered. For the first case, shown in Figure 26, with the flow conditions (u1=10m/s and u2=0.5m/s) used previously, the plot is seen to display 3 segments of positive slope, interrupted by step changes associated with the previously discussed transitions from laminar to turbulent flow. As expected, the unfilled polymer displays the lowest values of COP – in the range of 0.1 to 0.2kW/W - while the highly conductive polymer is essentially identical in thermal transport efficiency to the pure titanium and superior to the titanium alloy, with COP values peaking at 0.65kW/W in the laminar-laminar range and 0.25 in the turbulent-turbulent range. Interestingly, even

the low conductivity polymer is only marginally lower in COP than the titanium alloy needed for operation in corrosive environments. The foregoing suggests that moderately-filled polymer composites, with thermal conductivities of 5W/mK and better, could be used to replace corrosion-resistant titanium alloys in seawater heat exchangers without a significant loss in thermal performance or heat exchange efficiency.

At lower gas velocities, the COP values for all materials (excluding the unfilled polymer) become much closer, with only a difference of 0.05 (or about 10%) separating the aluminum alloy and the low thermal conductivity polymer. At the increased water velocity shown in Figure 28 and Figure 29, the COP drops dramatically due to the increased pumping power required. In the final COP case, with a gas velocity of 5 m/s and a water velocity of 1 m/s (Figure 29) no flow transition occurs. The gas flow is laminar for the Reynolds numbers from 600 to 1900, and the seawater flow is consistently turbulent for Reynolds numbers ranging from 3100 to 10300.

5.5 Total Coefficient of Performance

While the preceding analyses has demonstrated the near-parity in heat exchange efficiency between filled polymers and a corrosion resistant titanium alloy, the significant differences in the formation and fabrication energy between the polymer composites and both titanium and aluminum alloys suggest that filled polymers may provide a significant advantage in the overall energy efficiency reflected in the sustainability metric, COP_T.

The calculated values for the COP_T, for a service life of one year, shown in Figure 30 for the standard flow velocities of 10 m/s and 0.5 m/s for methane and seawater respectively, reveal that the unfilled polymer, despite its extremely low thermal conductivity, provides the highest value of COP_T, reaching above 100 in both laminar-laminar flow and turbulent-turbulent flow conditions, for the studied range of operating conditions and geometries. This result can be traced to the low manufacturing energy of the polypropylene polymer, which at 24 MJ/kg is less than $1/10^{th}$ of the aluminum and $1/40^{th}$ of either titanium alloy or pure titanium. The filled polymers provide significantly more

heat transfer but also require more fabrication/formation energy – due primarily to the high energy content of the carbon fibers - and display COP_T performance that is substantially below the unfilled polymer but still nearly seven times better than the titanium alloy in turbulent-turbulent flow and 1.5 that of aluminum under the same operating conditions. It is to be noted that both pure and alloyed titanium are severely hindered in their overall energy efficiency by the large manufacturing energy of approximately 1000 MJ/kg.

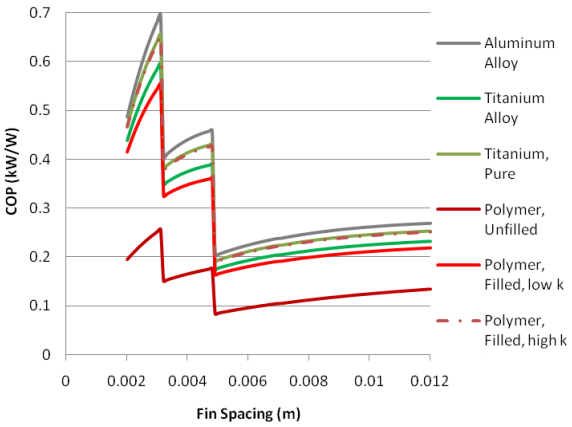

Figure 26: Doubly finned counterflow heat exchanger coefficient of performance as a function of fin spacing and heat exchanger material (t_f =1mm, t_b = 1 mm, H = 10 mm, W = L = 1 m, u_1 = 10 m/s, u_2 = 0.5 m/s).

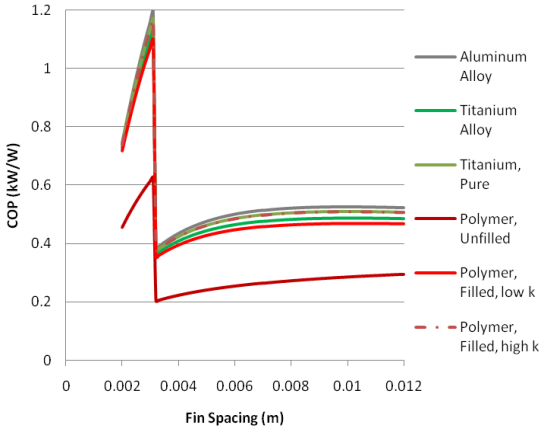

Figure 27: Doubly finned counterflow heat exchanger coefficient of performance as a function of fin spacing and heat exchanger material (t_f =1mm, t_b = 1 mm, H = 10 mm, W = L = 1 m, u_1 = 5 m/s, u_2 = 0.5 m/s).

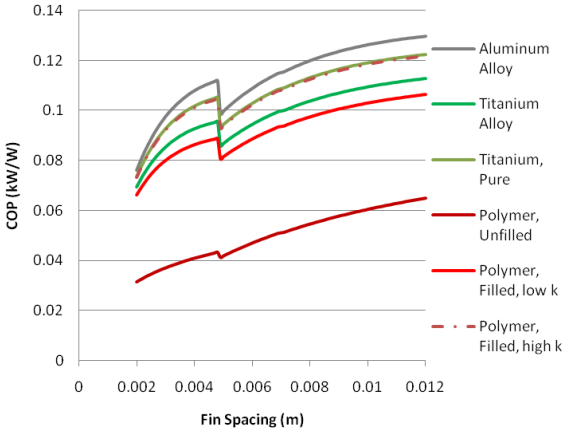

Figure 28: Doubly finned counterflow heat exchanger coefficient of performance as a function of fin spacing and heat exchanger material (t_f =1mm, t_b = 1 mm, H = 10 mm, W = L = 1 m, u_1 = 10 m/s, u_2 = 1 m/s).

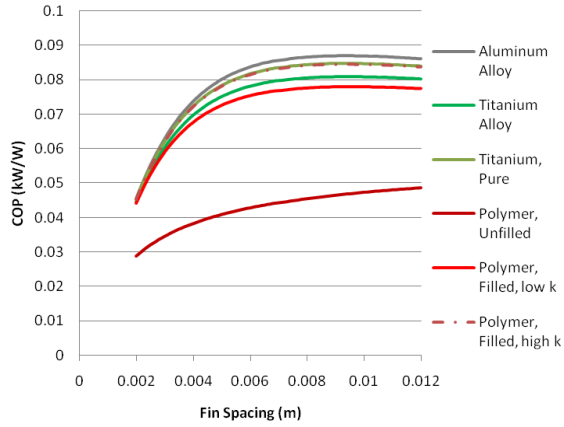

Figure 29: Doubly finned counterflow heat exchanger coefficient of performance as a function of fin spacing and heat exchanger material (t_f =1mm, t_b = 1 mm, H = 10 mm, W = L = 1 m, u_1 = 5 m/s, u_2 = 1 m/s).

Figure 31, with a reduced methane velocity of 5 m/s, shows an even more dramatic difference between the unfilled polymer and the other materials under analysis. Because of the lower pumping power in this case, manufacturing energy plays a larger role, and thus the COP_T values decrease. The filled polymers continue to perform the best of the potential heat exchanger materials, nearly double that of aluminum, and many times that of titanium. In Figure 32, with the highest gas and water velocities under analysis, the heat exchanger COP_T has less dependence on formation/fabrication energy. The thermally enhanced polymers show comparable performance to the unfilled polymer throughout the fin spacing domain, and far superior to the other materials. The low fluid velocities in Figure 33 result in significantly lower heat transfer and a corresponding drop in the COP_T. It is important to note that the COP_T values for this case are approximately one third of the values in the standard case shown in Figure 30. This is a much smaller difference than the corresponding difference in the COP metric (approximately one eighth).

To further clarify the trends seen in the COP_T metric it is instructive to examine Figure 34 that displays the manufacturing fraction of the overall energy consumed by the finned plate heat exchanger module, at a fin spacing of 0.005m when both fluids are turbulent and for a service life of 1 year. Examining the manufacturing fractions – which range from just 0.20 for unfilled polymer to 0.95 for the titanium alloy - it is clear that a lower fraction of invested energy correlates directly with a large COP_T. This trend is magnified by the short service life of today's seawater heat exchangers which makes it imperative that heat exchanger design and material selection include consideration of the invested manufacturing energy.

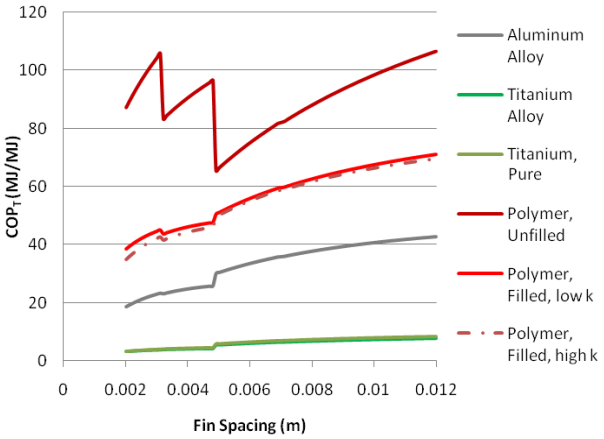

Figure 30: Doubly finned counterflow heat exchanger total coefficient of performance as a function of fin spacing and heat exchanger material (t_f=1mm, t_b = 1 mm, H = 10 mm, W=L= 1m, u_1 = 10 m/s, u_2 = 0.5 m/s).

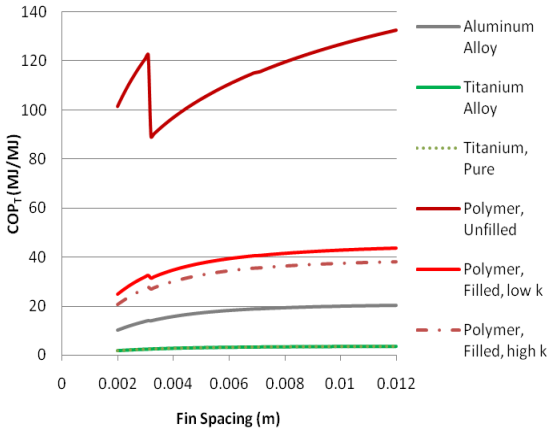

Figure 31: Doubly finned counterflow heat exchanger total coefficient of performance as a function of fin spacing and heat exchanger material (t_f =1mm, t_b = 1 mm, H = 10 mm, W = L = 1 m, u_1 = 5 m/s, u_2 = 0.5 m/s).

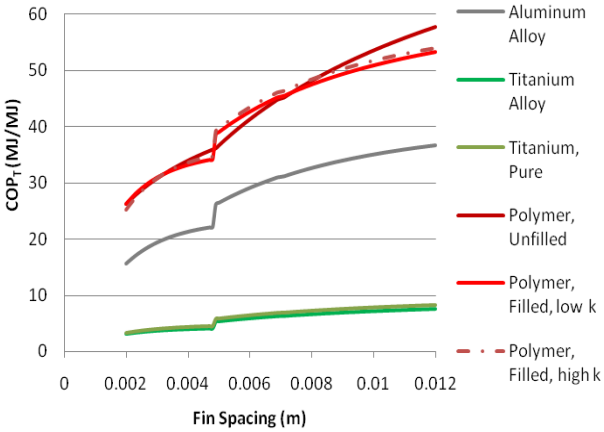

Figure 32: Doubly finned counterflow heat exchanger total coefficient of performance as a function of fin spacing and heat exchanger material (t_f=1mm, t_b = 1 mm, H = 10 mm, W=L= 1 m, u_1 = 10 m/s, u_2 = 1 m/s).

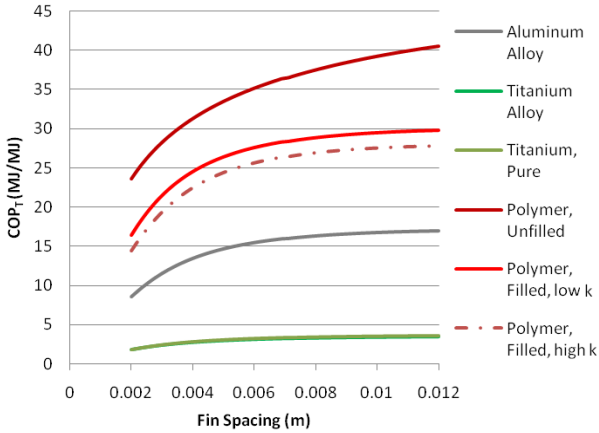

Figure 33: Doubly finned counterflow heat exchanger total coefficient of performance as a function of fin spacing and heat exchanger material (t_f=1mm, t_b = 1 mm, H = 10 mm, W = L = 1 m, u_1 = 5 m/s, u_2 = 1 m/s).

It is important to note that even with a much higher fabrication energy, but a far better thermal conductivity, the filled polymers have a COP_T roughly 82% of the unfilled polymers, while aluminum is only 47% of the unfilled polymer (for the case shown in Figure 30). Thus, when a heat transfer efficiency requirement has to be met, a filled polymer appears to be superior to aluminum.

Since, as previously noted, the poor thermal properties of methane make it possible for heat exchangers fabricated of low thermal conductivity materials to achieve adequate

heat transfer, the heat transfer rate for the low thermal conductivity polymer is found to equal 90% of the value achieved by the highly conductive polymer. Consequently, when the lower manufacturing energy of the low conductivity polymer, due to the reduced carbon fiber concentration, is considered, the low conductivity filled polymer has a nearly identical COP_T to the highly conductive polymer.

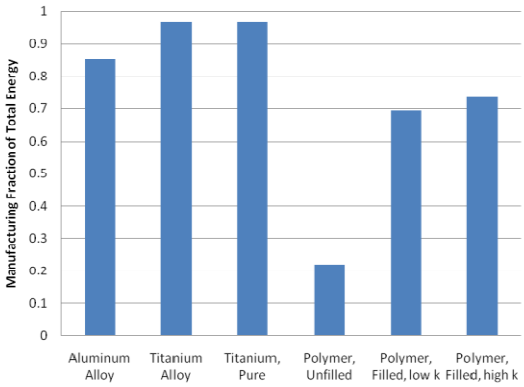

Figure 34: Energy invested in doubly finned counterflow heat exchanger as a function heat exchanger material (t_f =1mm , t_b = 1 mm, H = 10 mm, W = L = 1 m, S = 5 mm, u_1 = 10 m/s, u_2 = 0.5 m/s).

5.6 Geometric Optimization

As each of the materials considered for the finned plate heat exchanger has different thermal properties and energy contents, a detailed thermal transport and energy efficiency comparison should be based on the optimized designs for each material.

Figure 35 displays the variation of the Total Coefficient of Performance with fin height for each of the subject materials for the indicated flow and geometric parameters. The fin height is assumed to be equivalent on both sides of the heat exchanger. For the lowest thermal conductivity material – the unfilled polymer – there is a sharp optimum at approximately 3mm. While the other studied materials display optimum fin heights that increase – as expected – with the thermal conductivity, the height variation of COP_T is modest and fin heights of approximately 10mm – as previously assumed – can be expected to yield close to the best results.

Figure 36 shows the variation of COP_T with the fin spacing, when the fin height for each material is set at the optimum value displayed in Figure 35. Because a large fin spacing for the assumed plate width of 1m leads to a small number of fins, increasing fin spacing reduces the mass of the finned plate heat exchanger module and reduces the required manufacturing energy investment but also reduces the surface area exposed to the working fluids. It is thus seen that for the materials with low or modest formation/fabrication energies, a clear peak appears at values that range from 73mm for the unfilled polymer to 93mm for the highly-conductive polymer and to just 42mm for aluminum. However, the COP_T for pure titanium (k=22 W/mK) didn't reach a peak until 0.87m, and the titanium alloy (k=8 W/mK) never reached a COP_T peak.
In addition to optimizing the fin spacing and fin height, determination of the most energy efficient configuration for each material requires selection of the optimum fin thickness. Along with the material properties and the height, the optimal fin thickness can be expected to depend on the heat transfer coefficient on the exposed fin surface, which varies substantially from the gas-side to the liquid-side of the heat exchanger module. It is, thus, necessary to determine the optimal gas-side and liquid-side fin thicknesses, respectively.

Figure 37 and Figure 38 display the calculated variation of the COP_T with fin thickness on the liquid and air sides, respectively. While the COP_T for the unfilled polymer and the pure titanium show near-independence of the liquid-side thickness, it appears that optimum thickness for fins of filled polymers and aluminum is approximately 0.5mm and 0.3mm, respectively. Similar conclusions can be drawn relative to the air-side fin thickness, although the optimal values for the filled polymers and aluminum are somewhat larger than on the liquid side of this methane-water heat exchanger. Due to the relatively low heat transfer coefficients associated with the flow of methane in the prescribed passages, typically in the range of 20-40 W/m^2K, versus the 1500-2500 W/m^2K heat transfer coefficients expected on the seawater side, the addition of fins on the gas side generally has a greater impact on the overall module heat transfer rate.

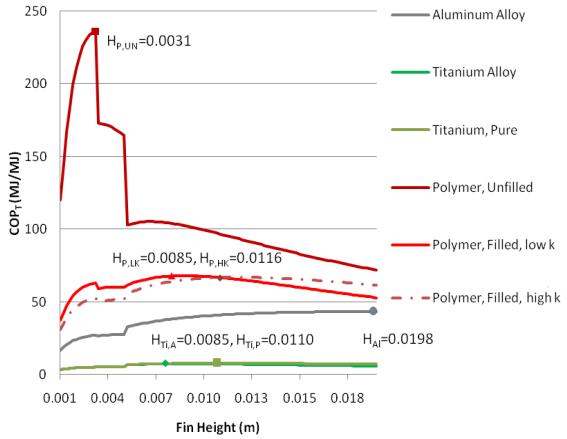

Figure 35: Doubly finned counterflow heat exchanger total coefficient of performance as a function of fin height and heat exchanger material (t_f = 1mm, t_b = 1 mm, W = L = 1 m, S= 10 mm, u_1 = = 10 m/s, u_2 = 0.5 m/s).

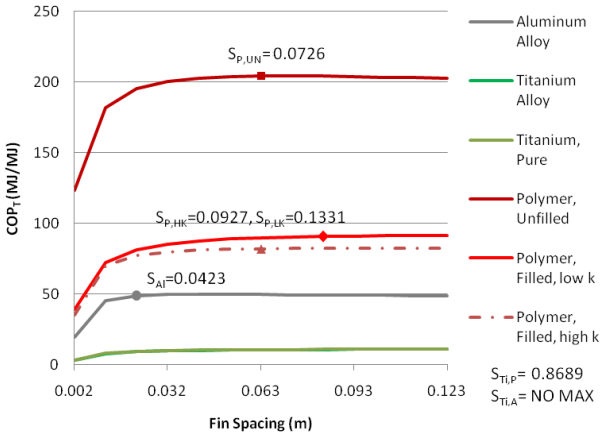

Figure 36: Doubly finned counterflow heat exchanger total coefficient of performance as a function of fin spacing and heat exchanger material (t_f =1mm, t_b = 1 mm, W = L = 1 m, u_1 = = 10 m/s, u_2 = 0.5 m/s, H = optimal height shown in Figure 35).

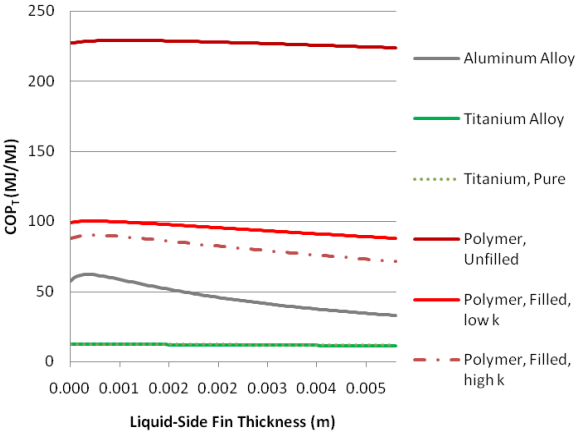

Figure 37: Doubly finned counterflow heat exchanger total coefficient of performance as a function of liquid-side fin thickness and heat exchanger material (t_b = 1 mm, optimum height, optimum fin spacing, W = L = 1 m, u_1 = 10 m/s, u_2 = 0.5 m/s).

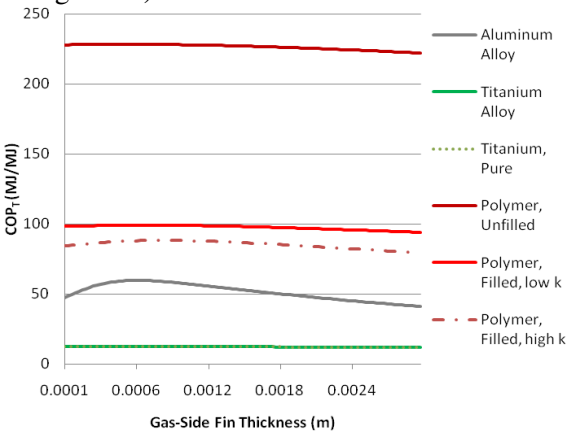

Figure 38: Doubly finned counterflow heat exchanger total coefficient of performance as a function of gas-side fin thickness and heat exchanger material (t_b = 1 mm, optimum height, optimum fin spacing, W = L = 1 m, u_1 = 10 m/s, u_2 = 0.5 m/s).

The overall optimum system dimensions, determined in Figure 35 through Figure 38, are shown in Table 9. The resulting COP_T values are plotted in Figure 39 and seen to span a range from 12.5 for the titanium alloy to 228 for the unfilled polymer. Interestingly, this first-order optimization has succeeded in yielding optimized COP_T values for the filled polymers that are 26% to 40% higher than the peak value of 70 achieved with the

nominal geometry analyzed in Figure 24 for both the low- and high-conductive polymer composites.

Material	k (W/mK)	H (mm)	S (mm)	Liquid thickness (mm)	Gas thickness (mm)
Aluminum Alloy	170	19.8	42.3	0.347	0.646
Titanium Alloy	8	8.5	No Maximum	0.248	0.050
Titanium, Pure	22	11	869	0.248	0.288
Polymer, Unfilled	0.25	3.1	72.6	0.941	0.892
Polymer, Filled, low k	5	8.5	133	0.397	0.765
Polymer, Filled, high k	20	11.6	92.7	0.446	1.486

Table 9: Best Performing Parameters for Gas/Liquid Counterflow Heat Exchanger.

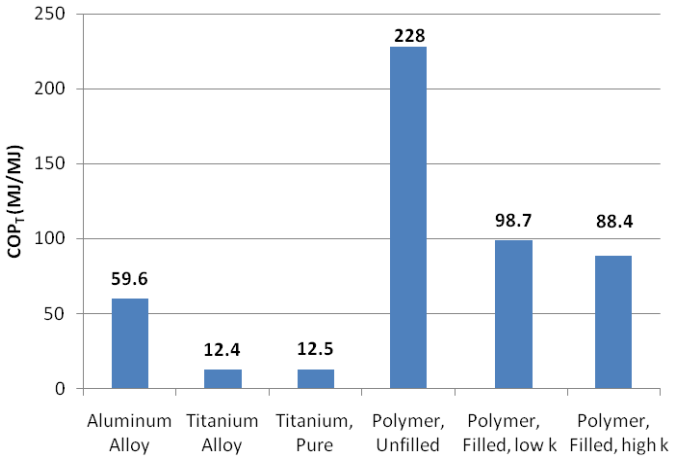

Figure 39: Material-optimized COP_T for doubly finned counterflow heat exchanger (tb = 1 mm, optimum height, optimum fin spacing, optimum fin thickness, W = L = 1 m, u1 = 10 m/s, u2 = 0.5 m/s)

Examining the optimum dimensions for the lower conductivity (k=5W/mK) material, it is seen that the 40% increase in the COP_T value to nearly 100 was achieved largely by reducing the mass of the fins through use of thinner fins of reduced height and larger spacing than used in the nominal design. The more modest increase in COP_T to 88 for the high conductivity polymer was achieved largely through thermally "fine tuning" the design, so that judicious addition of mass – through taller and more closely-spaced fins -

resulted in greater increase in the heat transfer rate than in the formation and fabrication energy. It is also important to note the similar energy efficiency of the low and high thermal conductivity polymers. The high k polymer has a slightly higher heat transfer rate, but the added energy content of the additional carbon fiber mass leads to a COP_T value that is only 90% of the low k polymer's value

Alternatively, the heavy burden of the very large manufacturing energy of the titanium and titanium alloy, at nearly 1000MJ/kg, suppressed any benefit provided by this first-order optimization processes and left the COP_T values essentially unaltered from the nominal conditions of Figure 24.

While the unfilled polymer results in a large COP_T, when a minimum heat transfer rate criteria is applied, the filled polymers are the leading material, with COP_T values 1.6 times that of aluminum and roughly 8 times greater than titanium.

5.7 Optimizing COP_T with Least Material Relations

The least material relations used in Section 3.2 for fins and finned arrays can be used to optimize the COP_T more rigorously. In Figure 40, the Total Coefficient of Performance (COP_T) is plotted for the same case as Figure 15, for a finned array with 500 fins and a heat transfer coefficient of 30 W/m^2K. The errors between the predicted least material thickness and actual are seen to increase at lower conductivities, with an error of 1.7% at k=300 W/mK, 1% at k=40, 20, and 10 W/mK, 6.2% at k=10 W/mK, 13.9% at k=5 W/mK, and 87.0% at k=0.25 W/mK. This increased error is likely due to that fact that for the k=0.25 W/mK case, the heat transfer per unit length varies from roughly 2.6 W/m to 4.4 W/m, over a range of fin thicknesses from 0.1mm to 2mm, at the least material condition of 1.97mm the fin spacing is very small (0.0287mm), and pumping power is very large. Because of this the pumping power, not the mass, dominates the COP_T.

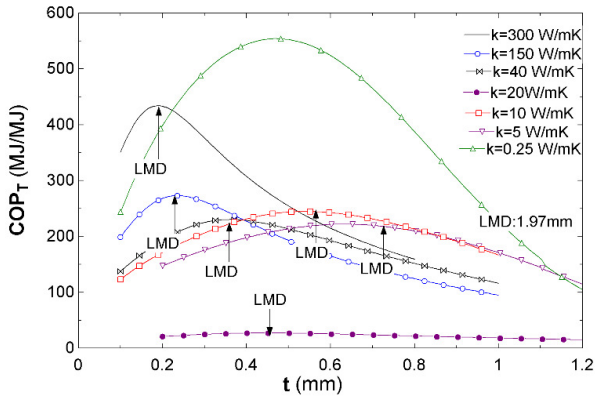

Figure 40: Total coefficient of performance in a gas-cooled array, for various thermal conductivities. W=1M,A_p=8 mm^2, h=30 W/m^{2}K, θ_b =55K, N_{fins}=500, t_b=1mm

It is important to note that while the COP_T values peak in Figure 40 at different thicknesses for k=150,40,10, & 5 W/mK, the value of the COP_T itself is nearly identical for all 4 cases.

Similarly to the previous case, if can set the gas velocity constant as opposed to the heat transfer coefficient (Figure 41). This is a less general case, and more practical for industry. The least material relation accurately predicts the peak within 0.5% for k=300 W/mK, 2.4% for k=150 W/mK, 4.3% for k=40 W/mK, 5.3% for k=20 W/mK, 7.0% for k=10 W/mK, and 9.4% for k=5 W/mK. While the 0.25 W/mK case does not peak in this example, by extending the array width to 2m, holding everything else constant, the least material efficiency accurately predicts the peak heat transfer rate of 6.9 kW/m within 6.9%. For the k=0.25 W/mK case, 55-75% of the heat transfer was through the fins. The percent through the fins increases with increases fin thickness, as the interfin spacings decrease with this quantity.

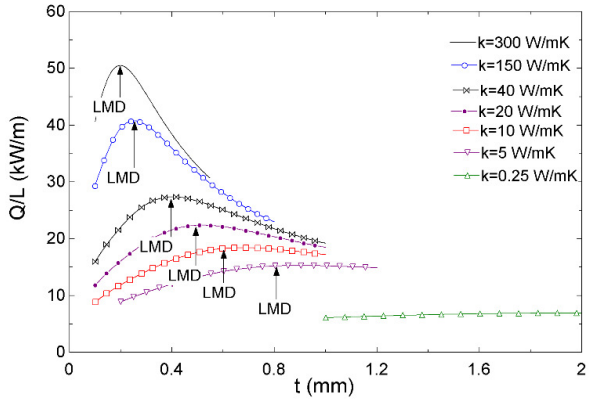

Figure 41:Heat transfer per unit length in a gas-cooled array, for various thermal conductivities. W=1m, A_p=8 mm^2, v=10 m/s, θ_b =55K, N_{fins}=500

Notably, the previous two examples used relatively large numbers of fins, and thus small interfin spacings. When fewer fins are used, additional measures must be taken to find the least-material point. This motivates the use of a value for fin heat transfer per unit length, as opposed to total heat transfer, including the fin and base. While neglecting the interfin spacings is poor overall design practice, this could be used to more accurately fine the least material fin. Figure 42, the predicted least material thickness aligns much more accurately with the peak of the fin heat transfer per unit fin mass plot. The error at k=300,150, and 40 W/mK are reduced to 3.0%, 2.9%, and 3.7%, respectively. More important, for low thermal conductivity fins, the error was reduced to 3.5%, 3.0%, 2.0%, and 10.8% for k=20, 10, 5, and 0.25 W/mK. While this is an insufficient metric for overall fin array performance, it provides a good basis for evaluation of the number of fins and their aspect ratio on a given array surface. By subtracting the mass of the walls from the total allowed mass, this method could be used to accurately maximize the achievable heat transfer, through the use of optimum fins.

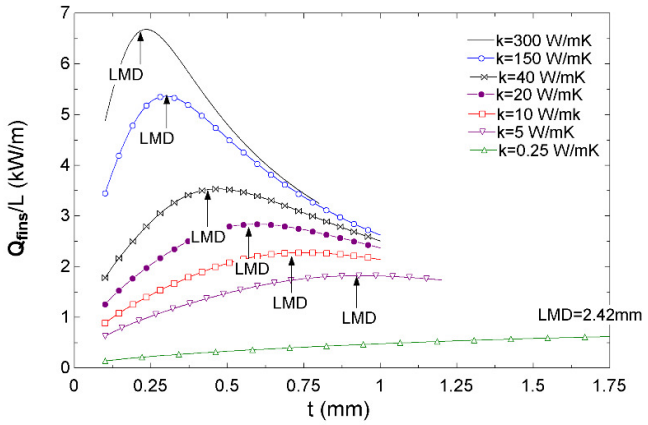

Figure 42: Fin heat transfer per unit length in a gas-cooled array, for various thermal conductivities. W=1M, A_p=8 mm^2, v=10 m/s, θ_b =55K, N_{fins}=50

Another method to improve the accuracy of the least material correlation, without neglecting the important heat transfer through the base, is through the use of the least array-based optimum fin, as given in equation (18). The optimum fin efficiency is no longer 0.627, but varies with the heat transfer coefficient, fin height, and thermal conductivity. The second term in this equation accounts for heat transfer from the interfin spacings. Because the optimum efficiency varies across the range of fin thicknesses plotted here, the least-material point is defined as that where the actual fin efficiency matches the optimum efficiency and the accuracy is the difference between this point and the point of maximum heat transfer.

The same conditions were studied as Figure 42. The heat transfer rate per unit length is identical, but the array based optimum fin changed, as shown in Table 10 . Errors remained under 10% for thermal conductivities of 300 W/mK down to 5 W/mK.

k (W/mK)	*η (peak)*	*η (optimum)*	*Error*
300	0.6548	0.6247	4.82%
150	0.6607	0.6235	5.97%
40	0.664	0.619	7.27%
20	0.666	0.613	8.65%
10	0.636	0.6053	5.07%
5	0.6	0.591	1.52%
0.25	0.2011	0.2853	-29.51%

Table 10: Error in array-based optimum fin equation

An additional factor to consider is that, with a constant profile area, each fin height will have its own unique optimum point. In such a case (shown in Figure 42), the optimum fin efficiency for a 0.25 W/mK fin varied from 5% to 39% as fin thickness varied from 0.1mm to 2.5mm. By holding the height constant at 1cm and the heat transfer coefficient at h=50 W/m^2K , this variation is reduced to 27.1% to 25.3% over the same range, only due to the change in base area, which varies from 0.995 m^2 to 0.875m^2. With each fin having a nearly identical optimum point, the array-based optimum fin equation more accurately predicts the peak. In this case, the optimum efficiency was predicted as 25.1% for an actual efficiency at peak heat transfer rate of 24.1%, an error of only 4%.

As indicated by Bar-Cohen and Jelinek [54], optimization of a rectangular plate fin array by assuming the array is composed of a series of individually optimum fins seems to work well for a range of thermal conductivities, from 5 W/mk to 300 W/mK. At a very low thermal conductivity of 0.25 W/mK, typical of unfilled polymers, a corrected array-based optimum fin efficiency is necessary, as well as use of the more thorough fin efficiency equation, for a fin with a convecting tip.

5.8 Alternative Heat Exchanger Designs

Beyond the finned plate heat exchanger studied so far, there are several alternative heat exchanger configurations that may be considered. Here, the finned plate heat exchanger will be compared to a more conventional shell and tube heat exchanger, as well as another compact heat exchanger configuration, referred to as a plate coil. The three geometries will be compared for a constant heat transfer rate, constant flowrate scenario, comparable to the design decisions which must be made when commercially developing a heat exchanger for a specific application. In this case, a 350kW heat exchanger will be designed, with flowrates of 10,000 kg/hr of methane at 90℃ and 300,000 kg/hr of seawater at 35℃, representative of a production scale heat exchanger for natural gas liquefaction [9].

5.8.1 Configurations

A finned plate heat exchanger, similar to that shown in Figure 23, will be studied here. In order to achieve the required heat transfer of 350 kW, a 1m wide by 1m long heat exchanger is used, with 100 fins on the gas side and 5 fins on the water side, each 1mm thick, with a 2.5mm base thickness, needed to assure effective injection molding of the thermally enhanced polymer composite will be used [65]. This results in a 17.8 m/s gas velocity and a 0.30 m/s water velocity when used with the previously specified flow rates.

Shell and tube heat exchangers have been used for some time in industrial applications, where high operating pressures are encountered. Without the need for gaskets, as used in plate heat exchangers, they are quite strong and reliable. A shell and tube heat exchanger consists of a bundle of tubes within a large shell, as shown in Figure 43. For gas-liquid applications, the liquid would be on the inside of the tubes, and the gas would flow around and on the outside of the tubes. The tubes may be enhanced with fins to improve their thermal performance. Baffle plates, or tube sheets, are used at several points along the length of the shell to support the tubes and force the gas to travel across the tubes, not along their length. For purposes of this study, a similar shell and tube configuration, which might be used in a natural gas liquefaction facility, is chosen. A 6m long shell, 1.5m in diameter is used, filled with 2000 finned tubes, each with a 14mm inner diameter. A tube wall thickness of 1.5mm is required for sufficient strength. The resulting fluid velocities are 29.5 m/s on the gas side and 0.27 m/s on the water side.

The plate-coil configuration (Figure 44) is another potential compact heat exchanger geometry [66, 67]. It consists of a stack of rifled plates, containing an axial array of "embedded" tubes. When fabricated of conventional heat exchanger metals, relatively thin walls , small diameter passages, and very small vertical and horizontal spacings between the tubes could be used. For a molded polymer composite heat exchanger module, a tube inner diameter of 2mm and a 2mm thick wall is thought to be necessary. In order to achieve 350kW of heat transfer, 190 plates, with 30 tubes in each plate are

required. This results in fluid velocities of 0.75 m/s on the gas side, and 4.75 m/s on the water side.

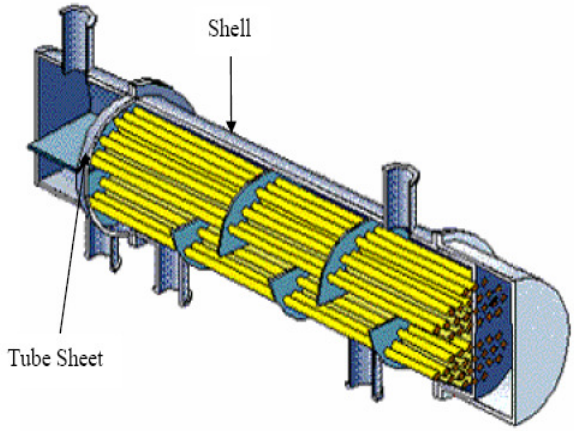

Figure 43: A shell and tube heat exchanger [68]

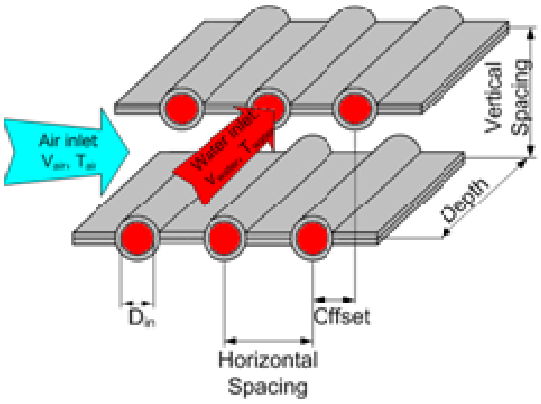

Figure 44: Proposed plate-coil heat exchanger [66]

5.8.2 Results of comparisons

The Coefficient of Performance (COP), volumetric heat transfer rate, and mass-specific heat transfer rate, as previously defined, were chosen to provide a basis for comparison of these three configurations, operating at constant flowrates and heat transfer rates. The Coefficient of Performance, as shown in Figure 45, shows a value of about 16 for the shell and tube, 25 for the plate coil, and 62 for the finned plate. Because flowrates and heat transfer rates are held constant across each design, the key differentiating factor here is the pressure drop. The finned plate heat exchanger, due to its open, unobstructed channels, has very low pressure drops of about 0.01 bar and 0.004 bar on the gas and water side, respectively. The plate coil heat exchanger, as one might expect, has an extremely small gas side pressure drop of 9×10^{-5} bar, but a high water side pressure drop of 1.6 bar due to the small tube diameter. Notably, if a larger tube diameter was used for the plate coil configuration, the COP would go up by a factor of four, but the other

metrics discussed later would suffer significantly. The shell and tube has values of 0.05 and 0.03 bar on the gas and water side.

A similar trend can be seen when observing the volumetric heat transfer rate (Figure 46). The shell and tube is the lowest, at about 30 kw/m^3. The finned plate and plate coil, both considered compact heat exchanger geometries, are significantly better; the plate coil at 100 kW/m^3 and the finned plate at 230 kW/m^3. The finned plate is superior in this metric due to its ease of manufacturing with injection molding. A thick base plate is all that is required to facilitate removal of a molded heat exchanger module from the mold. The plate coil configuration, on the other hand, operates best at thicknesses of under 0.5mm, at which point it would have a very large volumetric heat transfer rate. But tubes this thin would not be structurally stable, and would break when removed from a mold. The 2mm thick walls, combined with the 2mm diameter tubes, significantly hamper the volumetric performance.

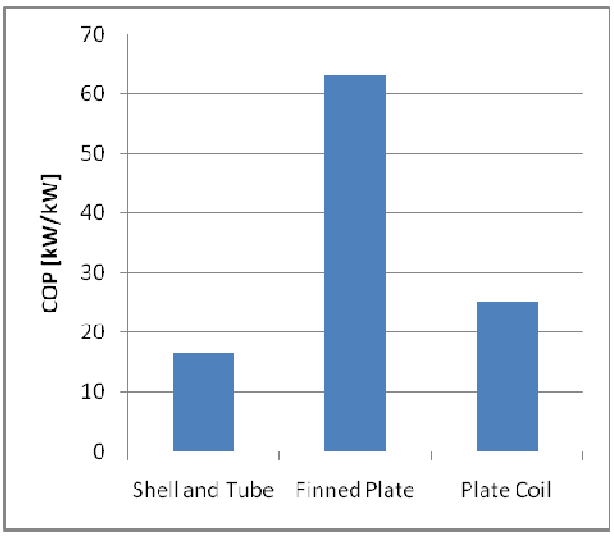

Figure 45: Coefficient of performance of alternative heat exchanger configurations [68]

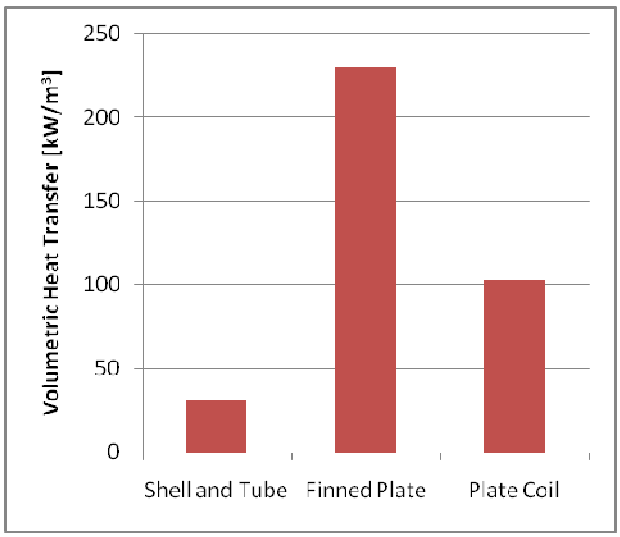

Figure 46: Volumetric heat transfer of alternative heat exchanger configurations

Finally, the mass based performance is studied. This is an important metric, because not only does the mass of the heat exchanger influence metrics such as the Total Coefficient of Performance, but it also plays a major role in the manufacturing and transportation

costs. Simply moving a heavy heat exchanger from the place where it was built to the location of use can consume large quantities of fuel.

Figure 47 shows this mass specific heat transfer rate, in kW/kg of material. A density of 1.7 g/cm^3 is used, representative of a 10 W/mK thermally enhanced polymer composite. Once again, the shell-and-tube performs poorly, at slightly above 0.1 kW/kg. The plate coil is nearly double that, at 0.2 kW/kg, and the finned plate is well beyond this value, at 0.55 kW/kg. In determining this mass-specific heat transfer rate for the shell-and-tube configuration, only the mass of the tubes, the active heat transfer surface, was considered. The shell could be built from any other material deemed appropriate, but inclusion of this material would further lower the already poor mass-specific heat transfer rate. The two compact heat exchanger geometries will also require some sort of supporting structure, but it is not likely to be as large and massive as what is required for a shell-andtube heat exchanger.

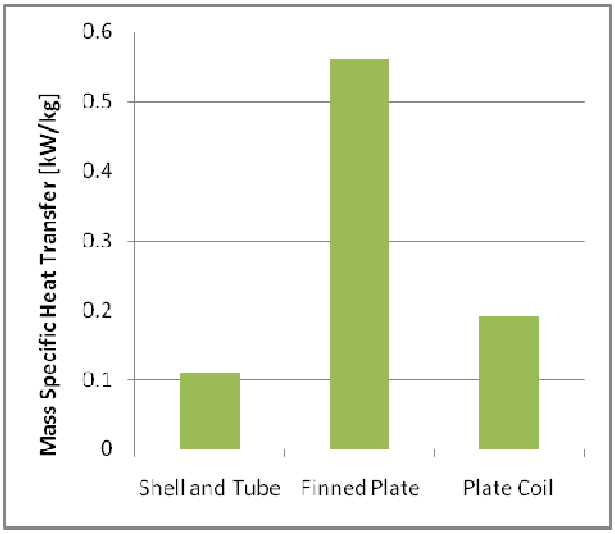

Figure 47: Mass specific heat transfer rates of alternative heat exchanger geometries

The finned plate geometry showed superior performance compared to manufacturable shell and tube and plate coil configurations. The performance of the plate coil was severely limited due to constraints imposed by the injection molding process. Mass and volume specific metrics for the finned plate were seen to be nearly 5 times greater than a shell and tube configuration, due to the large enclosed volume and required heat transfer area for a shell and tube. A plate-coil may be a promising next generation heat exchanger geometry for different materials, but a polymer finned-plate heat exchanger shows the greatest promise out of the three studied here.

Chapter 6: Optimization of Low-k Heat Exchangers

This Chapter focuses on attaining the minimum mass design to achieve the optimum heat transfer rates for a range of pumping powers. The array-based least material relation, Eq. (18), is used to minimize the fin mass required for a complete heat exchanger module (Figure 23). Several metrics, including the heat transfer rate, the mass-specific heat transfer rate, and the total Coefficient of Performance (COP_T), are used to compare the thermal performance of polymer composites having a range of thermal conductivities with that of corrosion resistant metals. The operating conditions considered are typical of the natural gas liquefaction industry in the Persian Gulf, namely hot gas at 90°C cooled by 35°C seawater. In addition, the gas flow rate is varied from 0.01 to 0.1 m^3/s, while the coolant velocity is held constant at 1m/s. For the design and operating conditions examined, a 10 W/m-K polymer composite is found to provide nearly identical heat transfer rate to that of a corrosion-resistant titanium heat exchanger. Furthermore, at 200 W pumping power, the polymer composite provides 3.2 kW/kg of mass-specific thermal performance, which is almost 50% higher than for titanium. Polymer composites also show COP_T values approximately twice that of a least-material titanium heat exchanger. The results contribute to establishing the viability of using polymer composites for gas-liquid heat exchanger applications involving seawater and other corrosive fluids.

6.1 Motivation for gas-side optimization

Applying Eq. (23) to the determination of the effective thermal conductance for the heat exchanger module, it can be seen from Figure 48 that in the case of the low thermal conductivity unfilled polymer (k=0.25W/mK), roughly two thirds of the thermal resistance occurs on the gas side, and the bulk of the remaining third is from the wall. For a 10 W/mK polymer composite (Figure 49), roughly 90% of the thermal resistance is due to the gas side. Since the convective resistance on the seawater side is nearly an order of magnitude below the gas side resistance, least-mass optimization of this seawater heat exchanger begins by nearly eliminating the fins on the water side, leaving widely-spaced

fins to primarily meet the structural constraints of this finned-plate compact heat exchanger. Since the overall thermal resistance is dominated by the convective resistance on the gas side, it is these fins that need to be optimized for the highest heat transfer rate per unit mass. For purposes of the present study, the base plate thickness is assumed to be dictated by molding considerations and is taken to be constant and equal to 1mm. Such a thin base plate would be difficult to manufacture using today's techniques, but would most effectively take advantage of the material. Multi-gate molding and significant fin tapers would surely be required to mold such a heat exchanger.

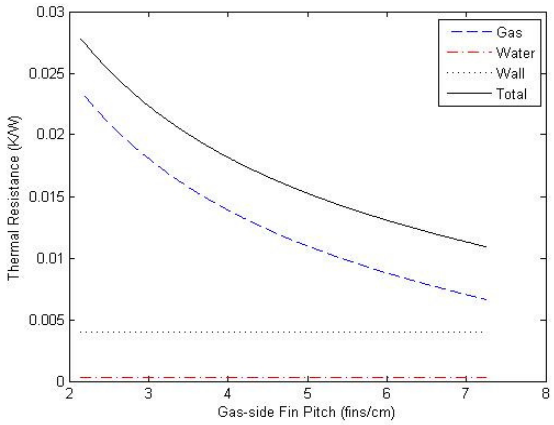

Figure 48: Thermal resistance values as a function of fin pitch, k=0.25 W/mK, W=L=1m, H_{fin}=10mm, t_f=t_b=1mm. Liquid velocity: 1 m/s, Gas Flowrate: 0.073 m^3/s, $N_{fins,liquid}$=25, t_b=t_f=1mm, k=10 W/mK

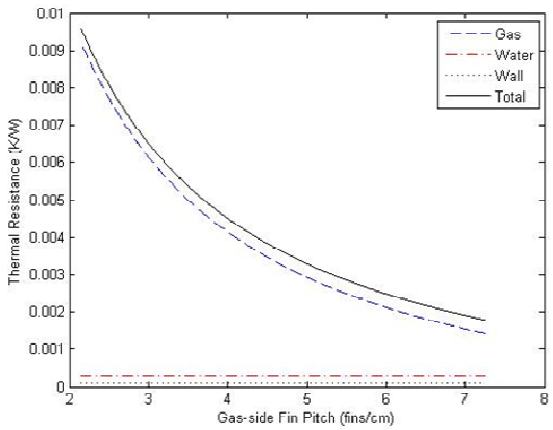

Figure 49: Thermal resistance values as a function of fin pitch, k=10 W/mK, W=L=1m, H_{fin}=10mm, t_f=t_b=1mm. Liquid velocity: 1 m/s, Gas Flowrate: 0.073 m^3/s, $N_{fins,liquid}$=25, t_b=t_f=1mm, k=10 W/mK

6.2 Results and Parameter Trends

In this section, the results of parametric analyses for metallic and polymer composite materials are presented and discussed in terms of the heat transfer rate, Coefficients of Performance, mass-specific heat transfer rate, and least-material fins.

6.3 Heat Transfer Rate for HX Module

Prior to exploring the impact of least-mass optimization, it is useful to determine the baseline performance of a polymer, as well as various metallic, methane-seawater heat exchangers operating in the parametric space appropriate to a natural gas liquefaction plant in the waters of the Persian Gulf.

Examining Figure 50 it may be observed that – for a counterflow parallel-plate heat exchanger with a fin height of 10mm and fin thickness of 1mm operating with a liquid velocity of 1m/s and gas flow rate that varies from 0.008 to 0.12 m^3/s - the heat transfer rate is relatively insensitive to the thermal conductivity of the heat exchanger material, down to approximately 5W/mK. Thus, for example at a pumping power of 200W, a carbon-filled polymer composite having a thermal conductivity of 5 W/mK yields a heat transfer rate of 5.5kW or some 85% of what could be achieved with a $1m^2$ copper heat exchanger (k= 300 W/mK). Similarly, a polymer composite or other material with thermal conductivity of 10 W/mK provides 92% the thermal performance of copper, while titanium, at 20 W/mK, would provide 95% of this maximum performance. Overall, the heat transfer rate can be seen to increase with increasing pumping power, with diminishing improvements at higher pumping powers.

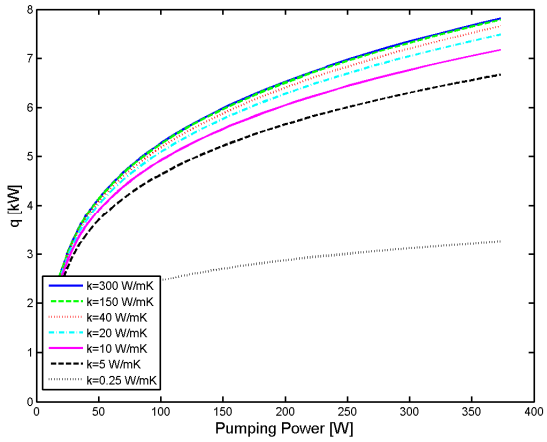

Figure 50: Gas/Liquid thermal performance in a counterflow parallel plate heat exchanger. W=L=1m, H_{fin}=10mm, t_f=t_b=1mm. Liquid velocity: 1 m/s, $N_{fins,m}$=100, $N_{fins,w}$=5

Increasing the number of fins on the methane side from 100 to 200 would help to increase the heat transfer rate at lower pumping powers and, thus, flatten the shape of the curves shown in Figure 50. Increasing the number of fins on the water side would not appreciably change the heat transfer rate; the high water-side heat transfer coefficients, compared to the methane side, mean that substantial heat transfer enhancement cannot be achieved by further improvements on the water-side.

6.4 Coefficient of Performance

It is helpful to use the previously defined coefficient of thermal performance (COP), Eq. (34) for evaluating the performance of the heat exchanger. The COP is the ratio of the heat transfer rate to pumping power and can vary with the geometry, the flow rates, and the thermal conductivity of the finned plate. Due to the modest effect of the thermal conductivity in the parametric range studied, the COP's for copper, aluminum, copper nickel, titanium, and the 10 W/mK polymer composites are relatively close. As may be seen in Figure 51, increasing pumping power - up to approximately 25W for this configuration, results in a steep increase in the COP followed by a more gentle decline, as the progressively higher pumping power leads to diminishing improvements in the heat transfer rate. For a typical pumping power of 200W, the COP's fall between 31 and 29 for the higher conductivity material, while the 5 W/mK polymer composite yields a value of 27.

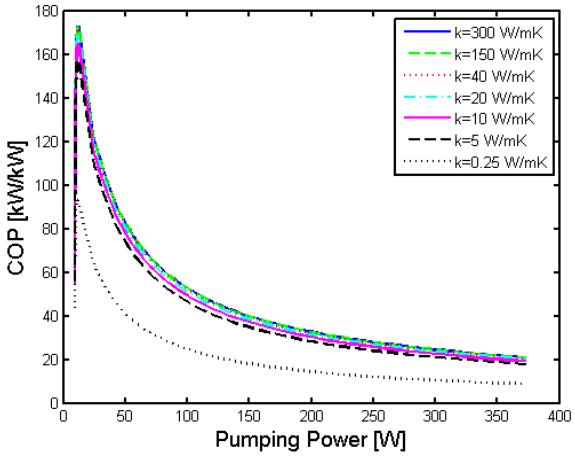

Figure 51: Gas/Liquid thermal performance in a counterflow parallel plate heat exchanger. W=L=1m, H_{fin}=10mm, t_f=t_b=1mm. Liquid velocity: 1 m/s, $N_{fins,g}$=100, $N_{fins,l}$=5

6.5 Mass-Specific Heat Transfer Rate

The impact of material choice on the mass-efficiency of the methane-seawater heat exchanger is shown in Figure 52, displaying the mass-specific heat transfer rate for the specified operating conditions. The mass-specific heat transfer rate is seen to continually increase with increasing pumping power, as the pure heat transfer rate did in Figure 50. Interestingly, when compared on this basis, with a fixed fin geometry, the low density (1.7 g/cm^3) thermally-enhanced polymer composite with a conductivity of 10 W/mK provides the best result – and is seen to be capable of transferring 1.6kW for every kg at 200W pumping power. By contrast, titanium, with a high density of 4.5 g/cm^3 and comparable thermal conductivity, can transfer just 0.7 kW/kg. For aluminum the values of this metric fall between the two, at about 1.1 kW/kg. Copper performs the poorest, due to its high density, with a mass-specific heat transfer rate of under 0.4 kW/kg.

Interestingly, doubling the number of fins on the methane side would decrease the mass-specific heat transfer rate, except for operation at low pumping powers. For pumping powers greater than approximately 100W, the added thermal performance is not enough to compensate for the increased mass. Due to its low added mass and weak effect on the

heat transfer rate, a five fold increase in the number of fins on the water side, from 5 to 25 for the 1m width, would result in only a modest decrease in the values of the mass-specific heat transfer coefficients– of about 10% - across the range of pumping powers. The total coefficient of performance, discussed next, shows similar trends.

6.6 Total Coefficient of Performance

Use of the total coefficient of performance, COP_T , which compares the heat transferred to the energy invested in the heat exchanger, Eq. (35), again favors the filled polymers. The polymer composites, with thermal conductivity of 5W/mK and 10W/mK, respectively, are seen to reach peak values of COP_T, above 60 for approximately 40W of pumping power and then decrease towards a common asymptote of 20 – for polymer and metallic materials – as the pumping power increases and begins to dominate the denominator of the COP_T. Due the high levels of energy invested in manufacturing the titanium, this material displays a far weaker optimum and a plateau-like dependence of the COP_T on pumping power. It is noteworthy that the copper and copper-nickel alloy, with their high thermal conductivity and moderate energy content, perform identically at a peak COP_T value of nearly 45. By contrast, the titanium heat exchanger provides the poorest value of the Total Coefficient of Performance barely reaching a value of 10, while aluminum's high conductivity compensates in part for the high energy content and reaches a COP_T of 40. Due to its low energy content, the unfilled polymer does display the highest values of COP_T, reaching 83 at low pumping powers, but has been previously shown to yield heat transfer rates that are far inferior to the other material choices.

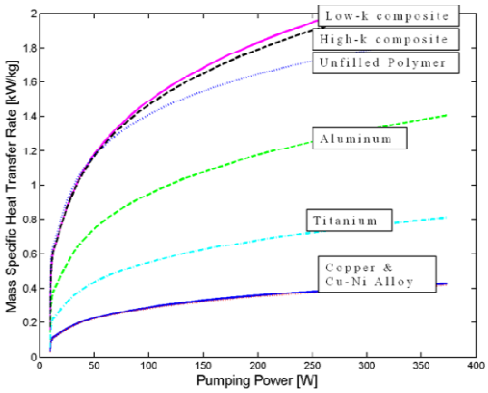

Figure 52: Gas/Liquid thermal performance per unit mass in a counterflow parallel plate heat exchanger. W=L=1m, H_{fin}=10mm, t_f=t_b=1mm. Liquid velocity: 1 m/s, $N_{fins,g}$=100, $N_{fins,l}$=5

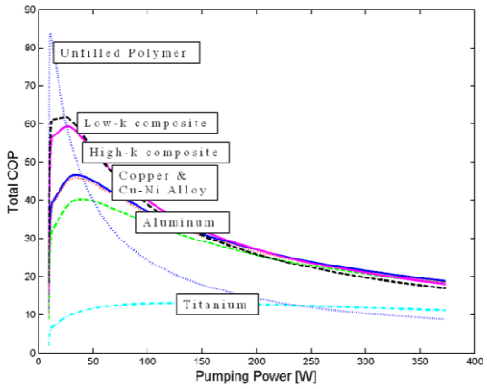

Figure 53: Gas/Liquid COP_T in a counterflow parallel plate heat exchanger. W=L=1m, H_{fin}=10mm, t_f=t_b=1mm. Liquid velocity: 1 m/s, $N_{fins,g}$=100, $N_{fins,l}$=5

6.7 Use of Least Material Relations

A more refined analysis of the mass specific heat transfer rate can be obtained by using relations for least-material fins on the gas-side of the modular heat exchanger. The array-based least material relation, equation (18) [54], can be used to minimize the fin mass required to achieve a specified heat transfer rate, for a given material and operating conditions, as discussed in Section 3.2. For identical heat transfer coefficients and fixed fin height, high thermal conductivity will result in relatively thin fins and low thermal conductivity in relatively thick fins, thus affecting the value of the mass-specific heat transfer rates. The validity of this array-based equation for the design of complete heat exchangers is discussed here.

The least material relation often yields extremely thin fins, especially for high conductivity materials with modest heat transfer coefficients. However, it must be realized that for the arrays considered herein, manufacturing constraints can be expected to limit fin thicknesses to approximately 0.1mm [69]. Thus, when the least material relation suggests thinner fins, a 0.1mm fin is used instead.

Applying Eq. (18) to the iterative determination of the optimum fin geometry for each operating condition and material, it is possible to again calculate the heat transfer rates, mass-specific heat transfer rates, and COP_T values and then compare them to the previously determined non-optimum values. The thermal performance, displayed in Figure 54, shows similar trends to Figure 50, the heat transfer rates rising asymptotically with pumping power and titanium attaining a rate of 4.4 kW at 200W while the 10W/mK polymer composite reaches 4.3 kW.

As a result of the least-material optimization, these somewhat reduced heat transfer rates are achieved with far more significant reductions in mass, especially for the metals, as may be seen in Table 11 and 4, for 50W and 200W of pumping power, respectively. In retrospect it may be understood that the initial chosen thickness of 1mm – though thin by conventional standards - was much thicker than necessary for fins fabricated of high thermal conductivity materials. The least material equation (18) allowed this thickness to be reduced significantly, with only slight reductions in the thermal performance.

The total heat exchanger module mass, including the base plate, for the high-k composite decreased from 3.5 kg to a least material configuration at 200W pumping power of 1.3kg. The titanium heat exchanger decreased even more, from 9.2kg to 2.0kg. The value of the least-material optimization is clearly seen in these substantial mass reductions and the consequent improvements of well above 100% in the mass-specific heat transfer metric, for all the materials except the low-k composite and even greater reductions at lower pumping powers. The COP_T values also improved, but only at low pumping powers where the energy invested in the mass plays the major role. While the focus of this paper is on the potential benefits of polymer composite heat exchangers, the very significant metal mass reductions, achievable by the use of the “least-material” optimization, are very noteworthy and – in themselves – represent a potentially profound contribution to energy efficiency and sustainability.

Due to these mass reductions, the asymptotic mass-specific heat transfer rate, shown in Figure 55, is seen to have increased significantly; the high-k thermally enhanced polymer

is at 2.5 kW/kg, below aluminum – which reaches 4.5-7 kW/kg – but well above the other materials considered in this analysis, including Titanium that attains a mass specific heat transfer rate of just 1.8 kW/kg or 72% of the 10W/mK polymer. Figure 56 displays the COP_T values and shows this metric for the high-k composite to have increased to a peak of approximately 70, compared to the value of 60 determined earlier for the non-optimum configuration. The least-material optimization has also benefited the titanium design, helping it attain a COP_T value of 30 - nearly double the non-optimum value, but still well below the polymer composites. The COP_T values have increased dramatically for copper and aluminum as well, towards 90 MJ/MJ. At larger pumping powers, any improvement is less apparent, as the energy invested in the material becomes small in comparison to the pumping power.

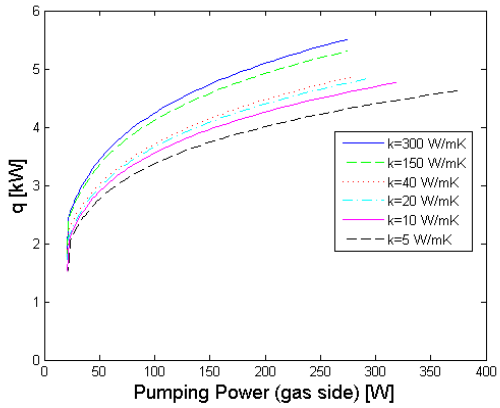

Figure 54: Gas/Liquid thermal performance in a least-material design counterflow parallel plate heat exchanger. W=L=1m, H_{fin}=10mm, t_b=1mm, t_f=t_{opt}. Liquid velocity: 1 m/s, $N_{fins,g}$=100, $N_{fins,l}$=5

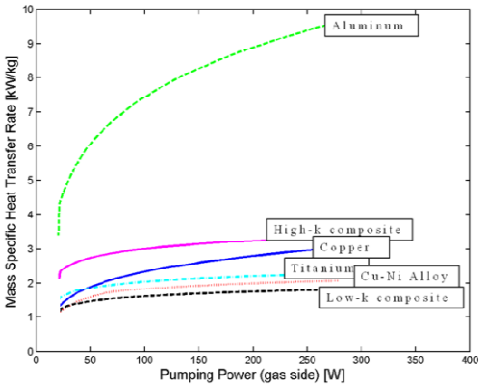

Figure 55: Gas/Liquid thermal performance per unit mass in a least-material design parallel plate heat exchanger. W=L=1m, H_{fin}=10mm, t_b=1mm, t_f=t_{opt} (t_{min}=0.1mm) Liquid velocity: 1 m/s, $N_{fins,g}$=100, $N_{fins,l}$=5

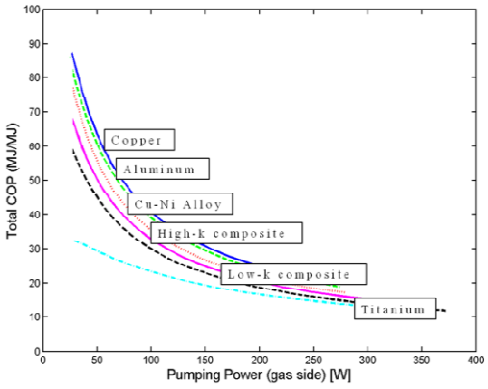

Figure 56: Gas/Liquid COP_T in a least-material design parallel plate heat exchanger. W=L=1m, H_{fin}=10mm, t_b=1mm, t_f=t_{opt}. (t_{min}=0.1mm) Liquid velocity: 1 m/s, $N_{fins,g}$=100, $N_{fins,l}$=5

	Initial Mass [kg]	Least-Material Mass [kg]	Initial Performance [kW/kg]	Least-Material Performance [kW/kg]	% Change
Copper	18.3	1.8	0.22	1.9	764%
Aluminum	5.4	0.6	0.75	5.9	687%
Cu-Ni	18.3	1.9	0.22	1.5	582%
Titanium	9.2	1.6	0.42	1.9	352%
High-k Composite	3.5	1.1	1.10	2.8	155%
Low-k Composite	3.5	1.9	1.10	1.4	27.3%

Table 11: Change in Mass-Specific Heat Transfer Rate (at 50W)

	Initial Mass [kg]	Least-Material Mass [kg]	Initial Performance [kW/kg]	Least-Material Performance [kW/kg]	% Change
Copper	18.3	1.8	0.35	2.79	697%
Aluminum	5.4	0.6	1.17	8.88	659%
Cu-Ni	18.3	2.2	0.35	2.00	471%
Titanium	9.2	2.0	0.68	2.20	224%
High-k Composite	3.5	1.3	1.70	3.24	91.6%
Low-k Composite	3.5	2.3	1.72	1.75	1.70%

Table 12: Change in Mass-Specific Heat Transfer Rate (at 200W)

A detailed thermofluid analysis of a 1 m^2 seawater-methane, finned-plate heat exchanger module for use in operating conditions typical of the natural gas liquefaction industry in the Persian Gulf was presented here. A 10 W/m-K polymer composite was found to provide nearly identical heat transfer rate to that of a corrosion-resistant titanium heat exchanger for the design and operating conditions examined, i.e. hot methane at 90°C, having flow rates of 0.01 to 0.1 m^3/s, and cooled by 35°C seawater. Furthermore, at 200 W pumping power, the polymer composite provided 3.2 kW/kg of mass-specific thermal performance, which is almost 50% higher than the titanium value. Polymer composites also showed total Coefficient of Performance (COP_T) values approximately twice that of a least-material titanium heat exchanger. The results contribute to establish the viability of using polymer composites for gas-liquid heat exchange applications involving seawater and other corrosive fluids.

The overall thermalfluid design of a polymer heat exchanger must seek to both minimize pumping power and achieve the greatest heat transfer. For a given pumping power, the fin thickness can be chosen to achieve sufficient heat transfer and minimize the use of material, saving energy in formation and fabrication as well as transportation. In this section, the least-material relation was shown to be a powerful tool in minimizing fin thickness with very small reductions in heat transfer rate and noteworthy gains in the mass-specific heat transfer rate.

Chapter 7: Experimental study of air/water prototype plate heat exchanger

In order to validate the analytical predictions of heat exchanger performance presented in Chapter 5 an experimental test facility was designed to study the thermal performance of a prototypical heat exchanger building block as a function of thermal conductivity. Testing was done using air and water as the working fluids. Air was chosen as the hot working fluid instead of methane for the following reasons:

(i) Air has a considerably lower specific heat capacity (1.006 kJ/kgK) than methane (2.293 kJ/kgK) at 50℃, and thus a higher temperature drop would be measured thereby reducing experimental error.
(ii) Safety issues are minimized.

Studies were done on prototype heat exchangers constructed using both unfilled and filled polymer materials having thermal conductivities of 0.25 W/mK [70], and 10 W/mK [28], respectively. The following sections present the prototype heat exchanger used, the construction of the test facility, instrumentation and data acquisition, error analysis, and results obtained.

The test strategy focused on comparing the thermal performance of an unfilled heat exchanger to that of a filled heat exchanger, for an air flowrate range 1800 to 3000 cm^3/s. The water flowrate was held constant.

7.1 Design and Construction of Experimental Setup

7.1.1 Prototype Heat Exchanger

It was important to be able to accurately measure thermofluid performance of a small scale heat exchanger. The prototype heat exchanger used, Figure 58.a, had dimensions of 5.0 cm x 5.2cm x 4.5cm. The air and water channel lengths in the stream-wise direction

are 5.2 cm 5.0 cm, respectively. The prototypical heat exchanger had fins on the air side, but not on the water side. This is typical in gas-liquid heat exchangers, as the bulk of the thermal resistance is on the air side; minimal enhancement is therefore needed on the water side.

The initial design of the heat exchanger was assessed through an analytical parametric analysis to assess the effects of fin height, fin spacing, and thermal conductivity on the predicted air temperature, with the results shown in Figure 57.

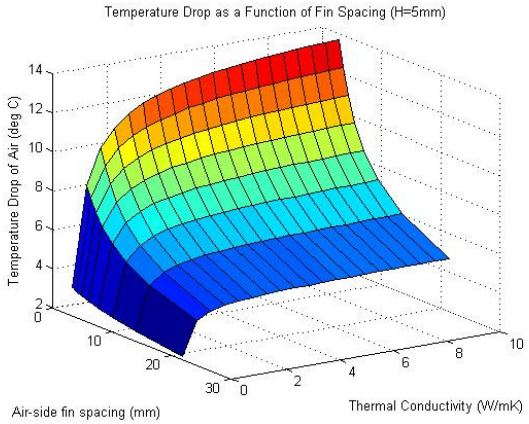

(a) H=5mm

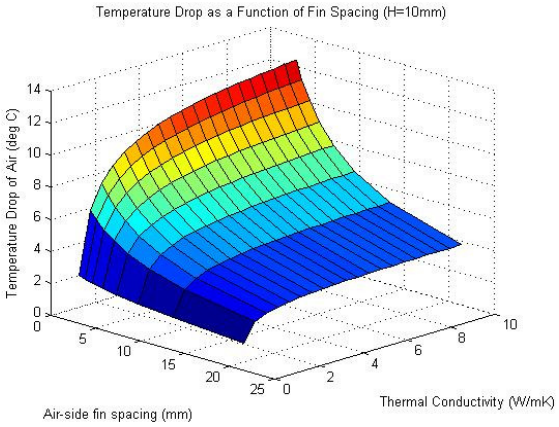

(b) H=10mm

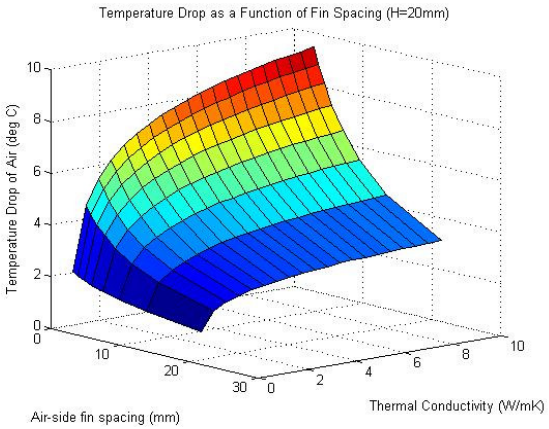

(c) H=20mm

Figure 57: Air-side temperature drop as a function of thermal conductivity and fin spacing. Air flowrate=3200 cm^3/s, Water flowrate=64 cm^3/s, L=5.2cm, W=5cm, t=2.5mm, Air Inlet Temp=50 °C, Water Inlet Temp=25°C

For a fixed flow rate, the maximum temperature drop is seen to decrease with increasing fin height as the flow velocity and corresponding heat transfer coefficient decrease with cross-sectional flow area increasing. Consequently the optimum prototype design for maximum temperature drop would have small fin spacing (under 5mm), and a thermal conductivity above 3 W/mK. However the heat exchanger prototype geometry for fin thickness and spacing was constrained by manufacturing capabilities of the injection molding machine used. Thin fins are difficult to remove from a mold, and a small fin spacing would require more material to be used than the available shot capacity [6.5 cm^3] of the injection molding machine [71]. With these considerations, fin thickness and spacing were set at 2.5 mm and 9.4mm, respectively (see Figure 58.b).

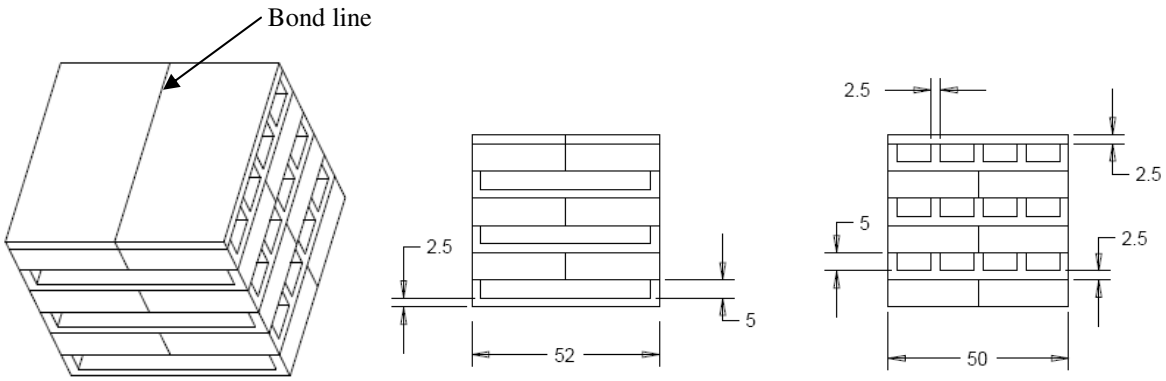

(a) Isometric View (b) Dimensions

Figure 58: Prototype Heat Exchanger Building Block Dimensions (in mm)

To maximize the overall heat exchanger size, air and water side plates were molded independently and subsequently bonded together using epoxy. No leaks were observed, and this is understood to be a viable commercial assembly technique, at moderate pressures.

The heat exchanger had three sets of air and water channels, with measurements obtained from the center channel. By having three sets of channels, the exterior channels absorb undesired thermal effects from the ambient conditions, as the external ambient air will be cooler than the air used as a working fluid. To minimize the mentioned extraneous effects, the heat exchanger external surfaces were insulated using 2cm (0.79 in) polyurethane foam having an R-value of 0.58-0.93 m^2K/W [72].

The unfilled case was an ABS polymer, while the filled polymer was a commercially available composite from PolyOne. Data was taken for air flowrates varying from approximately 1800 to 3000 cm^3/s.

To further understand the behavior of a polymer composite heat exchanger, it is important to not only understand the overall thermal performance, but also the temperature distribution within the polymer fins themselves. Modeling showed that using the conditions studied in Figure 57 would result in a temperature distribution less than 2.2℃. It was decided to both raise the air temperature to 70℃, as well as design a new heat exchanger with thinner fins, 2mm as opposed to 2.5mm, to increase the expected temperature to at least 3.7℃, as shown in Figure 59.

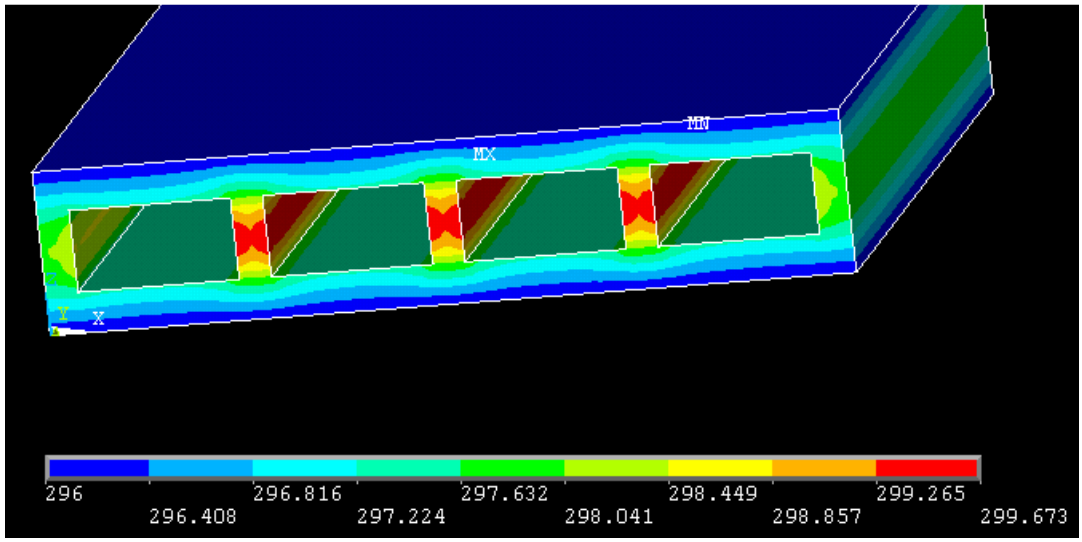

Figure 59: Numerical simulation of modified prototype heat exchanger module. T_{air}=70°C, T_{water}=23°C, t_{fin}=2mm, k=3.6 W/mK, h=40 W/m2K

Embedding thermocouples within polymer fins during the injection molding process was unrealistic for this case; it was decided the manufacture the heat exchanger alone, and drill holes to embed the thermocouples. Temperature was measured at 6 locations per fin, for three fins, two at the outlet side and one on the inlet side. The positions of the thermocouples are shown in Figure 60. All holes were drilled 1cm deep, to avoid edge effects.

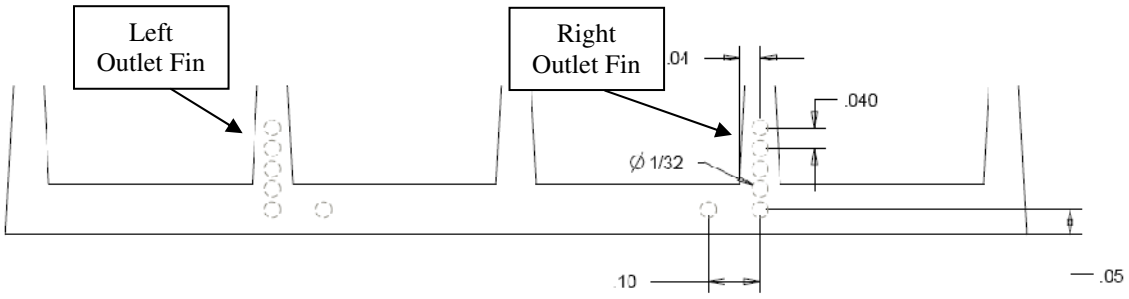

Figure 60: Thermocouple locations for study of fin temperature distribution, dimensions in inches

The completed heat exchanger can be seen in Figure 61.

(a) Isometric view of thin-finned HX

(b) Outlet view of thin-finned HX

Figure 61: Prototype thermally enhanced heat exchanger

A table summarizing the heat exchangers to be tested is given below.

Test	**Fin Thickness (mm)**	**Nominal Conductivity (W/mK)**	**Water Temperature (°C)**	**Air Temperature (°C)**
1	2.5	0.25	25	50
2	2.5	10.0	25	50
3	2.0	10.0	20	70

Table 13: Summary of heat exchangers studied

7.1.2 Test Facility

The experimental test facility developed to characterize the thermal performance of the prototype heat exchanger is shown in Figure 62.a. The air was heated to approximately 50 ℃, while the water was kept at an ambient temperature of 25℃.

The test facility draws in ambient air at room temperature, heats it to the desired temperature, and blows it across a flow straightener and downstream towards the heat exchanger. At fully developed hydrodynamic conditions within this pipe, the velocity is measured. A manifold connects the pipe to the heat exchanger, and the temperature is measured at the inlet and outlet of the heat exchanger. The somewhat cooler air is then exhausted to the ambient. Water flows in, driven by the building water pressure. It is passed across a heater, to ensure a consistent temperature, and then through a flowmeter. The water piping is then attached to a manifold, distributing the water across the heat exchanger channels. The temperature is again measured at the inlet and outlet, though not with the resolution as on the air side. The water flowrate is set sufficiently high to maintain isothermal conditions on the water side, and thermocouples are used to verify this. The actual test facility is depicted in Figure 62.b.

Temperature and flowrate measurements are acquired real-time on a PC running LabVIEW software, which both displays the respective measurements and records it for future processing. A schematic of the measurement process is provided in Figure 63. Data acquisition consisted of 18 channels, 16 of which were allocated for temperature measurement using thermocouples, and two for fluid flowrate measurement.

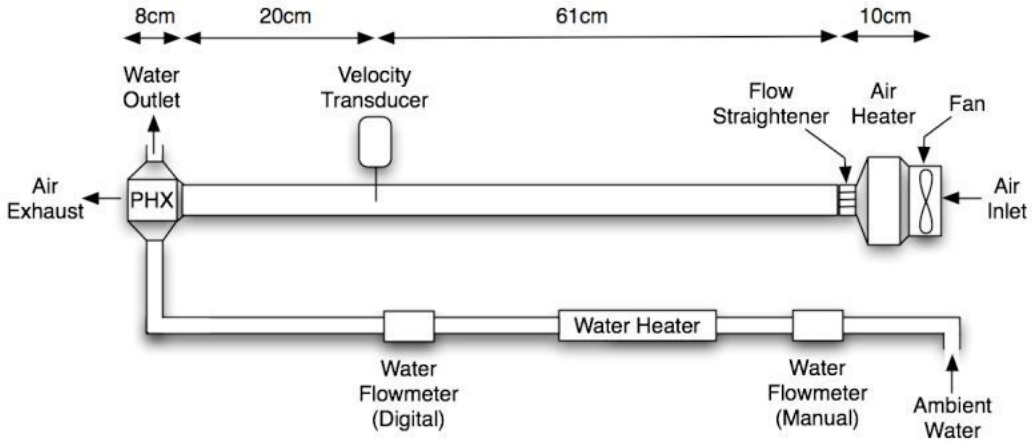

(a) Experiment Diagram

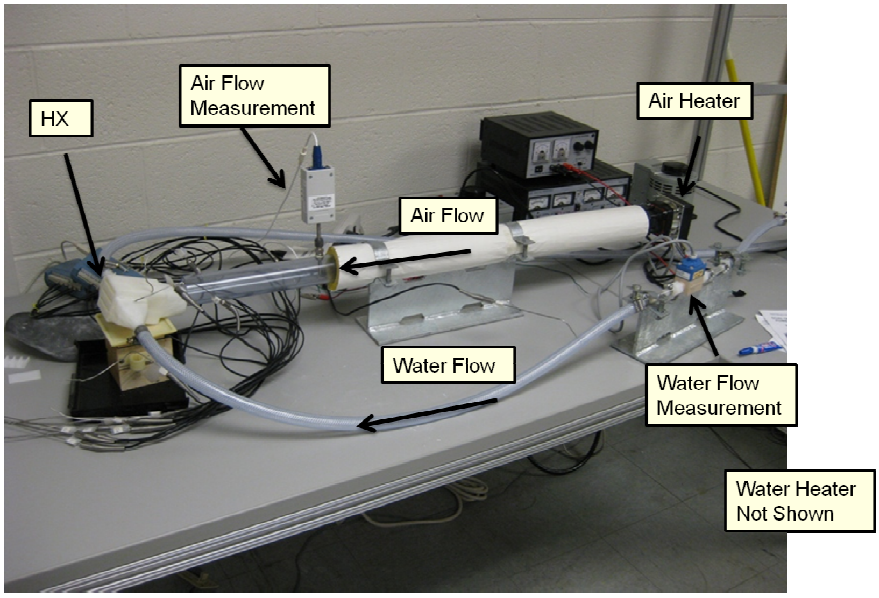

(b) Actual test facility

Figure 62: Test Facility

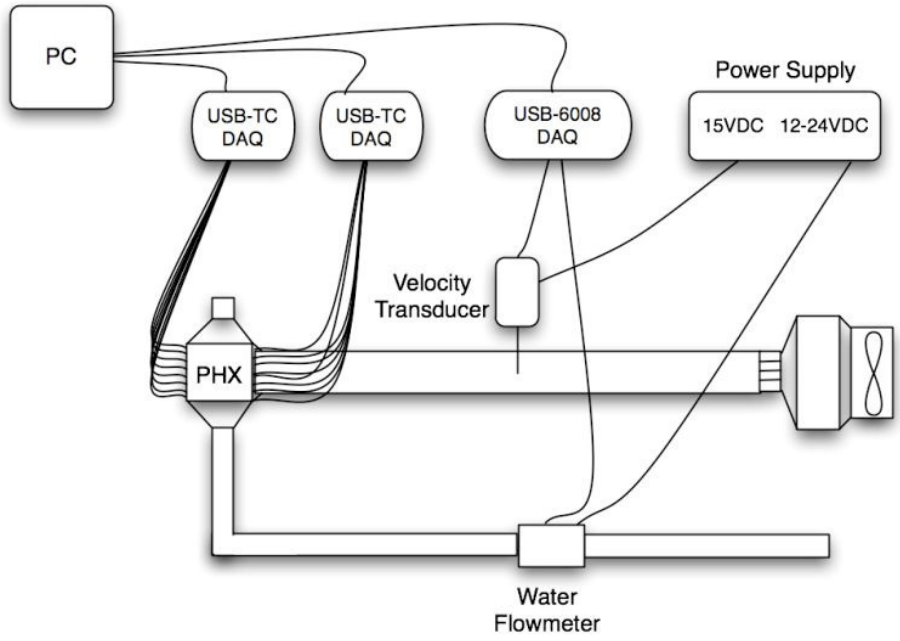

Figure 63: Schematic of Measurement Process

A circular PVC pipe of diameter 41 mm was used as an air conduit, with its external surface insulated using fiberglass pipe insulation having ½" wall thickness. The insulation has a R-value of 0.42 m^2K/w at 23℃ [73]. A honeycomb flow straightener [74] is used, ¾" thick with ¼" honeycomb, cut to fit the dimensions of the air conduit.

To maintain a straight and uniform flow path, the air conduit size was chosen based on a 4 cm square axial fan whose pressure-flow performance curve shown is Figure 64. The experimental pressure drop through duct, flow straightener, manifold, HX is calculated by

$$\Delta P = K_{L,ent} * \frac{1}{2}\rho V^2 + K_{L,fs} * \frac{1}{2}\rho V^2 + K_{L,man} * \frac{1}{2}\rho V^2 + \Delta P_{HX} \quad \textbf{(37)}$$

where the loss coefficient for the flow straightener, $K_{L,fs}$ is taken as 0.66, according to Groth [75] and the entrance and exit coefficients are a function of the change in area [76]. The friction factor given by Shah & London [77], Equation (38), is used to calculate the pressure drop over the heat exchanger for developing flow.

$$f_{app} \cdot Re = 3.44(x^+)^{-0.5} + \frac{\frac{K(\infty)}{4x^+} + fRe - 3.44(x^+)^{-0.5}}{1 + C^{'}(x^+)^{-0.2}} \quad \textbf{(38)}$$

where K(∞), fRe, and C' are given as a function of the duct aspect ratio, 1.28, 15.548, and .00021 respectively. Calculated fan operating point is shown in figure 64.

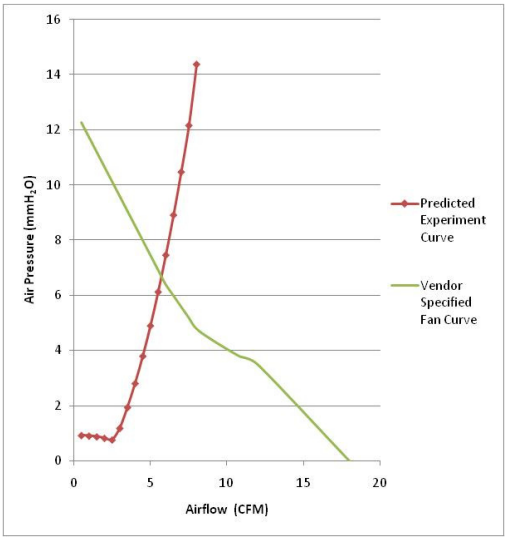

Figure 64: Vendor specified fan pressure curve, R124028XU [78]

The primary pressure drop components are listed in Table 14. The bulk of the pressure drop in this experimental set up is due to the flow straightener and HX manifold, not the heat exchanger itself. The large fin spacing mandated by manufacturing constraints minimizes the pressure drop over the heat exchanger. The initial air entrance from the heater to the pipe is a very gradual shift from a larger area of the heater to the smaller area of the pipe diameter, and results in negligible pressure drop.

Region	Pressure Drop (mm H_2O)	Pressure Drop (Pa)
Entrance	0.0133	0.13
Flow Straight.	1.378	13.5
HX Manifold	1.153	11.3
HX	0.633	6.2
Total	3.17	31.1

Table 14: Calculated air side pressure drop components of heat exchanger test loop.

The above analysis demonstrates the operating point of the test facilitate, and ensures that the fan will provide sufficient pressure to the air. Once expected flowrates and pressure drops were known, flowmeters could be chosen for the highest accuracy at this expected operating point.

7.1.3 Instrumentation

Instrumentation is composed of flowmeters for both air water measurement, as well as process heaters for both fluids. The temperatures are measured through an array of thermocouples on the heat exchanger.

Flowmeters

The performance specifications of the flow rate meters used for air and water measurement are given in Table 15.

Part	Supplier	Part Number	Capacity	Output	Measurement Accuracy
Air Velocity	Omega Eng.	FMA-902-V-S	0-3260 cm^3/s	0-5 Volts	3.5%
Water Flow	Mcmaster	3437K62	6-70 cm^3/s	0.089 mL/pulse	3.3%

Table 15: Test facility Flowmeters

Air flowrate was measured using an Omega FMA-900 velocity transducer, whose operation is based on thermal anemometry. It uses two RTD's, one to sense velocity and another to compensate for the ambient air temperature. By maintaining a constant temperature differential with the ambient, the meter determines flow velocity by measuring the cooling effect on the velocity sensor. This meter design was selected as opposed to an obstruction flowmeter, which would have introduced a significantly higher pressure drop, and therefore lower fan supplied flow rate. For reference, many air flowmeters use differential pressure measurement, and are designed for high pressure compressed air. In such a case, the pressure drop over the flow meter would be insignificant compared to the air pressure. This is not suitable for this application, as the

resulting pressure drop could represent a large fraction of the overall system pressure loss.

By using this velocity transducer, it was possible to transverse the channel and determine the velocity at different locations to permit accurate computation of the pipe flowrate. To determine the air flowrate through the pipe, a velocity traverse is performed based on ASHRAE standards [79]. Velocity readings are taken at several positions across the diameter of the pipe. The position of these points relative to the wall is determined by the log-Tchebycheff rule, which minimizes error caused by failure to account for losses at the duct wall [80]. A straight average of the individual velocity readings can be used. The velocity transducer is then placed in the location of this average velocity. The velocity traverse showed a fully developed turbulent profile in the pipe.

Installation of the velocity transducer required it to be placed 15 diameters downstream of the flow straightener in order to ensure fully developed turbulent flow conditions (Re~4000), for which it is calibrated for. It also required 5 diameters of piping downstream of the meter itself, coming to 81cm of piping total.

Water flowrate was measured using a Vortex Eggs Delta-Pulse flowmeter. It used vortex principles for flowrate measurement [81] , whereby a bluff body generates vortices, and the shedding of these vortices are proportional to the Reynolds number, and hence the flowrate. This meter outputs a single pulse for every 0.089mL, with flowrate calculated based on the frequency of these pulses. In order to maximize accuracy, simulations of the prototype heat exchanger were done at expected conditions for air and water flowrates, and these results were used to purchase flowmeters most suitable. Pressure drop in the flowmeter was calculated according to equation (39), where ΔP_o is the pressure loss at the maximum flowrate, 31 kPa. For an expected water flowrate of 3.785 L/min (or 1 gpm) a pressure drop of 27.8 kPa is expected. This is relatively minor compared to an expected pressure head of around 500 kPa.

$$\Delta P = \Delta P_o \frac{\rho}{\rho_o}\left(\frac{Q}{Q_o}\right)^2 \quad \textbf{(39)}$$

Both the air and water meters provided digital outputs to be processed and recorded through a computer, using Labview software, as discussed later.

A panel-mount manual flowmeter, was used to verify the output of the Eggs Delta –Pulse flowmeter. Both meters show equivalent readings when the experiment is running.

Process Heaters

The specifications of the process heaters used for the bulk heating of air and water test sections are given in Table 16.

Part	**Supplier**	**Part Number**	**Capacity**	**Resultant Fluid Temp**
Air Heater	Mcmaster	20055K111	200W	24-80℃ @ 3000 cm^3/s
Water Heater	Mcmaster	7400T14	1200W	22-27℃ @ 64 cm^3/s

Table 16: Process heater specifications.

A Farnam Custom products axial fan heater [82] was used to heat inlet air using a resistive wire coiled within an enclosure (see Figure 65) using the same mounting holes as a typical 80mm computer cooling fan. A process water heater was used to compensate for tap water supply temperature fluctuations which were between 22-24℃. To eliminate such temperature fluctuations, the inlet supply water was heated to 25℃, The water was heated resistively, using a process heater with the amount of heat supplied to the water heater manually controlled by varying the supply voltage. Both the fan and water heater were AC powered through two variable voltage output transformers. A 200W heater was sufficient to heat air up to 70℃ at flowrates of 1000-3000 cm^3/s. A larger 1200W heater was required to heat the water from 23 to 25℃ because of the larger specific heat capacity of water. The heaters were sized according to steady flow equation (40).

Figure 65: Resistive coil axial fan heater

Figure 66: Airflow straightener

(40)

After the air was heated, it passed across the flow straightener, an aluminum honeycomb with cells at 45° angles to each other, 6mm in size.

Temperature Measurement

For temperature measurement, J-type iron-constantan thermocouples, with a 1/16" stainless-steel sheath, were used. The sheaths ensure that the thermocouples are rigid and stay in place in the middle of a channel. They also prevent water corrosion of the thermocouple junction. Thermocouples were placed according to Figure 67, symmetrically on the air inlet and outlet of the heat exchanger. Because the rise in the water temperature was expected to be very small (less than 0.1℃) the water flowrate was set to a constant value of about 60 cm^3/sec, and taken as isothermal. A single thermocouple was place at the inlet and outlet to verify this assumption.

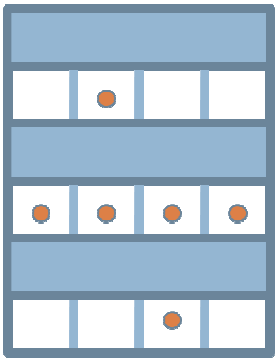

Figure 67: Air side thermocouple placement
on prototype heat exchanger

For the second phase of this experiment, where the temperature distribution within the fins was measured, T-type thermocouples made from Special Limits of Error wire, for improved performance over standard wire, were chosen for their good tolerance value of 0.5℃ in the applicable range [83], significantly better than the previously used J-type thermocouples. These thermocouples have a sensitivity of 42.4 μV/°C in the relevant temperature range. 12 Stainless-steel sheathed thermocouples (Omega Part No. TMQSS-020U-6) were used on the outlet side for rigidity and easy of mounting. On the inner face of the heat exchanger, PFA-insulated thermocouple wires were used (Omega Part No. 5TC-TT-T-36-36), to facilitate routing of the wires out of the airflow path. The thermocouples were attached to the polymer using Arctic Silver thermally conductive epoxy with an approximate thermal conductivity of 7.5 W/mK [84]. All other equipment used in the experiment was identical to that described earlier, although a 3rd USB-TC data acquisition unit was required to accommodate the additional thermocouple signals.

The use of T-type thermocouples, with a high conductivity copper wire, present a potential source of error. Fortunately, the actual copper wire is 0.13mm in diameter, and the overall diameter of the thermocouple assembly is 0.79mm, so the copper is only 3% of the total area. To further confirm this, a composite conductivity, 3% for copper and 97% representing the polymer insulation, of 10 W/mK was studied to determine the effects of the thermocouple on the overall module heat transfer rate. In an isotropic heat exchanger module, increasing the inlet thermocouple conductivity from 0.5 W/mK to 10 W/mK only increased the heat transfer rate 2.6%, from 12.49W to 12.82W. This is well below the experimental uncertainty, and not likely to play a significant role.

Data Acquisition

A USB-TC thermocouple input module from Measurement Computing is used to acquire data from the thermocouples. Two modules were used, each with 8 thermocouple channels and a 24-bit resolution. A high resolution analog-to-digital converter is necessary as thermocouples are extremely sensitive to temperature changes;

for a J-type thermocouple the sensitivity is on the order of 50mV/°C, which must be first amplified and then converted from an analog to a digital signal [85]. Cold junction compensation is provided through two integrated high resolution temperature sensors on either side of the module, for maximum measurement accuracy. This is necessary to account for variations in the signal caused by connecting the thermocouple wires to the dissimilar metal contacts of the module.

A USB-6008 multifunction data acquisition unit from National Instruments is used to capture data from both the air velocity transducer and the water flowmeter. This is not as high of a resolution as the thermocouple data acquisition unit, but the 12 bit resolution combined with a 10 kS/s sample rate is adequate for the flowmeters used. This unit also interfaces with Labview and facilitates the necessary signal processing and analysis.

7.1.4 Software

Labview 8.5 was used to acquire, process, and store the data from all instrumentation. The USB-TC thermocouple data acquisition modules temperature outputs are calibrated in degrees Celsius, so no further processing was necessary with the signals sent directly to the output measurement file. Calibration and configuration of the modules is done through a separate software, *Instacal*, by Measurement Computing [86].

In Figure 68, data acquisition pseudocode and the corresponding Labview block panel are represented in (a) and (b).

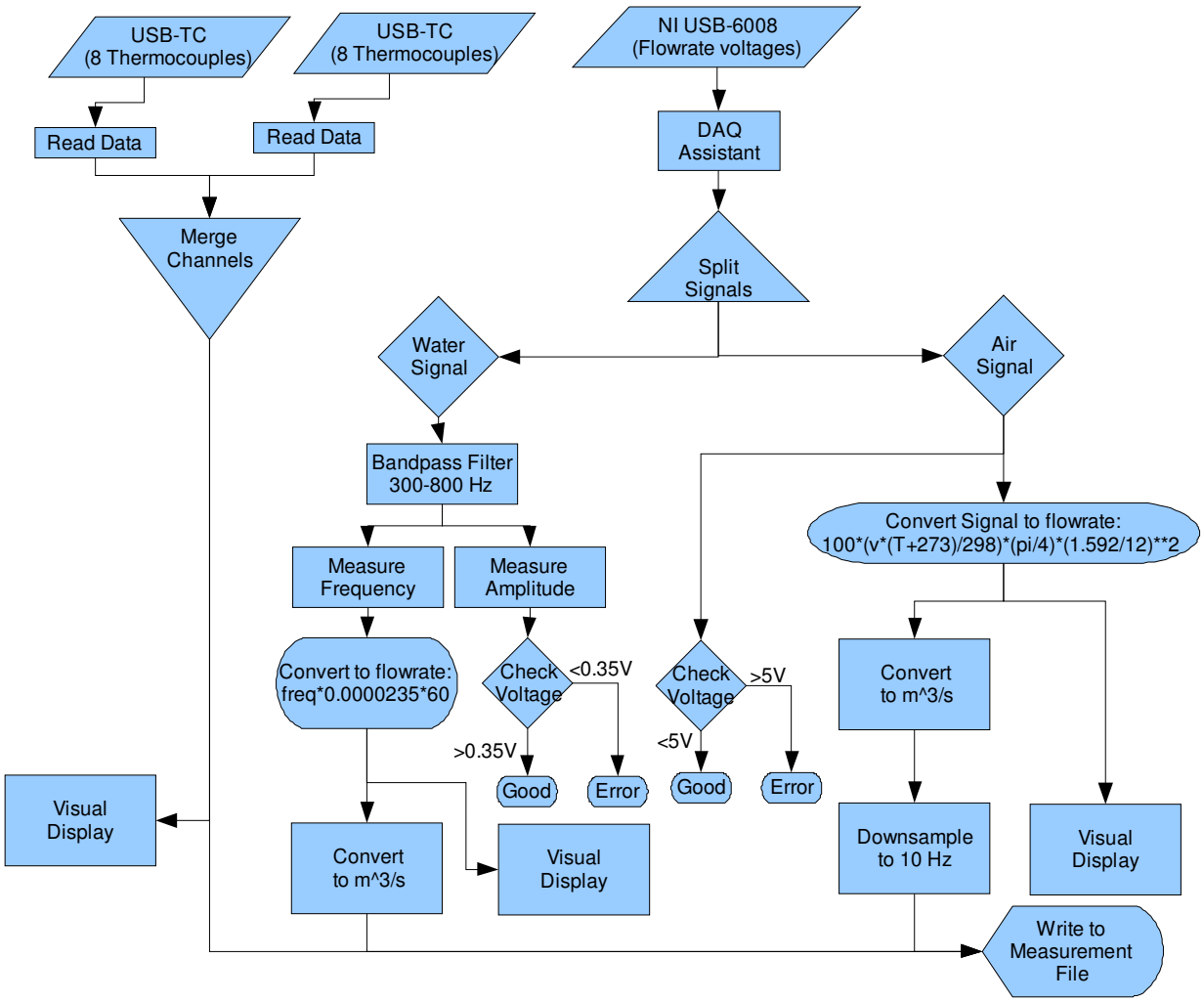

Figure 68 (a): Pseudocode Representation

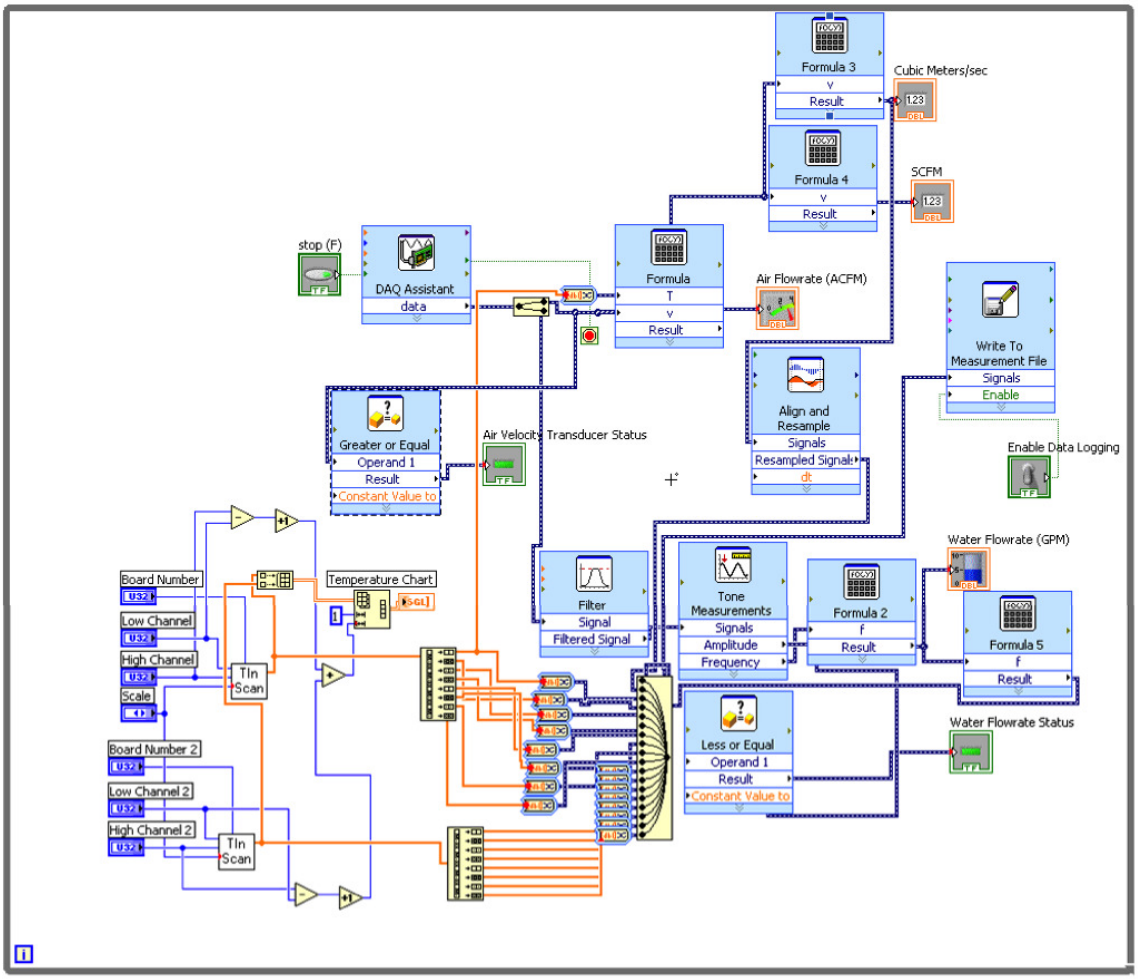

Figure 68 (b): Labview Block Diagram

Figure 68. Instrumentation and measurement process.

Data from the air velocity transducer is read in as a voltage from 0-5V. Because the transducer is calibrated for 500 SFPM, this signal needs to be multiplied by 100 to derive a velocity measurement. Velocity was converted from SFPM to AFPM using equation (41). The pressure correction can be neglected, because the difference between the operation pressure of the system and atmospheric pressure is minimal. The maximum pressure head of the fan as shown in Figure 64 is 0.137 kPa. The temperature correction is very important, as the air is being heated significantly above ambient temperature and therefore the vendor specific performance curve is not applicable at high temperatures

$$AFPM = SFPM\left(\frac{T + 273.15}{298.15}\right)\left(\frac{760\ mm\ Hg}{P}\right) \quad \textbf{(41)}$$

Labview can be used to convert the velocity output to a flowrate, based on the channel area. This flowrate is converted to metric units and sent to the output measurement file.

To acquire a water flowrate from the pulse flowmeter requires more processing. The signal is first filtered based on the expected frequency. The expected water flowrate is approximately 3785 cm^3/min, and with a flowmeter output of 0.089 pulses/mL, this gives an expected frequency of 709 pulses/sec. A bandpass filter is used in Labview, with a low cutoff frequency of 300 Hz and a high cutoff frequency of 800 Hz. A tone measurement function is then used to measure the amplitude and frequency. The amplitude is used to check that the flowmeter is operating correctly, and the frequency is used to calculate the final value of the flowrate. This value was compared to the value read from the manual flowmeter and showed accuracy within 5%.

All the acquired signals are displayed in real-time on the screen, as well as written to an Excel-compatible file for further analysis.

7.1.5 Error Analysis and Calibration

An error analysis was completed to determine the relative error that could be expected from the experiment. Two different methods for calculating the experimental uncertainty were used, sequential perturbation analysis, and design stage uncertainty analysis. The results were compared to each other as a process check.

Three primary sources of error in measurements for this experiment were identified; temperature, and air and water flowrate measurement. The error analysis was done based on the computation of the experimental heat transfer rate from the air, given in equation (42). The temperature difference on the water side of the heat exchanger was very small, and thus it was decided to take the water side as isothermal, as thermocouple measurements would not provide sufficient accuracy.

$$Q = \dot{m}c_p(T_{out} - T_{in}) = \rho VAc_p(T_{out} - T_{in}) = \frac{P}{RT}VAc_p(T_{out} - T_{in}) \quad \textbf{(42)}$$

A sequential perturbation analysis was performed, as described in Figliola &Beasley [87] and Moffat [88]. In this analysis c_p was taken as a constant as it varies insignificantly in air from 20 to 50℃. A sequential perturbation analysis is done by listing all the relevant variables, as well as their uncertainties. The heat transfer rate is calculated for the nominal values. Each independent variable is then increased by its respective uncertainty value, and the heat transfer rate is again calculated. The difference between the nominal heat transfer rate and these values is calculated. The root-sum-square of these values is the absolute uncertainty, and the relative uncertainty is this value divided by the nominal value. The resultant uncertainty is 15.72%.

Input	Est. Unc.	Data	In each col, the title variable has been increased by its uncertainty					
Variables			Pressure (kPa)	Temp (℃)	V (FPM)	Diameter (m)	Temp, in (℃)	Temp, out (℃)
P	0	101.325	**101.325**	50	430	0.040437	50	45
T	0.54	50	101.325	**50.54**	430	0.040437	50	45
V	15.05	430	101.325	50	**445.05**	0.040437	50	45
A	0.00025	0.040437	101.325	50	430	**0.040687**	50	45
Ti	0.54	50	101.325	50	430	0.040437	**50.54**	45
To	0.54	45	101.325	50	430	0.040437	50	**50.54**
Q		15.41355	15.41355	15.38784	15.95303	15.60473	17.07822	13.74889
Ind. Con.			0	0.025714	-0.53947	-0.19118	-1.66466	1.664664
Abs. Unc.	2.423							
Rel. Unc	**15.72%**							

Table 17: Sequential Perturbation Analysis

A design stage uncertainty analysis can also be done, as shown in Taylor [89]. This method is shown in equation (43) for the heat transfer rate calculation in equation **(42)**:

Heat Transfer Uncertainty: $\sqrt{\sqrt{(\%V)^2 + (\%A)^2 + (\%T)^2}^2 + \left(\frac{\sqrt{T^2+T^2}}{\Delta T_{exp}}\right)^2}$ **(43)**

The uncertainty values from each component are summarized in Table 18.

	Initial Uncertainty	% Full Scale	Overall Uncertainty
Air Flowmeter	**2.5%**	**87%**	**3.5%**
Water Flowmeter	**3.0%**	**91%**	**3.3%**
Pipe Area	**0.5%**	**N/A**	**0.5%**
Temperature Error	**0.54℃**	**N/A**	**0.54℃**

Table 18: Experimental Uncertainty Values

A random sampling of 5 thermocouples was used for initial calibration. They were tested in an ice bath as well as boiling water, and an average thermocouple error of 0.44 °C was found. The USB-TC data acquisition unit gives a measurement error of 0.312 °C, according to the manufacturer [86], resulting in a combined error of 0.54°C. An uncertainty of 3.7 % results for the (PV/T) term and 15.3% for the (T_{out}-T_{in}) term. The latter dominates because of the small expected delta of 5 °C. An overall uncertainty of 15.7% is found. As expected, this result is equivalent to the result from the sequential perturbation analysis. This high level of uncertainty underscores the importance of properly calibrating the thermocouples.

To reduce the overall uncertainty, a more thorough thermocouple calibration was done on all thermocouples, by reading the raw voltage when immersed in an ice bath and in boiling water. The raw voltage can be converted to a temperature value by equation (45) with constants with the NIST specified constants [90] in Table 19. By bringing the thermocouple uncertainty down to 0.1 °C, the overall error is reduced to 4.5%.

$$T = c_0 + c_1V + c_2V^2 + c_3V^3 + c_4V^4 + c_5V^5 + c_6V^6 + c_7V^7 + c_8V^8 \quad \textbf{(44)}$$

J-Type Thermocouple Constants	T-Type Thermocouple Constants
0 °C to 760 °C **0 mV to 42.919 mV**	**0 °C to 400 °C** **0 mV to 20.872 mV**
C0 = 0	C0 = 0
C1 = 1.978425 * 10^1	C1 = 2.592800 *10^{1}
C2 = -2.001204 * 10^-1	C2 = -7.602961 *10^{-1}
C3 = 1.036969 * 10^-2	C3 = 4.637791 * 10^{-2}
C4 = -2.549687 * 10^-4	C4 -2.165394 * 10^{-3}
C5 = 3.585153 * 10^-6	C5 = 6.048144 * 10^{-5}
C6 = -5.344285 * 10^-8	C6 = -7.293422 *10^{-7}
C8 = 0	C8 = 0

Table 19: NIST Thermocouple Coefficients for J & T-Type Thermocouples

Figure 69 shows the resulting voltage for all 16 thermocouples, labeled according to channel and board number. The thermocouples show small variations, giving voltages in a 0.05mV range at freezing, and a 0.1mV range at boiling. A linear slope is also drawn between 0°C and 100°C, to clarify the curvature of the equation at the expected temperature values of 40-50°C. This is enlarged in Figure 70.

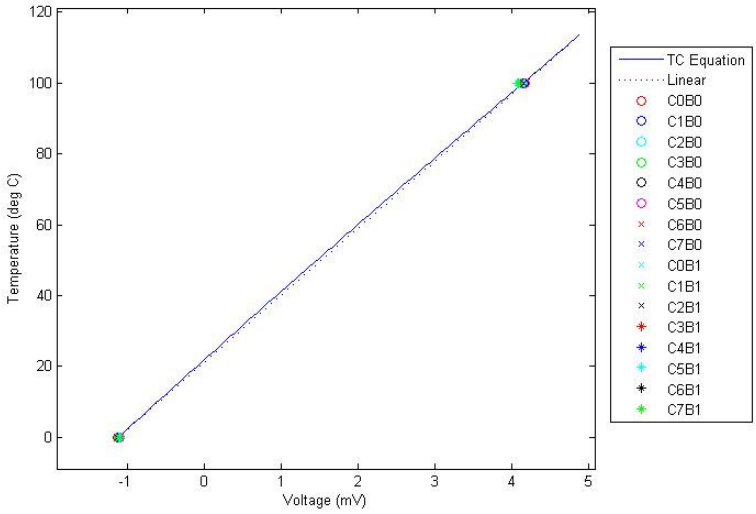

Figure 69: Thermocouple calibration: temperature versus voltage

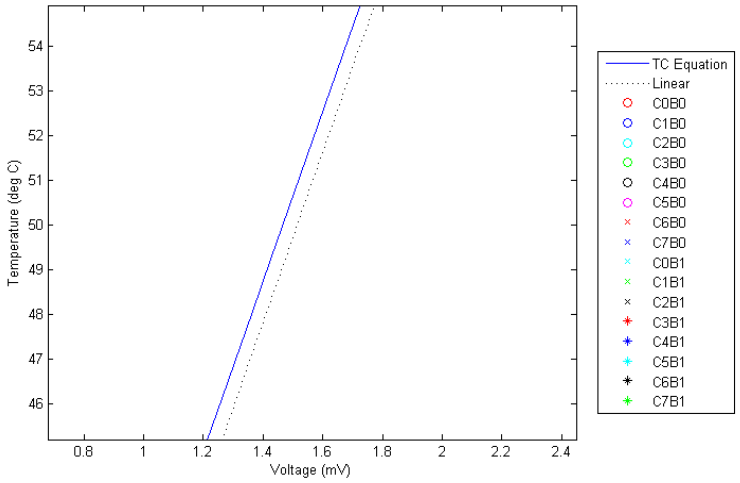

Figure 70: Nonlinearity of thermocouple equation

The thermocouple equation does differ notably from the linear slope at the expected temperature range, by approximately 0.05mV. This deviation is consistent from 45 to 55℃, and should not affect the temperature delta measured by thermocouples calibrated at freezing and boiling. A potential source of error in this case is the atmospheric pressure, which may affect the boiling temperature differently on different days. This is not significant, as calibration is done primarily to minimize uncertainty in the temperature difference calculation, not the absolute temperature.

A thorough thermocouple calibration was again completed for the second phase of this experiment using T-type thermocouples, for all thermocouples, by reading the raw voltage when immersed in an ice bath and boiling water. The voltage signal can be converted to a temperature value by equation (44), using NIST specified constants [90] in Table 19.

Figure 71 shows the resulting voltage for all 18 T-type thermocouples. This calibration process revealed a standard deviation of 0.129℃, and a mean residual of 0.0849℃ difference from the expected value. A linear slope is also drawn between 0℃ and 100℃, to clarify the curvature of the equation.

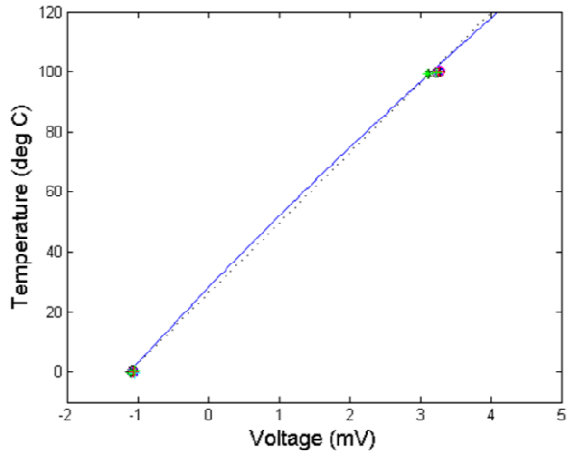

Figure 71: Thermocouple calibration: temperature versus voltage

The total thermocouple error is compiled in Table 20 for both the fin and air temperature measurements. The RMS accuracy of the fin temperature measurement, at 0.323, is appropriately much better than the accuracy of the air temperature measurement, 0.539, as the expected temperature gradient is significantly smaller.

	Thermocouple Accuracy	**Measurement Accuracy**	**RMS Accuracy**	**Expected Temp Measurement**
Fin Temperature	0.085	0.312	0.323	22
Air Temperature	0.44	0.312	0.539	70

Table 20: Thermocouple accuracy for temperature distribution

While studying a percentage error is not generally appropriate for temperature measurements, an "effective error" can be used to study how significant the thermocouple accuracy is in terms of reference temperatures. In Table 21, the RMS accuracy of the fin thermocouples is compared relative to the ambient (25°C), water (17°C) and the fluid temperature difference (53°C), all of which are below 2%.

	Relative to Ambient	**Relative to Water**	**Relative to Fluid ΔT**
Effective Error	1.3%	1.9%	0.6%

Table 21: Thermocouple effective error

Furthermore, a temperature transverse of the channel was done to determine the temperature uniformity of the flow. Significant stratification of the temperature profile was observed in the vertical direction, especially for low flowrates. This emphasizes the importance of measuring the individual air temperatures at the entrance to each heat exchanger channel. Results are shown in Appendix 3.

Upon seeing the stratification in the flow, further analysis was completed. Figure a.6 shows that the temperature gradient varies from 8℃ at the heat exchanger exit to 1.5℃ at the entrance side. Also, Figure a.7 shows that taking an average temperature value, as opposed to summing the heat transfer rates from each individual channel, yields essentially identical heat transfer rates.

7.1.6 Experimental Error and Anisotropy in Numerical Modeling

7.1.6.1 Single Fin

The effects of anisotropy on a single fin, at low and high heat transfer coefficients, are first compared, as introduced in Section 4.4.2. The results of an anisotropic fin (Figure 22) as determined by molding simulations, are compared in Figure 72 to a fin with an isotropic conductivity of 3.6 W/mK, the value experimentally determined through use of a flash diffusivity technique. Notably this experimental value is much lower than the manufacturer's listed conductivity of 10 W/mK. The isotropic fin on the left – with h=40 W/m^2K, θ_b=55K, 5mm tall and 2.5mm wide- conducts 30.1W of heat while the anisotropic fin conducts only 29.1W.

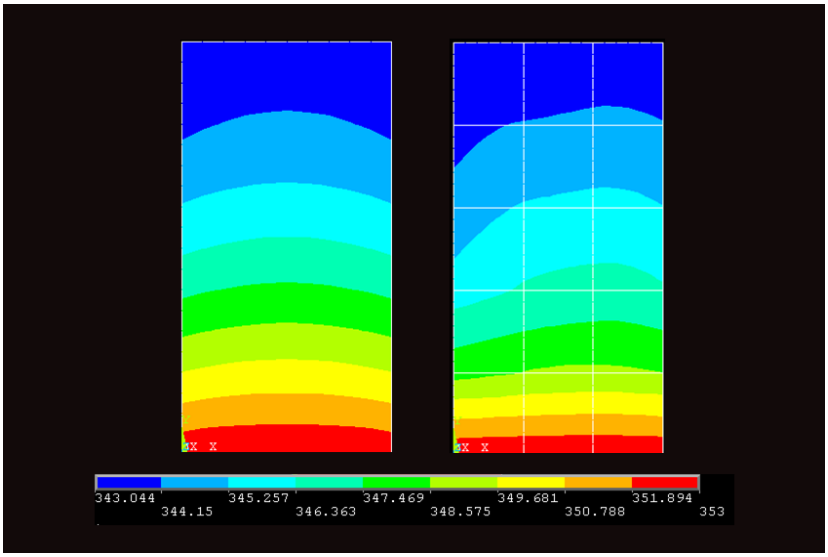

Figure 72: Comparison of temperature profile in an isotropic fin (k=3.6 W/mK) to an anisotropic fin (k's as discussed in Figure 22) t_f=2.5mm, H=5mm, h=40 W/m^{2}K, θ_b=55K

The difference between the two is even more significant at higher heat transfer coefficients (Figure 73). With h=1000 W/m^{2}K, θ_b=55K, a 5mm tall and 2.5mm wide fin shows a heat transfer rate of 222W is seen for the isotropic case, but 186W for the anisotropic case.

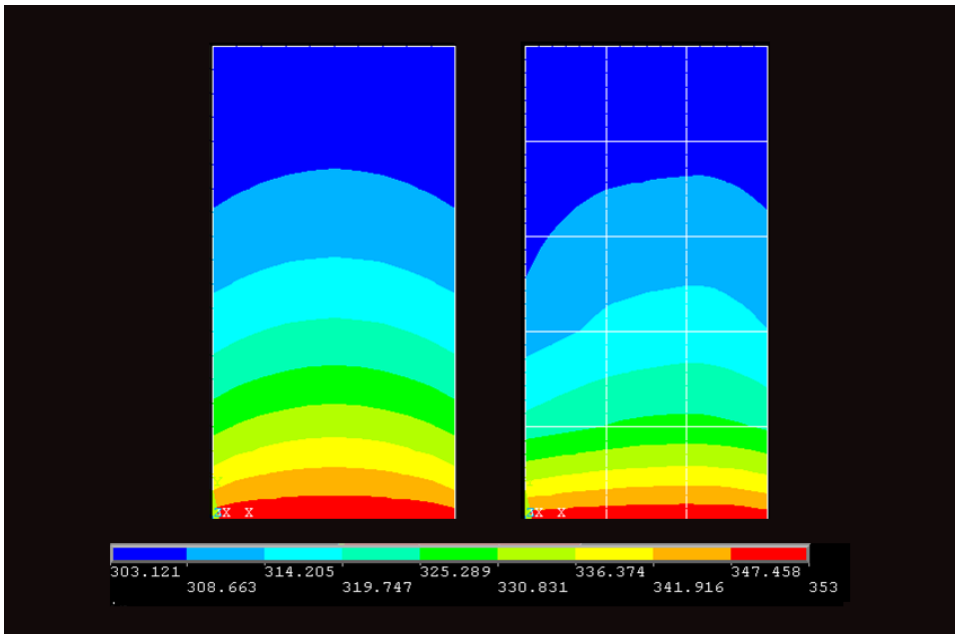

Figure 73: Comparison of temperature profile in an isotropic fin (k=3.6 W/mK) to an anisotropic fin (k's as discussed in t_f=2.5mm, H=5mm, h=1000 W/m^{2}K, θ_b=55K

Various techniques can be used to study how this anisotropy affects the thermal performance of the fin. The 15 different fin conductivity "blocks" were rearranged into three configurations, and the resulting performance compared. First the existing set of blocks, which resulted from flow simulations, were rearranged into a "best performing" configuration. The blocks with high conductivity in the y-direction were placed at the base, and the ones with low axial conductivity were placed at the tip. Next the thermal conductivity values were changed to maximize the axial conductivity, while maintaining a constant arithmetic mean conductivity**.** A low axial conductivity case was also used. The results are shown in Table 22 for two heat transfer coefficients, 40 W/m^2K and 1000 W/m^2K, both with t_f=2.5mm, H=5mm, θ_b=55K and compared with the performance of an isotropic fin.

At low heat transfer coefficients, the difference between the initial case and an isotropic case is only 3%, reaching up to 5% and 9% for low and high axial conductivity. The "best blocks" arrangement is nearly identical to the isotropic case. At the higher heat transfer coefficient, of $1000W/m^2K$, the differences are much more pronounced; in this case the fin conductivity is the limiting thermal resistance. The initial case is only 84% the performance of an isotropic fin, but the differences approach 25% for the low and high axial conductivity cases.

		Initial Case	**Isotropic**	**Low Axial Conductivity**	**High Axial Conductivity**	**Best Blocks**
40 W/m^2k	q (W/m)	29.1	30.1	27.5	31.5	30.4
	% Isotropic	97%	100%	91%	105%	101%
1000 W/m^2k	q (W/m)	186	222	169	282	247
	% Isotropic	84%	100%	76%	127%	111%

Table 22: Thermal Performance comparison for several anisotropy scenarios, t_f=2.5mm, H=5mm, θ_b=55K

Modeling of isotropic fins is thoroughly studied and well understood. To save time and resources, it would be preferable to approximate the thermal characteristics of an anisotropic fin with equivalent isotropic properties. At low heat transfer coefficients, where the thermal resistance in the fluid becomes a significant factor, a difference of only a few percent between the two fins makes such approximations fairly straightforward. It becomes more difficult at higher heat transfer coefficients, where the difference in performance can be greater than10%.

The thermal performance of the fin seemed to be dominated by the axial conductivity values, especially at the base of the fin. Several different methods of finding an "average" conductivity were used. A simple arithmetic mean was taken of the axial conductivities. The geometric mean, found by taking the nth root of the product of all n values, was also studied. The root mean square (RMS) was also calculated, as the square root of the sum of the squares, divided by the number of values. Finally, a harmonic mean of the axial conductivity values was used. This is the number of values divided by the sum of the reciprocal of the values, as shown in Equation (45).

$$H = \frac{n}{\frac{1}{x_1} + \frac{1}{x_2} + \frac{1}{x_3} \ldots + \frac{1}{x_n}} \tag{45}$$

This harmonic mean is frequently used in conduction problems [91] and tends to give more weight to the smaller values. This offers promise in this case as small conductivity values seem to "choke" the heat transfer rate.

As can be seen in Table 23 the performance of an isotropic fin with a conductivity set to the harmonic mean of the axial conductivity values of the initial anisotropic fin seems to most accurately represent the anisotropic fin, showing thermal performance difference of less than one percent, and less than 4% in the high heat transfer coefficient case. The geometric mean is the next best, with differences of 1.6% and 11.8% respectively.

			Isotropic			
		Anisotropic Solution	**Arithmetic Mean of k_y**	**Geometric Mean of k_y**	**RMS k_y**	**Harmonic Mean of k_y**
40 W/m^2k	q (W/m)	29.1	30.1	29.6	30.4	28.97
	Error	-	3.3%	1.6%	4.6%	0.4%
1000 W/m^2k	q (W/m)	186	222.3	208	235	193
	Error	-	19.5%	11.8%	26.5%	3.8%

Table 23: Deviation of isotropic mean conductivity performance from anisotropic performance

Thermally enhanced polymer composites provide an academically interesting heat exchanger material, due to anisotropy induced from filling characteristics. In the future, it is desirable to have manufacturing processes that facilitate the optimal alignment of fibers, to potentially achieve the high axial conductivity cases shown in Table 22. For now, simplified analysis methods, such as using a mean conductivity value, can increase the likelihood of industrial adoption of such technologies.

7.1.6.2 Heat Exchanger Module

Beyond a single fin, it is important to characterize the performance of a full heat exchanger module. The prototype heat exchanger was numerically modeled, with the model construction and strategy presented in Section 4.4. The simple model from was not sufficiently accurate for experimental considerations. The additional thermal conductance of the stainless steel thermocouples had to be accounted for, by modeling a 0.5mm cylinder with a conductivity of 14 W/mK for each thermocouple on the outside fins. The PFA-insulated thermocouples on the inside face were modeled with a conductivity of 0.5 W/mK, assuming the thick PFA-insulation dominates the thermal resistance over the very thin thermocouple wires.

The heat exchanger studied here was an assembly of several injection molded fin modules. The modules were attached to each other using a thin layer of Loctite Epoxy Gel, modeled with a thermal conductivity of 0.1 W/mK [92]. The relative impact of this thermal conductivity is studied in Figure 74. Doubling the conductivity from 0.05 W/mK to 0.1 W/mK only results in a change in heat transfer rate of 0.5%; the overall heat transfer rate is not sensitive to the epoxy thermal conductivity.

Because the flow in the short air-side heat exchanger channels is likely to be developing throughout the length, there is some uncertainty in the validity of the values used in modeling. To understand the significance of this, the effect of using a heat transfer coefficient varied by 20% is shown in Figure 75. A 20% increase in the heat transfer coefficient leads to an increase in the total heat transfer rate from 12.5W to 13.6W, or 8.2%.

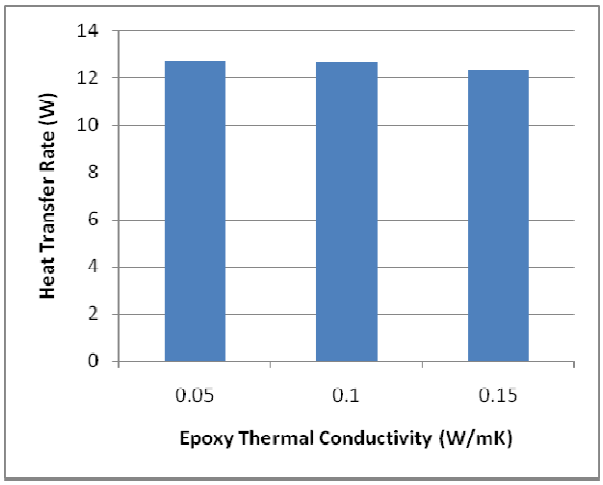

Figure 74: Effect of epoxy thermal conductivity, Q=2310 cm^3/sec

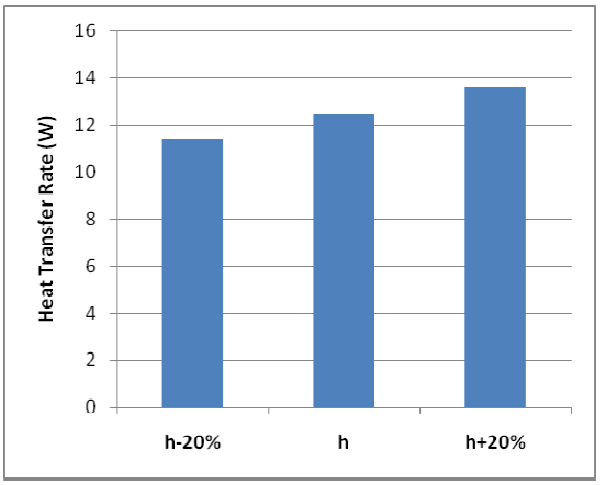

Figure 75: Effect of heat transfer coefficient, Q=2310 cm^3/sec

Another important consideration is the anisotropy which is likely present in the heat exchanger as a result of the orientation of the short carbon fibers present in the polymer matrix. As discussed earlier, these carbon fibers are the key means of enhancing the polymer's conductivity, and the directional conductivity will be significantly higher along the axis of the fibers than across them.

To study this anisotropy, the Nielsen model was used in combination with Moldflow orientation predictions, as discussed in Section 4.4, to guide the choice of conductivities. In order to most accurately compare to isotropic results, the average of the x, y, and z direction conductivities was held constant, at the isotropic value of 3.6 W/mK.

In the base, the conductivity is likely to be higher in the x and y directions, in the plane of the base, and lower in the z direction, through the thickness. This will result in a notable heat spreading behavior. A predicted anisotropy of 4.7 W/mK in the planar direction of the base is used, combined with a conductivity of 1.5W/mK through the thickness. The use of this anisotropic base conductivity, with an average isotropic fin conductivity of 3.6 W/mK, reduced the heat transfer rate from 12.49W for a purely isotropic heat exchanger module to 10.54W. An isotropic temperature profile is seen in Figure 76 for comparison. With anisotropic behavior in the base, Figure 77, significant heat spreading is observed,

with a flat temperature behavior close to the wall. The peak fin temperature is also significantly higher.

Similarly, it is also important to understand the anisotropy in the fins. This effect was studied independently from the base anisotropy. A z-direction conductivity (along the height) of 6.2 W/mK and an x and y conductivity, through the thickness and along the length, of 2.3W/mK was studied. This anisotropy had negligible effect in the overall heat transfer rate, increasing it to 12.49W from a purely isotropic heat exchanger heat transfer rate of 12.53W, or 0.3%. The temperature profile can be seen in Figure 78, showing a significant reduction in the peak temperature of the fin, from 24.3℃ to 22.3℃

Finally, the base and fin anisotropy were combined into a single model, with the values previously studied, as shown in Figure 79. The results were dominated by the effect of the base anisotropy, with the total heat transfer rate just slightly below the values found for an isotropic fin and anisotropic base, at 10.54W.

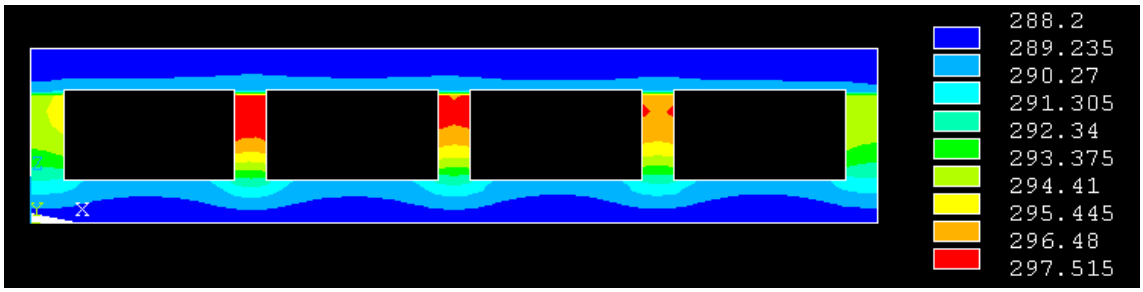

Figure 76: Isotropic HX module, k=3.6 W/mK, T_{water}=15℃, T_{air}=70℃, Q=767cm^3/s

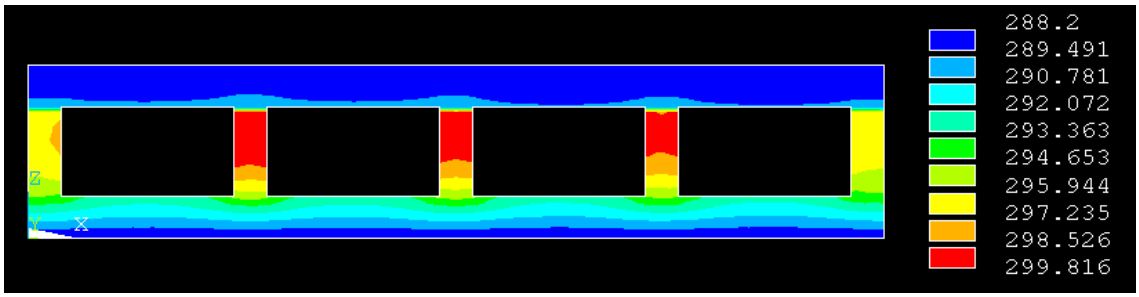

Figure 77: Anisotropic base HX module, $k_{base,x,y}$=4.7 W/mK, $k_{base,z}$=1.5 W/mK, k_{fins}=3.6 W/mK, T_{water}=15°C, T_{air}=70°C, Q=767cm^3/s

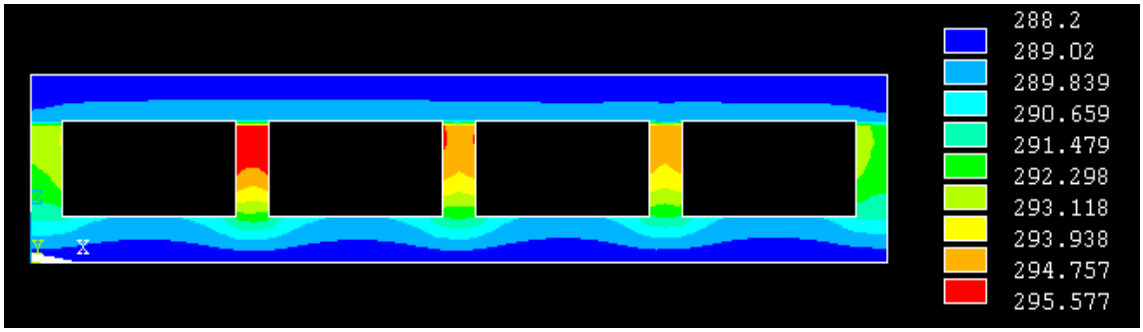

Figure 78: Anisotropic finned HX module, k_{base}=3.6 W/mK, $k_{fins,x,y}$=2.3 W/mK, $k_{fins,z}$=6.2 W/mK , Twater=15°C, Tair=70°C, Q=767cm^3/s

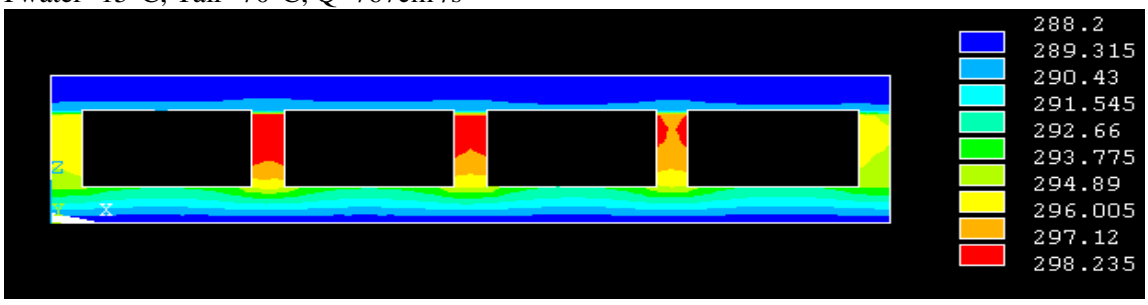

Figure 79: Combined Anisotropic fins and base HX module, $k_{base,x,y}$=4.7 W/mK, $k_{base,z}$=1.5 W/mK , $k_{fins,x,y}$=2.3 W/mK, $k_{fins,z}$=6.2 W/mK, Twater=15°C, Tair=70°C, Q=767cm3/s

7.2 Results of Thermal Performance Comparison

7.2.1 Baseline Unfilled Heat Exchanger Testing

Experimental air-side temperature drops for channel 2 and 3, the innermost channels in the middle row, of the unfilled polymer heat exchanger are plotted in Figure 80 for flowrates ranging from 1800 cm^3/sec to 3000 cm^3/sec. Predicted values are calculated based on the Sieder & Tate [93] Nusselt number correlation and the effectiveness-NTU method. Error bars are included using the 15.7% error calculated in section 7.1.5.

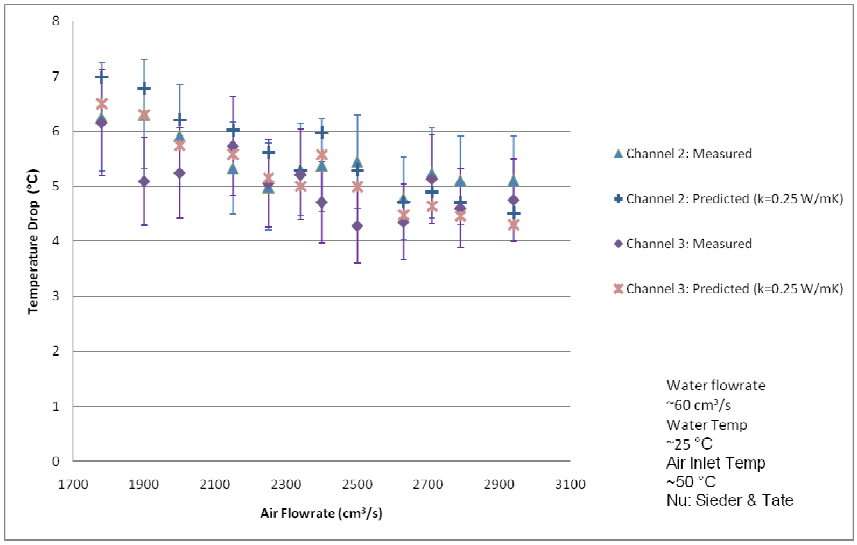

Figure 80: Air-side temperature drop over unfilled polymer heat exchanger as a function of flowrate

The air temperature drops slightly more than 6℃ at a low flowrate of 1800 cm^3/s, and about 5℃ at the higher flowrates. Measured values are well within experimental uncertainty. A slight downward trend in the temperature drop can be observed with flowrate.

7.2.2 Thermally Enhanced Polymer Heat Exchanger Testing

A heat exchanger was constructed based on PolyOne Therma-Tech [94] thermally enhanced polymer, with specified nominal thermal conductivity of 10 W/mK. Dimensions were identical to that of the unfilled polymer heat exchanger, as discussed in 7.1.1.

Results show air temperature drops ranging from nearly 10℃ to about 8℃ at the highest flowrates. 15.7% error bars are again shown in the chart. The standard deviation and mean of the residuals, as well as the standard error, are displayed in Table 24. Thermal conductivity testing was done on samples of the polymer and gave values of approximately 4.0 W/mK much lower than the nominal value given by the manufacturer. This is likely due to the fiber orientation in the test samples.

k=4.0 W/mK	**Channel 2**	**Channel 3**
Std Dev of Residual	0.519	0.499
Mean of Residuals	-0.087	-0.167
Std Err	0.555	0.558

Table 24: Statistical analysis of thermally enhanced HX data

The standard error is calculated according to equation (46), where Y is the measured value and $\hat{Y}$ the predicted value [95].

$$Standard\ Error = \sqrt{\sum \frac{\left[Y - \hat{Y}(X)\right]^2}{n-2}} \quad \textbf{(46)}$$

To calculate the predicted values, an equation was analytically derived for the air temperature drop over the prototypical heat exchanger as a function of air flowrate, based upon the effectiveness-NTU equation

$$\Delta T = 78 - 78\exp\left(\frac{117.4}{456.02Q} NTU^{0.22}\left\{\exp\left(-\frac{456.02Q}{177.4} NTU^{0.78}\right) - 1\right\}\right) \quad \textbf{(47)}$$

where NTU is specified as the following:

$$NTU = \left(\frac{UA}{456.02Q}\right) \quad \textbf{(48)}$$

For a thermal conductivity of 4.0 W/mK, the UA term is approximated by the following:

$$\left(\frac{1}{21.921Q + 0.1043} + 1.669\right)^{-1} \quad \textbf{(49)}$$

This relation is within 0.25% of the UA determined using the Sieder & Tate Nusselt number correlation, and is valid only for this heat exchanger with a fin thickness of 2.5mm, height of 5mm, a total width of 50mm, and a nominal thermal conductivity of 4.0 W/mK. Sieder and Tate is an appropriate Nusselt number correlation for this case, as Reynolds numbers are laminar, ranging from 1000-1500 for air and about 1000 for water, and the flow is simultaneously developing. This correlation is generally considered to be valid for values of $[RePr/(L/D)]^{1/3}(\mu/\mu_s)^{0.14} > 2$. In this case, values of this quantity are in the range of 4 to 6.

Due to the relatively thick fins in use here, fin efficiencies are high, from 91-93% across the range studied, one benefit from the constraints of the injections molding process.

To gauge the accuracy of the predicted air-side temperature drops, the predicted values were plotted against the measured values in Figure 81.

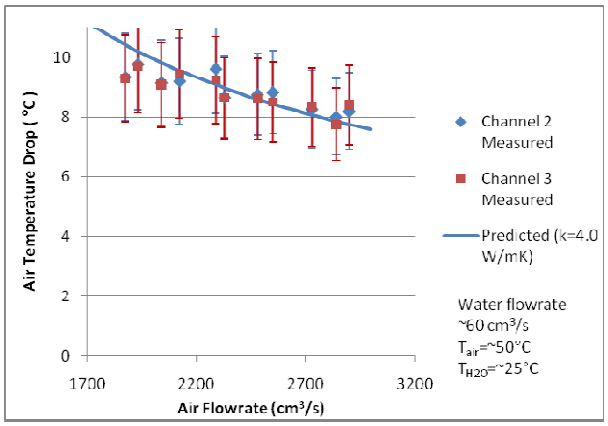

Figure 81: Air-side temperature drop over thermally enhanced polymer heat exchanger as a function of flowrate

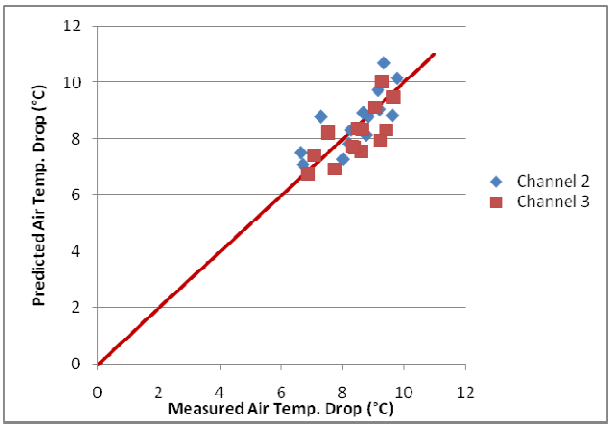

Figure 82: Predicted vs. Measured Air Temperature Drop in Thermally-Enhanced HX

The mean residual is -0.190 and 0.322 for channel 2 and 3, with a standard deviation of 0.722 and 0.644. The relative standard deviation, the standard deviation divided by the mean air temperature drop, is 8.64% for channel 2 and 7.62% for channel 3, within experimental uncertainty.

Another method of verification is heat balance. The heat lost by the air should be equivalent to the heat gained by the water, according to equation (50).

It was not possible to do this for the unfilled polymer, as the increase in the water temperature was too small to measure. With the use of a thermally enhanced polymer, heat transfer was increased, and the water temperature delta increased accordingly. Results are tabulated for a full range of air flowrates from 1875 cm^3/s to 2940 cm^3/s, see Table 25.

(50)

Air Flowrate (cm^3/s)	**H_2O Flowrate (cm^3/s)**	**Air DeltaT (K)**	**Water DeltaT (K)**	**Air Heat (W)**	**Water Heat (W)**	**% Error**
1875	62.4	9.34	0.069	20.06	17.97	11.66%
1933	66.0	9.77	0.088	21.64	24.16	10.43%
2040	64.4	9.15	0.121	21.39	32.52	34.24%
2124	65.0	9.20	0.060	22.39	16.28	37.55%
2260	61.4	7.28	0.089	18.85	22.81	17.35%
2290	65.5	9.62	0.087	25.24	23.78	6.13%
2330	62.4	8.67	0.078	23.14	20.31	13.94%
2480	61.4	8.76	0.099	24.89	25.37	1.89%
2550	65.5	8.83	0.105	25.80	28.76	10.29%
2600	67.5	9.38	0.087	27.94	24.48	14.14%
2660	62.0	6.63	0.081	20.21	20.93	3.47%
2730	63.3	8.26	0.095	25.84	25.18	2.62%
2820	67.5	9.13	0.109	29.50	30.71	3.93%
2840	64.4	8.01	0.091	26.06	24.38	6.91%
2900	64.0	8.19	0.104	27.21	27.78	2.04%
2940	60.6	6.70	0.077	22.57	19.40	16.34%
					Average	**12.06%**

Table 25: Experimental Heat Balance of Heat Exchanger Heat Transfer Paths.

The average heat balance error of 12% is well within experimental uncertainty for such a minute water-side temperature rise. There is a high degree of uncertainty in this comparison, because of the small temperature difference. These heat balance results serve only as a check on the air side results.

The observed air-side temperature drops seen in the thermally enhanced polymer heat exchanger were a significant improvement over the unfilled polymer heat exchanger. A comparison between the two can be seen in Figure 83.

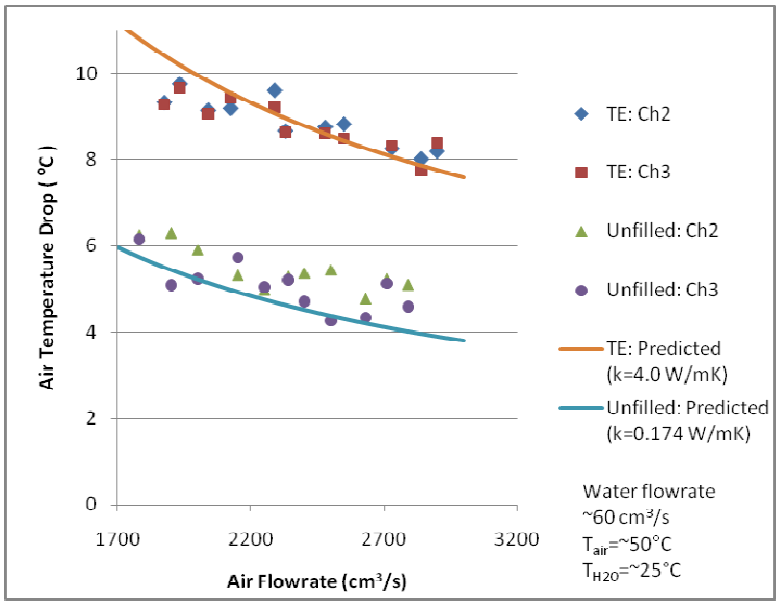

Figure 83: Comparison of air temperature drop between unfilled and thermally enhanced heat exchangers

Both conductivity values used for predictions were determined experimentally. The predictions for the unfilled polymer heat exchanger seem to underpredict the measured values, likely due to anisotropy introduced in the FDM manufacturing process of the heat exchanger. Notable, the thermally enhanced heat exchanger offers an approximate 70% performance advantage over the unfilled polymer heat exchanger, throughout the range of flowrates.

7.3 Results of Temperature Distribution in Polymer HX Fins

The temperature distribution over the fins was measured for several cases; comparisons for the low flowrate case of 1625 cm^3/sec are shown in Figures 84-86. The measured values, on the left hand side, are shown superimposed over an image of the fin, with corresponding numerical predictions shown on the right hand side. The fin locations, one for the inlet side and two on the outlet side, correspond to the heat exchanger diagram in Figure 60.

In this case, the conductivity values predicted by the Nielsen equation were used, without concern for maintaining a constant "average" conductivity. In the base, the conductivity

is likely to be higher in the x and y directions, but lower than previously studied, due to less orientation at the base of the fin. Based on Moldflow simulations, in combination with the Nielsen model, a planar conductivity of 4W/mK is predicted, combined with a conductivity of 1.5W/mK through the thickness. There is also likely to be anisotropy in the fins as well, but averaging 15 points within the fin leads to a constant value of 3.6 W/mK. This is because of the larger x-direction orientation at the base and top, contrasting with the large y-orientation in the middle of the fin.

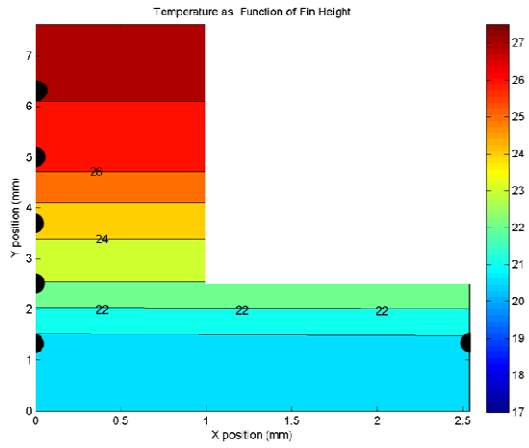

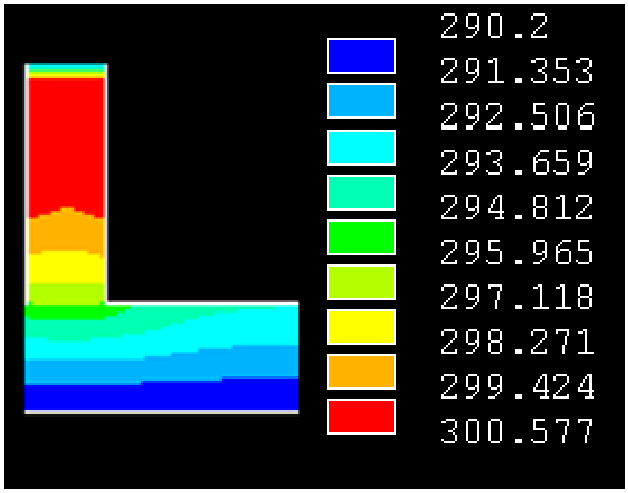

27.1	
26.6	
24.5	
23.0	
20.5	20.6

(a) Measured

27.3	
26.3	
25	
22.8	
20.5	20.5

(b) Predicted (k_{fin}=3.6 W/mK, $k_{base,x,y}$=4 W/mK, $k_{base,z}$=1.5 W/mK)

Figure 84: Measured vs. Predicted temperature distribution over inlet fin, Q=1625 cm^3/sec

The inlet temperatures show good overall agreement, with a maximum error of 0.5℃. Values for the outlet side, both left and right fins, are presented below. The air going into left side was several degrees warmer than the air going into the right side, which explains the difference in the two temperature distributions.

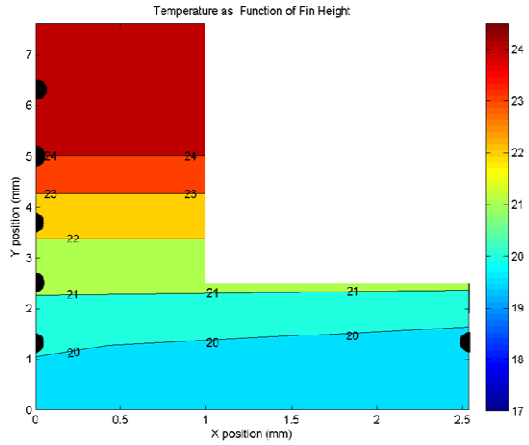

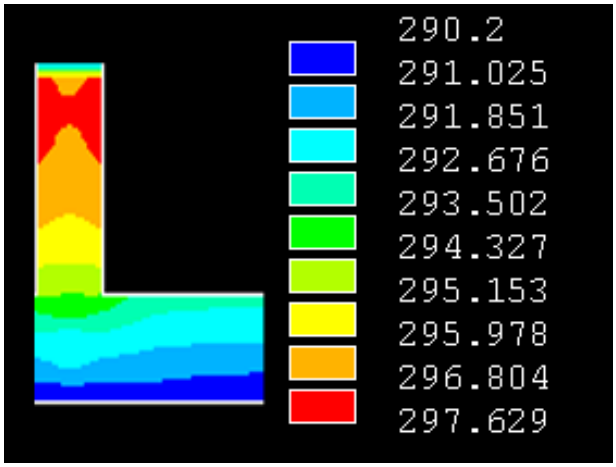

24.6	
24.0	
22.4	
21.7	
20.1	19.2

(a) Measured

24.2	
23.5	
22.7	
21.2	
19.6	19.1

(b) Predicted (k_{fin}=3.6 W/mK, $k_{base,x,y}$=4 W/mK, $k_{base,z}$=1.5 W/mK)

Figure 85: Measured vs. Predicted temperature distribution over left outlet fin, Q=1625 cm^3/sec

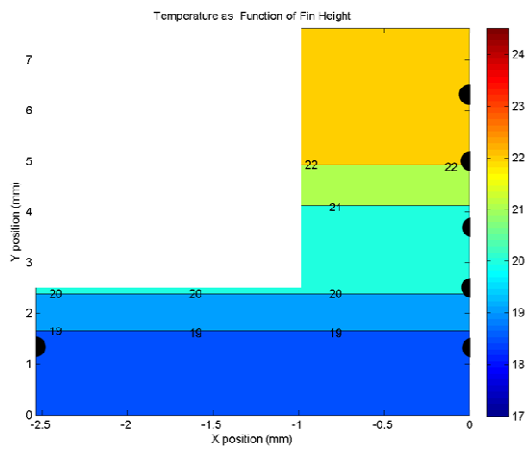

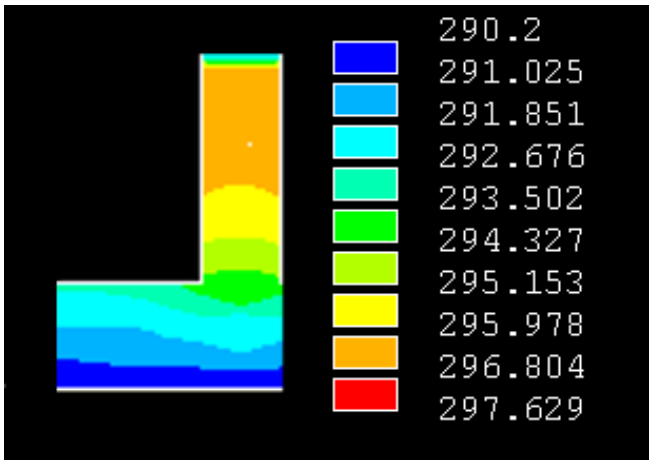

	22.3
	22.2
	20.6
	20.2
18.5	18.8

(a) Measured

	22.8
	22.7
	21.6
	20.5
18.4	18.7

(b) Predicted (k_{fin}=3.6 W/mK, $k_{base,x,y}$=4 W/mK, $k_{base,z}$=1.5 W/mK)

Figure 86: Measured vs. Predicted temperature distribution over right outlet fin, Q=1625 cm^3/sec

Accuracy is still good on the outlet side, with the maximum discrepancy on the left side being 0.5°C, while the right side has a more rapid temperature drop in the middle of the fin than expected, leading to a discrepancy of up to one degree. This may be explained by the somewhat random nature of the fiber orientation in the fins; a higher local thermal conductivity would lead to a larger temperature drop.

The statistical value of the error between the measured and simulated values combined for all three fins is shown in Table 26. The low mean of residuals shows that the errors involved are primarily random, not systematic. The distribution has a standard deviation of 0.432 and a standard error of estimate of 0.411.

Std. Dev	0.432
Mean of Residuals	0.0577
Std. Error of Estimate	0.411

Table 26: Statistical error in temperature distribution

To further verify the results, the measured heat transfer rate can be compared to the predicted heat transfer rate. Results are shown for several flowrates (Figure 87), and compared to the anisotropic conductivities used to compare the temperature distribution. In the low flow case, experimental results are less than the heat transfer rate predicted by ANSYS by about 5%, 8.65W as compared to 9.04W. The error is slightly less in the high flow case, 3%, but in this case ANSYS underpredicts the heat transfer rate, 10.73W as compared to 10.23W. These errors are well within experimental uncertainty. An isotropic conductivity of 3.6 W/mK is also shown for reference.

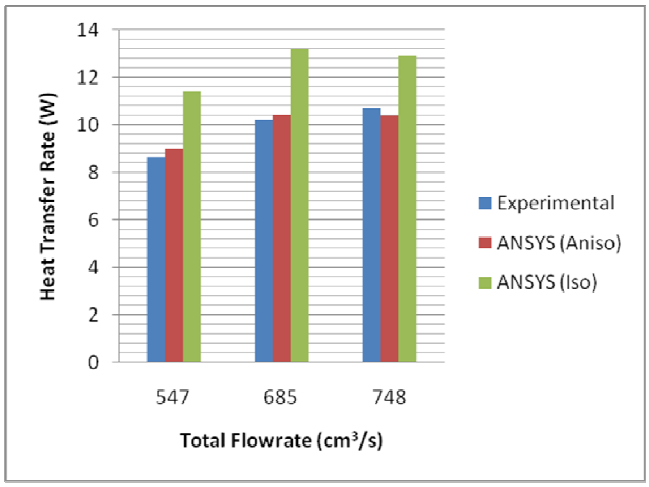

Figure 87: Comparison of measured and predicted heat transfer rates for several flowrates, T_{water}=15°C, T_{air}=70°C

Determining an "equivalent" isotropic thermal conductivity is useful in understanding the net performance of the heat exchanger module. Figure 88 shows a comparison of the heat transfer rate for several isotropic conductivities to both the experimental and anisotropic values given in Figure 87, for a flowrate of 685 cm^3/s. While the isotropic value of 3.6

W/mK significantly overpredicts the heat transfer rate, 13.2W compared to 10.2, an isotropic value of 2.5 W/mK can be seen to closely approximate both the modeled anisotropic results and the experimental results. While this is significantly lower than the manufacturer's listed conductivity of 10 W/mK, it is still an order of magnitude greater than the base polymer. For reference, the heat transfer rate for an unfilled, 0.25 W/mK polymer is plotted, at only 3.7W, or 35% of the experimental performance.

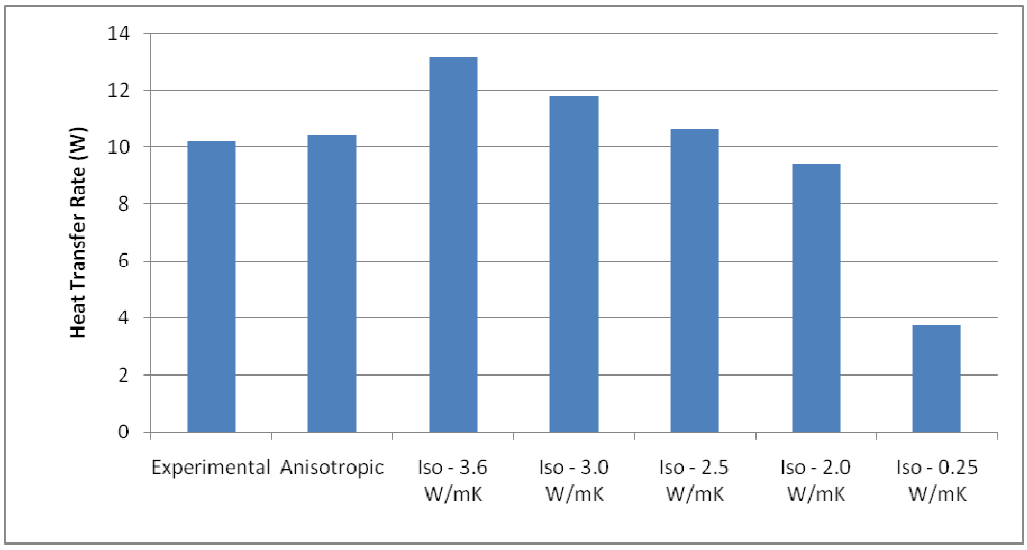

Figure 88: Comparison of heat transfer for several isotropic conductivities, T_{water}=15°C, T_{air}=70°C, Q=685 cm^3/s.

An anisotropic set of conductivities suggested by the Nielsen equation, was used to match the temperature distribution. An effective isotropic conductivity of 2.5 W/mK was then determined. On top of these two, a further investigation into an anisotropic conductivity that matches both the temperature distribution and the heat transfer rate can be conducted. For the case shown in Figures 84-86, numerical analysis overpredicts the heat transfer rate, 9.1W as compared to an experimental value of 8.6W. Through a trial-and-error process, a set of conductivities were found that match this experimental heat transfer rate, and still give good agreement with the temperature distribution. Initially, the base thickness was set at 4W/mK in the planar direction, and 1.5W/mK through the thickness. To match the heat transfer rate, this was reduced to 3W/mK in the planar direction, and increased to 1.6W/mK in the planar direction. The fin conductivity, initially an isotropic

3.6W/mK, was reduced to 3.0W/mK. The final temperature distribution can be seen in Figure 89, and falls within 0.1℃ of the temperatures previously found.

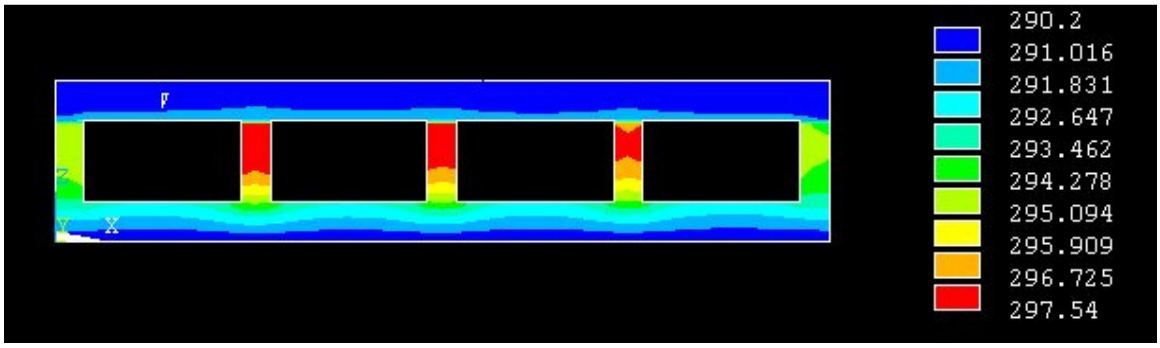

Figure 89: Predicted outlet temperature distribution matching experimental heat transfer rate, Q=1625 cm^3/sec, k_{fin}=3.0 W/mK, $k_{base,x,y}$=3 W/mK, $k_{base,z}$=1.6 W/mK

Numerical results appear to be able to accurately predict the temperature profile in fins, and pinpoint the causes of non-uniform temperature distributions; primarily the epoxy layer required for assembling and the anisotropy effects in the base. Numerical results also accurately reflect the heat transfer rate of the heat exchanger module.

Parametric numerical comparisons would seem to encourage manufacturing techniques that avoid the use of epoxy for assembly. This is possible using currently injection molding techniques, but prohibitively costly for small runs.

Chapter 8: Summary of Contributions and Future Work

8.1 Summary of Contributions

Polymer heat exchangers have the potential to play an important role in the use of corrosive fluids for cooling. From power plants to industrial cooling, freshwater consumption can be minimized through the use of heat exchangers able to withstand seawater, greywater, and brackish water for extended periods of time.

The energy content of polymers was studied and compared to several existing heat exchanger materials, through the use of life cycle studies and performance modeling. A composite energy content for thermally enhanced polymer composites was developed based on the Nielsen model. This energy content proved to be several times less than that of titanium. While larger than the raw energy content of copper, the low density of the polymers means an equivalent heat exchanger will weigh less, and have less overall invested energy. Thermally enhanced polymers provide the interesting opportunity of optimizing thermal conductivity for the specific application, as both the energy content and conductivity is dominated by the carbon fiber fillers used.

The array-based least material relation was shown to predict the mass-based optimum least material efficiency to within 1.5% for a thermal conductivity of k=5 W/mK and 5.1% at k=10 W/mK, relevant values for future use of thermally-enhanced polymers. While the low energy content of the unfilled polymer is attractive, the low conductivity of 0.25 W/mK may hamper performance too much for industrial applications. Error at low fin spacings and thermal conductivities can be reduced through a combination of an array-based least material relation and use of the full fin efficiency equations. Thermally-enhanced polymers show a strong balance of thermal performance and energy content in gas-cooled fins

For polymer composites, significant orthotropic behavior is introduced by the directional carbon fibers. Numerical analysis of the differences in the thermal performance of

anisotropic and isotropic fins was small – 3% – for a low heat transfer coefficient, but the difference was much larger – 16% – at high heat transfer coefficients. If the directional conductivities can be identified at several locations throughout the sample, it was shown that by taking the harmonic mean of the axial conductivities values, an effective isotropic conductivity can be developed to simplify thermal analysis.

Several heat exchanger thermal analysis metrics were reviewed. The effectiveness-NTU relations were used for determining performance. For gas-liquid applications, the thermal resistance was found to be dominated by the gas, even for low thermal conductivities. This motivated the focus of optimization efforts on enhancement on the gas side. For a reference heat exchanger module of 1m on a side, the flow was shown to be predominantly fully developed, simplifying thermal analysis. The total coefficient of performance was introduced as a metric accounting for the heat transfer rate as a function of both the energy invested in pumping and in formation/fabrication.

A parametric study of several corrosion resistant materials was conducted, for a methane-seawater heat exchanger module. Unfilled polymers were found to perform poorly compared to their thermally-enhanced counterparts. Even small conductivity enhancements, up to 5 W/mK, were show to be sufficient to approximate performance of current corrosion resistant metals. Furthermore, such polymer composites showed COP_T values 48% better than an optimized aluminum heat exchanger, and nearly 7 times better than a titanium heat exchanger.

Several alternative heat exchanger geometries were studied, comparing the finned plate heat exchanger comprising the focus of this thesis to a more conventional shell and tube heat exchanger, as well as an alternative plate coil heat exchanger. The finned plate geometry showed superior performance compared to manufacturable shell and tube and plate coil configurations. The performance of the plate coil was severely limited due to constraints imposed by the injection molding process. Mass and volume specific metrics for the finned plate were seen to be nearly 5 times greater than a shell and tube

configuration, due to the large enclosed volume and required heat transfer area for a shell and tube.

The least material relations studied previously for single fins were demonstrated to be applicable to full heat exchanger design. Fins can be designed to achieve nearly equivalent heat transfer to a nominal fin, but with far less mass. This is a conclusion that is relevant not only to thermally-enhanced polymers, but conventional materials as well. Significant energy savings can be realized in formation, fabrication, and transportation of heat exchangers designed for minimum mass.

Finally, it was experimentally determined that a thermally enhanced polymer can be injection molded and assembled into a heat exchanger, and deliver thermal performance in excess of 70% greater than that of a reference unfilled polymer heat exchanger. The results were shown to correlate well to the results of the effectiveness-NTU relations discussed earlier. A heat balance was used for further verification of the results. The temperature distribution within the fins was studied using finite element methods, and verified experimentally. Numerical results appear to be able to accurately predict the temperature profile in fins, and pinpoint the causes of non-uniform temperature distributions; primarily the epoxy layer required for assembling and the anisotropy effects in the base. Numerical results also accurately reflect the heat transfer rate of the heat exchanger module.

8.2 Future Work

Verification of corrosion-resistance: Unfilled polymers have been used in seawater applications for some time, and proven to be resistant to the detrimental effects of corrosion and scaling. Carbon fiber fillers may be more susceptible to corrosion and scaling, reducing thermal performance or showing signs of pitting. It is crucial to demonstrate that mixing of fluids will not be a concern, and polymer composites can withstand high temperature, high salinity seawater for months or years.

Mechanical strength: Mechanical properties of carbon filled polymer composites are far superior to those of unfilled composites. It is important to understand how the directionality of these fibers affects the strength of the polymers. Fins thicker than those conventionally used for titanium are likely to be necessary, due to inferior mechanical properties. Additional work should seek to balance the thermal and structural requirements of polymer composite fins.

Large scale demonstration: A small scale heat exchanger was developed here, and demonstrated significantly improved performance. This is likely to scale up well, but to convince commercial industries to adopt this new technology, a larger prototype must be developed, capable of industrial heat transfer rates in the hundreds of kilowatts.

Appendix 1: Labview Configuration - Front Panel

The Labview code front panel is presented in Figure a.1, for corresponding block diagram presented in figure 68.b.

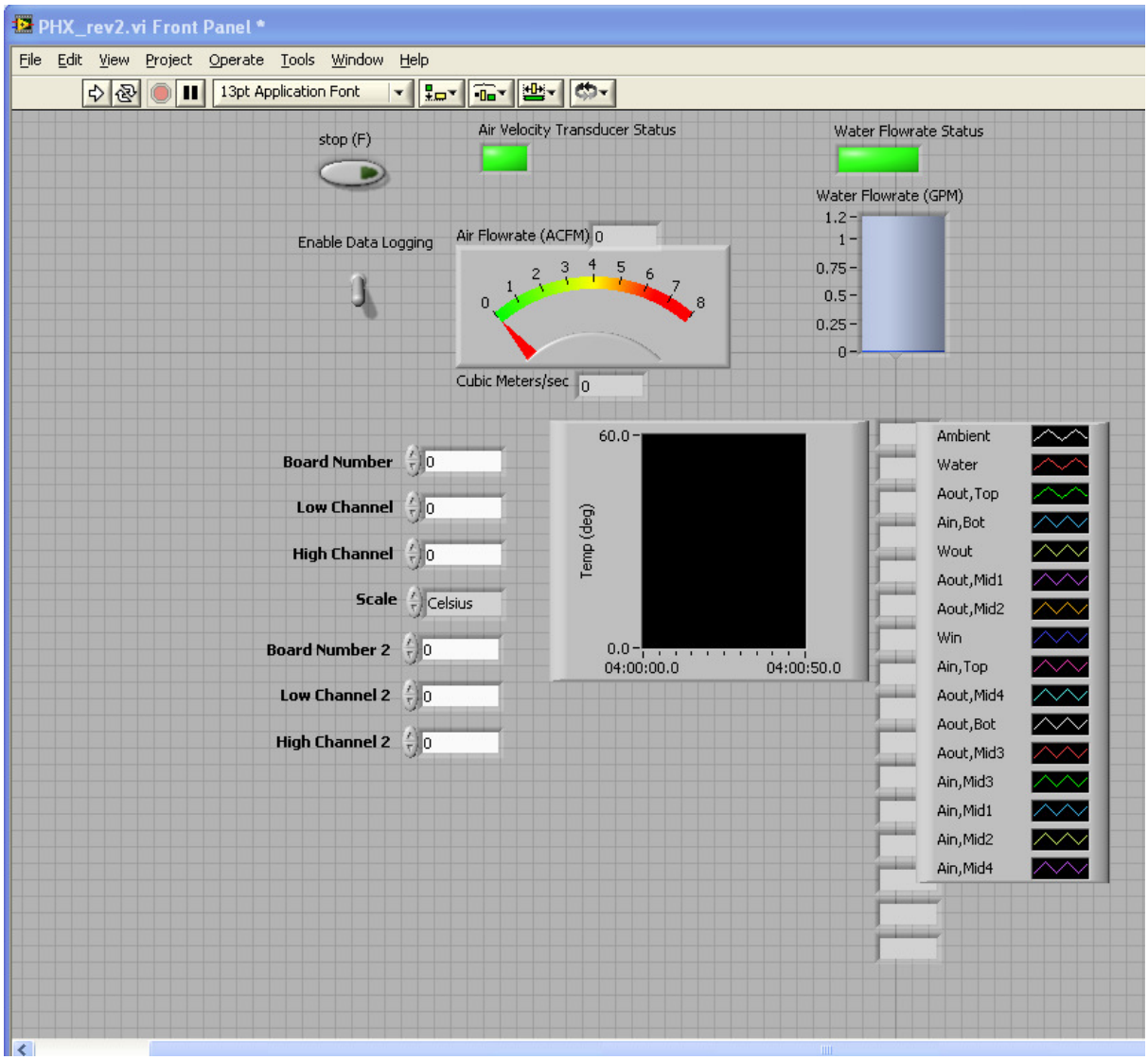

Figure a.1: Front panel for Labview data acquisition system

Appendix 2: ANSYS Code

The ANSYS code used for anisotropic simulations of the heat exchanger module, as discussed in Section 4.4, is presented below.

```
/clear

W=.05
L=.05
H=.005
N=5
tb=.0025
tf=.0020
S=(W-tf)/(N-1)-tf
h_airi=38.4
tamb_L=343
Tamb_LL=334
tamb_RR=338
tamb_R=340
twater=285.5
grad_L=-236
grad_LL=-313
grad_RR=-333
grad_R=-226
te=.0003
tinlet=323
h_air=h_airi+0*h_airi
kepoxy=.1-0*.1

/prep7
/title,Plate Fin Array

!---- Element Types
ET,1,SOLID70

!---- Geometry
BLOCK,0,W,0,L,0,tb
BLOCK,0,tf,0,L,tb,tb+H
BLOCK,0,tf,0,L,tb+H,tb+H+te
BLOCK,0,W,0,L,tb+H+te,2*tb+H+te
vsel,,VOLU,,2,3
vgen,N,ALL,,,S+tf,
vsel,all
vglue,all
K,1000,0,L,0
K,1001,W/2,L,0
K,1002,0,L,tb/2
KWPLAN,1,1000,1001,1002
CYL4,S+1.5*tf,tb/2,.0005,,,,.01
vsel,,VOLU,,1
vgen,5,ALL,,,,,.00127
CYL4,S+1.5*tf+.00254,tb/2,.0005,,,,.01
vsel,all
```

```
CYL4,3*(S+tf)+tf/2,tb/2,.0005,,,,.01
vsel,,VOLU,,10
vgen,5,ALL,,,,,.00127
CYL4,3*(S+tf)+tf/2-.00254,tb/2,.0005,,,,.01
K,1003,0,0,0
K,1004,W/2,0,0
K,1005,0,0,tb/2
KWPLAN,1,1003,1004,1005
CYL4,S+1.5*tf,tb/2,.0005,,,,-.01
vsel,,VOLU,,25
vgen,5,ALL,,,,,.00127
CYL4,S+1.5*tf+.00254,tb/2,.0005,,,,-.01
vsel,all
vsel,all
VOVLAP,all

!-----Material Properties
mp,KXX,1,3.6
mp,KYY,1,3.6
mp,KZZ,1,3.6
mp,KXX,2,kepoxy
mp,KYY,2,kepoxy
mp,KZZ,2,kepoxy
mp,KXX,3,14
mp,KYY,3,14
mp,KZZ,3,14
mp,KXX,4,.5
mp,KYY,4,.5
mp,KZZ,4,.5
mp,KXX,5,4
mp,KYY,5,4
mp,KZZ,5,1.5
mp,KXX,6,2.6
mp,KYY,6,2.6
mp,KZZ,6,4.3

!-----Mesh polymer, epoxy, and thermocouple volumes
!---large elements for most of polymer
vsel,all
MSHKEY,0
MSHAPE,1
MAT,1
esize,0.001
SHPP,Silent,ON
vmesh,21

!---Anisotropic Fins
vsel,all
MSHKEY,0
MSHAPE,1
MAT,6
esize,0.001
vmesh,7
vmesh,13
vmesh,18
```

```
!--small elements where polymer meets TC's, anisotropic fins
MSHKEY,0
MSHAPE,1
MAT,6
SMRTSIZE,4
vmesh,37,38

!--Anistropy in base plate
MSHKEY,0
MSHAPE,1
MAT,5
SMRTSIZE,4
vmesh,39

!---Epoxy
MSHKEY,0
MSHAPE,1
MAT,2
SMRTSIZE,3
vmesh,14,17
vmesh,19

!---Outlet TC
MSHKEY,0
MSHAPE,1
MAT,3
SMRTSIZE,3
vmesh,1,4
vmesh,6,12,2
vmesh,22,24
vmesh,31,32
vmesh,34,35

!---Inlet TC
MSHKEY,0
MSHAPE,1
MAT,4
SMRTSIZE,3
vmesh,25,30
vmesh,33
vmesh,36

!-----Apply Loads
SFGRAD,CONV,0,Y,0,grad_L
ASEL,S,AREA,,12
ASEL,A,AREA,,78
ASEL,A,AREA,,108
ASEL,A,AREA,,102
ASEL,A,AREA,,84
ASEL,A,AREA,,29
sfa,all,,conv,h_air,tamb_L

SFGRAD,CONV,0,Y,0,grad_LL
ASEL,s,AREA,,82
ASEL,A,AREA,,41
ASEL,A,AREA,,88
```

```
ASEL,A,AREA,,30
ASEL,A,AREA,,110
ASEL,A,AREA,,103
sfa,all,,conv,h_air,tamb_LL

ASEL,ALL
SFGRAD,CONV,0,Y,0,grad_R
ASEL,S,AREA,,42
ASEL,A,AREA,,86
ASEL,A,AREA,,111
ASEL,A,AREA,,104
ASEL,A,AREA,,53
ASEL,A,AREA,,92
sfa,all,,conv,h_air,tamb_R

SFGRAD,CONV,0,Y,0,grad_RR
ASEL,s,AREA,,54
ASEL,A,AREA,,90
ASEL,A,AREA,,65
ASEL,A,AREA,,101
ASEL,A,AREA,,105
ASEL,A,AREA,,112
sfa,all,,conv,h_air,tamb_R

ASEL,ALL
ASEL,S,AREA,,1
ASEL,A,AREA,,20
DA,ALL,TEMP,twater
Asel,s,area,,113
Asel,a,area,,174
Asel,a,area,,75
Asel,a,area,,81
Asel,a,area,,85
Asel,a,area,,89
Asel,a,area,,39
Asel,a,area,,51
Asel,a,area,,95
Asel,a,area,,113
asel,a,area,,175
asel,a,area,,77
asel,a,area,,99
DA,ALL,TEMP,tinlet
ASEL,ALL

!-----Solution
/solu
antype,static
solve

!---Temperature Plot
/post1
plnsol,temp

/plopts,info,auto
/plopts,logo,off
/plopts,frame,off
```

```
NSEL,S,LOC,Z,0            ! SELECT NODES AT Base of fin
NSEL,a,LOC,Z,2*tb+tf+te
FSUM, HEAT

wpoff,,,-.011
sucreate,inlet,cplane
susel,s,inlet
sumap,inletT,temp
suplot,inlet,inletT

/image,save,031109_1TC_inlet_anisocombined,jpg

wpoff,,,-.019
sucreate,inlet,cplane
susel,s,inlet
sumap,inletT,temp
suplot,inlet,inletT

/image,save,031109_1TC_outlet_anisocombined,jpg
finish
```

Appendix 3: Temperature Traverse of Test Facility

The results of a temperature traverse, performed 9cm before the inlet of the heat exchanger, both in the vertical and horizontal directions, are presented in figures a.2 to a.5.

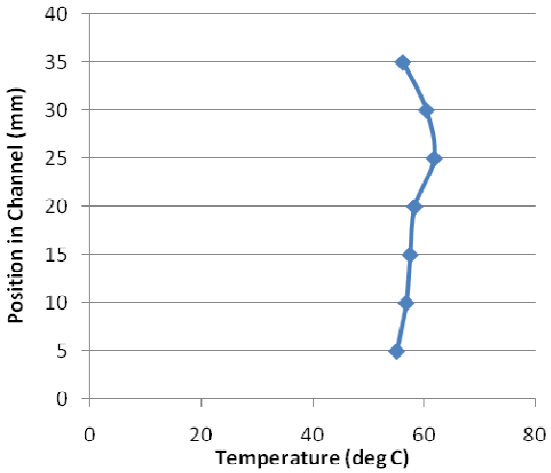

Fig a.2: Vertical temperature traverse of experimental facility, Q=1800cm^3/s

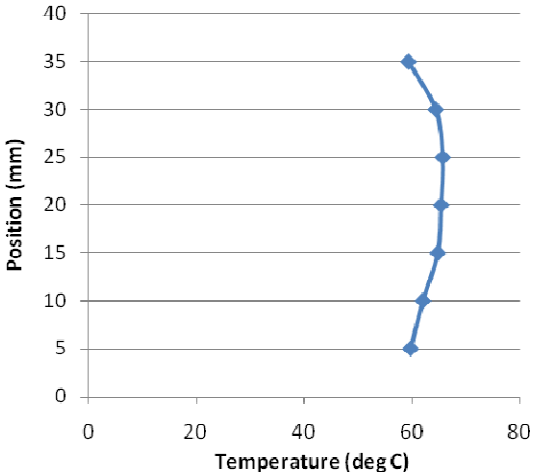

Fig a.3: Vertical temperature traverse of experimental facility, Q=3000cm^3/s

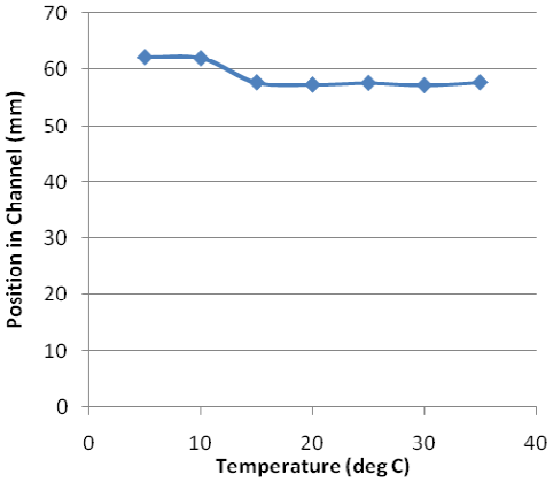

Fig a.4: Horizontal temperature traverse of experimental facility, Q=1800cm^3/s

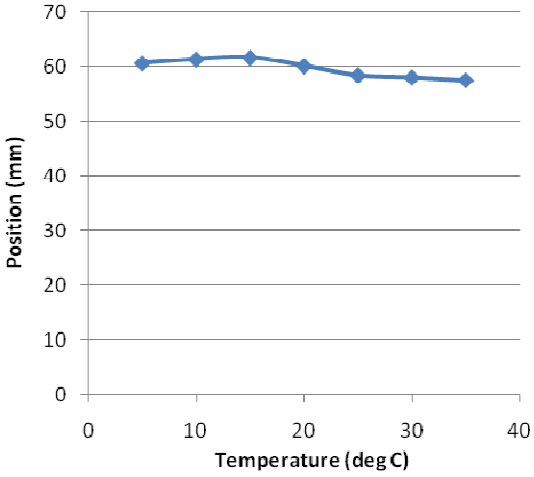

Fig a.5: Horizontal temperature traverse of experimental facility, Q=3000cm^3/s

The significant variations seen in this temperature traverse, especially in the vertical direction, motivated further study. A temperature traverse at the inlet of the heat exchanger is compared to a "middle" traverse 9cm upstream of the heat exchanger, as well as to an inlet traverse immediately following the heater, 89cm upstream of the heat exchanger. It can be seen in Figure a.6 that what appears to be a very significant temperature gradient at the inlet of nearly 8℃ lessens significantly over the length of the channel, down to 4℃ at the later measurement point, and about 1.5℃ at the heat exchanger inlet.

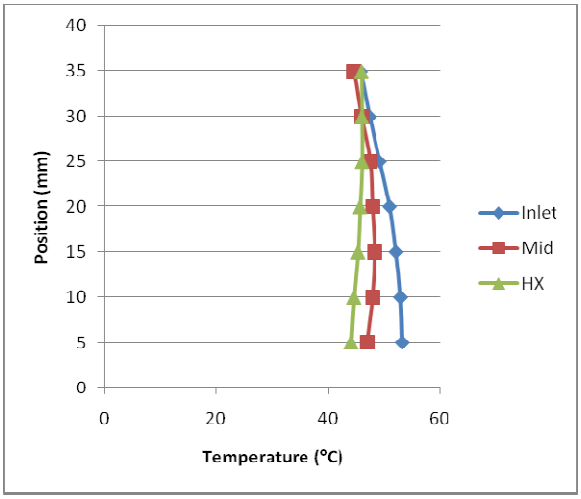

Figure a.6: Temperature traverse of test facility at several locations, q=3000 cm3/s

Despite the relatively minor stratification of the flow, calculations for the heat transfer rate throughout the experimental study were done by taking the temperature at the inlet to each individual channel, not a single overall temperature. This should reduce most of the error caused by the temperature stratification.

The average of the inlet temperatures can also be taken, and results in an overall calculated heat transfer rate very close to the value obtained from taking into account the individual temperature differences, as seen in Figure a.7.

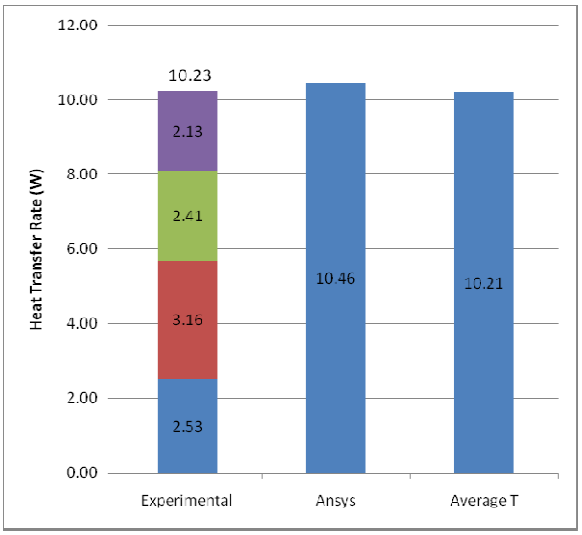

Figure a.7: Heat transfer rate comparison of experimental, Ansys and average cases. T_{air}~70℃, T_{water}=20℃, Q=2086 cm^3/s

Bibliography

[1]Sims, R.E.H., et al., *Energy Supply*. *Climate Change 2007: Mitigation. Contribution of Working Group III to the Fourth Assessment Report of the Intergovernmental Panel on Climate Change*, ed. O.R. Davidson, et al., Cambridge, United Kingdom and New York, NY, USA.

[2]Bar-Cohen, A., P. Rodgers, and J. Cevallos, *Application of Thermally Conductive Thermoplastics to Seawater-cooled Liquid-Liquid Heat Exchangers*, in *Fifth European Thermal-Sciences Conference*. 2008: Eindhoven, The Netherlands.

[3]Kampf, J. and M. Sadrinasab, *The circulation of the Persian gulf: a numerical study.* Ocean Science, 2006. **2**: p. 27-41.

[4]ADGAS, *Third LNG Train Project Das Island, Regenerator Overhead Condensor*. 1991: Drawing Number: D02-E3-DS-007.

[5]*International Energy Outlook 2008*. Energy Information Administration June 2008.; Available from: http://www.eia.doe.gov/oiaf/ieo/index.html.

[6]*Natural Gas Background*. 2004 [cited 2008 February 13th]; Available from: http://www.naturalgas.org/overview/background.asp.

[7]Millero, F.J., et al., *The composition of Standard Seawater and the definition of the Reference-Composition Salinity Scale.* Deep Sea Research Part I: Oceanographic Research Papers, 2008. **55**(1): p. 50-72.

[8]*Personnel communication with Mr. Nashaat M. Mohamed, ADGAS*. July 2007.

[9]Haytoumi, N. and P. Rodgers, *Survey of Heat Exchanger Usage at ADGAS Das Island LNG Plant*. 2008.

[10]*Case study Heat Exchanger 2-E-205B Hot Carbonate Titanium Tube Failure*, ADGAS Corrosion and Inspection Department.

[11]Wang, L., B. Sundén, and R.M. Manglik, *Plate Heat Exchangers: Design, Applications and Performance*. 2007, Billerica, MA: WIT Press.

[12]McCue, D.M. and D.K. Peacock, *The Application of Titanium for Power Plant Surface Condensers.* EPRI.

[13]Hart, G.K., C.-O. Lee, and S.R. Latour, *Development of Plastic Heat Exchangers for Ocean Thermal Energy Conversion*, in *Technical Report ORO-5165-1*. 1979, DSS Engineers, Inc.: Fort Lauderdale, FL.

[14]Zaheed, L. and R.J.J. Jachuck, *Review of polymer compact heat exchangers, with special emphasis on a polymer film unit.* Applied Thermal Engineering, 2004. **24**(16): p. 2323-2358.

[15]Hutson, S., et al., *Estimated Use of Water in the United States in 2000.* U.S. Geological Survey Circular 1268, 2000.

[16]Solley, W.B., C.F. Merk, and R.R. Pierce, *Estimated use of water in the United States in 1985.* US Geological Survey Circular 1004, 1988: p. 82.

[17]*Cooling Power Plants*. Nov 2008 [cited 2009 Jan 29]; Available from: http://www.world-nuclear.org/info/cooling_power_plants_inf121.html.

[18]Kampe, S.L. *Incorporating Green Engineering in Materials Selection and Design*. in *Proceedings of the 2001 Green Engineering Conference: Sustainable and Environmentally-Conscious Engineering*. 2001. Roanoke, VA.
[19]Shindo, N., *Energy and Environmental Applications of Carbon Materials*, in *The Research Council for Energy and Information Technology Magazine*. 2002: Tokyo, Japan.
[20]*Summary of Inventory Data, LCA (Life Cycle Assessment) Committee Report*. 1999, Japan Aluminum Association.
[21]Bahadur, R. and A. Bar-Cohen, *Orthotropic thermal conductivity effect on cylindrical pin fin heat transfer.* International Journal of Heat and Mass Transfer, 2007. **Vol. 50**: p. pp. 1155-1162.
[22]*AB SEGERFRÖJD Polymer Heat Exchangers*. [cited 2009 Jan 29]; Available from: http://www.segerfrojd.se/.
[23]Liu, W., J. Davidson, and S. Mantell, *Thermal Analysis of Polymer Heat Exchangers for Solar Water Heating: A Case Study.* Journal of Solar Energy Engineering, 2000. **122**(2): p. 84-91.
[24]*Power Cold Nauticon Wet/Dry Fluid Cooler*. [cited 2009 Jan 29]; Available from: http://www.powercold.com/site/Products/nauticoncooler.
[25]*Fluorotherm Corporation*. [cited 2009 Jan 29]; Available from: http://www.fluorotherm.com/immersion_heat_exchanger.html.
[26]Lowenstein, Thin plastic film for absorption chillers, US Patent No. 5992508, 1999
[27]Haogland, Desiccant-free heat and moisture exchange wheel, US Patent No. 6565999, 20003
[28]*Therma-Tech Thermally Conductive Compounds*. 2008 [cited 2008 August 4]; Available from: http://www.polyone.com/en-us/products/engresincompound/Pages/Therma-TechThermallyConductiveCompounds.aspx.
[29]*Cool Polymers Thermally Conductive Polymers*. [cited 2009 Jan 29]; Available from: http://www.coolpolymers.com/.
[30]Bar-Cohen, A., R. Bahadur, and M. Iyengar, *Least-energy optimization of air-cooled heat sinks for sustainability-theory, geometry and material selection.* Energy, 2006. **Vol. 31**: p. pp. 579-619.
[31]Nielsen, L.E., *The Thermal and Electrical Conductivity of Two-Phase Systems.* Ind. Eng. Chem. Fund., 1974. **13**(1): p. 17-20.
[32]X. Lu and G. Xu, *Thermally conductive polymer composites for electronic packaging.* Journal of Applied Polymer Science, 1997. **65**(13): p. 2733-2738.
[33]C. P. Wong, R.S.B., *Thermal conductivity, elastic modulus, and coefficient of thermal expansion of polymer composites filled with ceramic particles for electronic packaging.* Journal of Applied Polymer Science, 1999. **74**(14): p. 3396-3403.
[34]Bar-Cohen, A. and R. Bahadur. *Characterization and Modeling of Anisotropic Thermal Conductivity in Polymer Composites*. in *ASME International Mechanical Engineering Congress and Exposition*. 2006.

[35]Bahadur, R., *Characterization, modeling, and optimization of polymer composite pin fins*, in *Mechanical Engineering Ph.D. Thesis*. 2005, University of Maryland: College Park.
[36]Mohd Ishak, Z.A. and J.P. Berry, *Hygrothermal Aging Studies of Short Carbon Fiber Reinforced Nylon 6.6.* Journal of Applied Polymer Science, 1994. **51**: p. 2145-2155.
[37]*TIMET TIMETAL® 3-2.5 Titanium Alloy (Ti-3Al-2.5V; ASTM Grade 9) Typical Properties* [cited April 1 2009]; Available from: http://www.matweb.com/search/DataSheet.aspx?MatGUID=3695f9f62f87457db57cb148a93399de.
[38]*Aluminum 6061-T6; 6061-T651* [cited April 1 2009]; Available from: http://www.matweb.com/search/DataSheet.aspx?MatGUID=1b8c06d0ca7c456694c7777d9e10be5b.
[39]Suzuki, T. and J. Takahashi. *Prediction of energy intensity of carbon fiber reinforced plastics for mass-produced passenger cars*. in *9th Japan International SAMPE Symposium JISSE-9*. 2005. Tokyo, Japan.
[40]Harper, D. and W. Brown, *Mathematical Equations for Heat Conduction in the Fins of Air-Cooled Engines.* NACA Report, 1922.
[41]Schneider, P.J., *Conduction heat transfer*. Addison-Wesley series in mechanical engineering. 1955, Cambridge, Mass.: Addison-Wesley Pub. Co.
[42]Incropera, F. and D. DeWitt, *Introduction to Heat Transfer*. 2002, New York: John Wiley & Sons.
[43]Gardner, K., *Efficiency of extended surfaces.* Trans. ASME, 1945. **vol. 67**: p. pp. 621-631.
[44]Kern, D. and A. Kraus, *Extended Surface Heat Transfer*. 1992, New York: McGraw-Hill.
[45]Iyengar, M. and A. Bar-Cohen, *Least-material optimization of vertical pin-fin, plate-fin, and triangular-fin heat sinks in natural convective heat transfer.* Thermal and Thermomechanical Phenomena in Electronic Systems, 1998. ITHERM'98. The Sixth Intersociety Conference on, 1998: p. 295-302.
[46]Bejan, A., *Entropy generation through heat and fluid flow*. 1982, New York: Wiley.
[47]Ogiso, K., *Assessment of Overall Cooling Performance in Thermal Design of Electronics Based on Thermodynamics.* Journal of Heat Transfer, 2001. **123**(5): p. 999-1005.
[48]Iyengar, M. and A. Bar-Cohen, *Least-energy optimization of forced convection plate-fin heat sinks.* Components and Packaging Technologies, IEEE Transactions on [see also Components, Packaging and Manufacturing Technology, Part A: Packaging Technologies, IEEE Transactions on], 2003. **26**(1): p. 62-70.
[49]Culham, J.R. and Y.S. Muzychka, *Optimization of Plate Fin Heat Sinks Using Entropy Generation Minimization.* IEEE TRANSACTIONS ON COMPONENTS AND PACKAGING TECHNOLOGIES, 2001. **24**(2): p. 159.
[50]Lin, W.W. and D.J. Lee, *Second-law analysis on a flat plate-fin array under crossflow.* International Communications in Heat and Mass Transfer, 2000. **27**(2): p. 179-190.

[51]Shuja, S.Z., S.M. Zubair, and M.S. Khan, *Thermoeconomic design and analysis of constant cross-sectional area fins.* Heat and Mass Transfer, 1999. **34**(5): p. 357-364.
[52]Khan, W.A., J.R. Culham, and M.M. Yovanovich, *Optimization of pin-fin heat sinks using entropy generation minimization.* Components and Packaging Technologies, IEEE Transactions on [see also Components, Packaging and Manufacturing Technology, Part A: Packaging Technologies, IEEE Transactions on], 2005. **28**(2): p. 247-254.
[53]Luckow, P., et al., *Energy Efficient Polymers for Gas-Liquid Heat Exchangers* in *ASME 2nd International Conference on Energy Sustainability*. 2008: Jacksonville, FL, USA.
[54]Bar-Cohen, A. and M. Jelinek, *Optimum Arrays of Longitudinal, Rectangular Fins in Corrective Heat Transfer.* Heat Transfer Engineering, 1985. **Vol. 6**: p. pp. 68 - 78.
[55]Shah, R.K. and M.S. Bhatti, *Laminar convective heat transfer in ducts.* Handbook of Single-phase Convective Heat Transfer, 1987: p. 3.1-3.137.
[56]Gnielinski, V., *New equations for heat and mass transfer in turbulent pipe and channel flow.* Int. Chem. Eng, 1976. **Vol. 16**(Issue 2): p. 359–368.
[57]Kays, W.M., *Numerical Solutions for Laminar-Flow Heat Transfer in Circular Tubes.* Trans. ASME, 1955. **Vol. 77**: p. pp. 1265-1274.
[58]Pethukhov, B.S., in *Advances in Heat Transfer*, T.F. Irvine and J.P. Hartnett, Editors. 1970, Academic Press: New York.
[59]Bar-Cohen, A. and M. Iyengar, *Design and optimization of air-cooled heat sinks for sustainable development.* Components and Packaging Technologies, IEEE Transactions on [see also Components, Packaging and Manufacturing Technology, Part A: Packaging Technologies, IEEE Transactions on], 2002. **Vol. 25**: p. pp. 584-591.
[60]*Personal communication wit Mr. Nashaat M. Mohamed, senior process engineer, July*. 2007, ADGAS.
[61]*Recyclability and Energy Efficiency: The Case for Copper in Car and Truck Radiators*. 2008 [cited 2008 Aug 07]; Available from: http://www.copper.org/applications/automotive/radiators/recyclability.html.
[62]*SPINE LCI dataset: CuNi10Fe extrusion and drawing of tubes*. CPM LCA DATABASE 2008 [cited 2008 November 10]; Available from: http://www.cpm.chalmers.se/CPMDatabase/Scripts/sheet.asp?ActId=Designer1997-12-08862#About%20Inventory.
[63]Zweben, C. *Emerging High-Volume Applicaitons for Advanced Thermally Conductive Materials*. in *Proceedings, SAMPE 2004*. 2004. Long Beach, California.
[64]*Personal commincation with Mr. Juan Cevallos, EERC Polymer Heat Exchanger Project.* 2009.
[65]*Personal communication with Dr. SK Gupta, Professor of Mechanical Engineering, University of Maryland*. 2009.
[66]Abdelaziz, O., A. Vikrant, and R. Radermacher, *Multi-Scale Simulation for Novel Heat Exchanger Designs.* ASME Journal of Heat Transfer. **HT-08-1509 [in review]**.

[67]Abdelaziz, O., et al., *A-Type Heat Exchanger Simulation using 2-D CFD for Airside Heat Transfer and Pressure Drop*, in *12th International Refrigeration and Air Conditioning Conference at Purdue*. 2008: Purdue University, West Lafayette, IN 2008. p. 1-8.

[68]*ADGAS Personnel & Training Division, "Basic Operator Course: Heat Exchangers," Module 4, Rev.03.*

[69]Iyengar, M. and A. Bar-Cohen, *Design for manufacturability of SISE parallel plate forcedconvection heat sinks.* Components and Packaging Technologies, IEEE Transactions on [see also Components, Packaging and Manufacturing Technology, Part A: Packaging Technologies, IEEE Transactions on], 2001. **Vol. 24**(2): p. pp. 150-158.

[70]*eFunda Polymer Properties: ABS*. [cited 2009 April 25]; Available from: http://www.efunda.com/materials/polymers/properties/polymer_datasheet.cfm?MajorID=ABS&MinorID=7.

[71]*Babyplast Injection Molding Machine*. [cited 2009 May 1]; Available from: http://www.babyplast.com/httpweb/catalogo/index.php?view=prodotti&cod_categoria=AA.

[72]Mcmaster-Carr. *About Selecting Thermal Insulation*. [cited 2008 July 1]; Available from: http://www.mcmaster.com/#catalog/114/3412.

[73]Mcmaster-Carr. *Rigid Fiberglass Insulation for Pipe and Tube*. [cited 2008 July 1]; Available from: http://www.mcmaster.com/#catalog/114/3419.

[74]*Saxon PC 120mm Airflow straightener*. [cited 2009 April 25]; Available from: http://www.saxonpc.com/120mm-airflow-honeycomb-without-hous120.html.

[75]Groth, J. and A.V. Johansson, *Turbulence reduction by screens.* Journal of Fluid Mechanics, 1988. **197**: p. 139-155.

[76]Munson, B.R., D.F. Young, and T.H. Okiishi, *Fundamentals of fluid mechanics*. 2006, Hoboken, NJ: J. Wiley & Sons.

[77]Shah, R.K. and A.L. London, *Laminar Flow Forced Convection in Ducts: A Source Book for Compact Heat Exchanger Analytical Data*. 1978: Academic Pr.

[78]*40x40x28 Series Fans*. Everflow Technology Corp. 2006 [cited 2008 July 1]; Available from: http://www.everflowtech.com/catalog/show_pg.asp?pg=10.

[79]ASHRAE, *Standard 111: Practices for Measurement, Testing, Adjusting, and Balacing of Building Heating, Ventilation, Air Conditioning, and Refrigeration Systems*. 1988.

[80]*Velocity Traverse of Air Ducts*. Air Monitor Corporation Standards [cited 2008 July 1]; Available from: http://www.airmonitor.com/documents/shared/brochures/BRO_Standards_12501300.pdf.

[81]*Flow & Level Measurement*. Omega Transactions [cited 2008 June 17th]; Available from: http://www.omega.com/literature/transactions/volume4/T9904-09-ELEC.html.

[82]*Farnam Custom Products Axial Fan Heater*. [cited 2009 April 24]; Available from: http://www.farnam-custom.com/air_heaters/axialfanheater.php.

[83]*Thermocouple Wire Color Codes and Limits of Error*. Omega Engineering, Inc. [cited 2009 March 30]; Available from: http://www.omega.com/techref/colorcodes.html.
[84]*Arctic Silver Thermal Adhesive*. [cited 2009 March 29]; Available from: http://www.arcticsilver.com/arctic_silver_thermal_adhesive.htm.
[85]Carvile, J., *Mechanical Engineer's Data Handbook*. 1994: Butterworth-Heinemann.
[86]*USB-TC Thermocouple Input Module*. [cited 2009 May 1]; Available from: http://www.measurementcomputing.com/usb-data-acquisition/USB-TC.aspx.
[87]Figliola, R.S. and D.E. Beasley, *Theory and design for mechanical measurements*. 2006, Hoboken, N.J.: John Wiley.
[88]Moffat, R.J. *Uncertainty analysis*. Electronics Cooling 1998 [cited 2008 June 22]; Available from: http://www.electronics-cooling.com/articles/1999/1999_may_article3.php.
[89]Taylor, J.R., *An introduction to error analysis : the study of uncertainties in physical measurements*. 1997, [S.l.]: University Science.
[90]*ITS-90 Table for Thermocouples Coefficients of Approximate Inverse Functions*. 1995 [cited 2008 August 1]; Available from: http://srdata.nist.gov/its90/type_j/jcoefficients_inverse.html.
[91]Culham, J.R., M.M. Yovanovich, and S. Lee, *Thermal modeling of isothermal cuboids and rectangular heat sinks cooled by natural convection.* Components, Packaging, and Manufacturing Technology, Part A, IEEE Transactions on, 1995. **Vol. 18**(Issue 3): p. 559-566.
[92]*Loctite® Epoxy Gel* [cited 2009 March 30]; Available from: http://www.loctiteproducts.com/products/detail.asp?catid=11&subid=49&plid=440.
[93]Sieder, E.N. and G.E. Tate, *Heat Transfer and Pressure Drop of Liquids in Tubes.* Ind. Eng. Chem., 1936. **28**(12): p. 1429-1435.
[94]*PolyOne*. Therma-Tech NJ-600 TC [Technical Data Sheet] [cited 2008 July 22]; Available from: http://catalog.ides.com/pdfdatasheet.aspx?I=55275&E=85972.
[95]Lapin, L.L., *Probability and statistics for modern engineering*. 1983, Monterey, Calif.: Brooks/Cole Engineering Division.